DESIGN AND DEVELOPMENT OF POLYMERIC NANOPARTICLES FOR THE DELIVERY OF THERAPEUTICS

A Dissertation

by

FUWU ZHANG

Submitted to the Office of Graduate and Professional Studies of
Texas A&M University
in partial fulfillment of the requirements for the degree of

DOCTOR OF PHILOSOPHY

Chair of Committee,	Karen L. Wooley
Committee Members,	Marcetta Y. Darensbourg
	Michael V. Pishko
	Daniel Romo
Head of Department,	François P. Gabbaï

August 2015

Major Subject: Chemistry

ABSTRACT

The development of nanoscale drug delivery systems is a rapidly growing field within the realm of nanomedicine, as it has the potential to improve therapeutic efficacy and minimize side effects of various drugs. This dissertation focuses on the rational design, development and application of well-defined polymeric nanoparticles, capable of high loading of both hydrophobic and hydrophilic therapeutic agents, toward the effective treatment of lung diseases.

In the first study, cisplatin was loaded into non-degradable poly(acrylic acid)-*b*-polystyrene-based SCKs through the formation of coordination bonds between platinum and carboxylate groups in the nanoparticle shell domain. The effects of crosslinking were investigated by comparing drug loading & release, *in vitro* cytotoxicities, and immunotoxicities. In another study, degradable polyphosphoester-based polymeric micelles and SCKs, each derived from non-cytotoxic, amphiphilic block-graft terpolymers, were specifically designed and synthesized for anti-cancer drug paclitaxel (PTX) delivery toward the treatment of osteosarcoma lung metastases. PTX could be encapsulated into either micelles or SCKs, with overall PTX concentration as high as 4.8 mg/mL *vs.* the low solubility for free PTX in water of less than 2.0 μg/mL. *In vivo* biodistribution indicated that both micelles & SCKs underwent extravasation from the lung in a controlled manner, while crosslinking slowed the rate of extravasation significantly. Moreover, hydrophilic silver cations were also attached to the nanoparticles *via* the interaction between silver and alkyne as a potential treatment for

bacterial pulmonary infections. The well-defined Ag-loaded nanoparticles released silver in a controlled and sustained manner over 5 days, and displayed enhanced *in vitro* antibacterial activities against cystic fibrosis-associated pathogens and decreased cytotoxicity to human bronchial epithelial cells, in comparison to silver acetate.

DEDICATION

To my wife and my children

ACKNOWLEDGEMENTS

I would first thank my Ph.D. advisor Prof. Karen L. Wooley, for her invaluable guidance, support, patience, and trust in my graduate study at Texas A&M University. For the past five years, I have learnt from her not only tremendous knowledge of science and technology, but also her passion, diligence, dedication for science and research. She gave me the freedom to explore the fields of polymer science and nanotechnology, and provided me with helpful advice to improve my research. I was extremely fortunate to be one of her students, and was able to grow into an independent researcher with critical thinking and special attention to details. Without her, I could not achieve so much, and she will always be my great mentor and friend.

I would also like to thank my committee members, Prof. Marcetta Y. Darensbourg, Prof. Michael V. Pishko, and Prof. Daniel Romo for their valuable advice and simulating discussions, which led to improved research toward the completion of this dissertation.

The major work of this dissertation was conducted in collaboration with brilliant scientists from both academia and industry. I have enjoyed working with Dr. Carolyn L. Cannon from Texas A&M University and her lab members Mr. Justin A. Smolen and Dr. Parth N. Shah. The invaluable discussion and great collaboration have yield one important chapter in this dissertation. I would also thank Dr. Dennis M. P. Hughes from The University of Texas MD Anderson Cancer Center and his lab members Dr. Laura D. Nelson and Dr. Yanwen Yang, and Dr. Mark W. Lenox and Ms. Rachel Johnson from Texas A&M Institute for Preclinical Studies for their valuable discussion and

collaborative work on the lung metastasis of osteosarcoma project. I also enjoyed working with Dr. Suzanne Lapi and her lab member Dr. Tolu Aweda from Washington University in St. Louis on biodistribution of silver-loaded nanoparticles. I also want to thank Dr. Richard B. Dorshow, Dr. Dennis A. Moore from Covidien Pharmaceuticals, Dr. Henrik Sune Andersen and his team members from Novo Nordisk for insightful discussions.

Within the Wooley group, I would first thank Dr. Shiyi Zhang and Dr. Yun Lily Lin for their great mentorship and friendship. I learned many useful techniques and had a better understanding of my research direction through numerous discussions. I also want to acknowledge Mr. Richen Li, Mr. Hai Wang, Mr. Yi-Yun Tsao, and Ms. Sarah Leininger for their great help in my research. I have learned tremendous knowledge through the collaboration with Dr. Mahmoud Elsabahy, Dr. Tiffany P. Gustafson, Dr. Jeffery E. Raymond, and Dr. Jiong Zou. Their professional opinions and practical advices are invaluable for my graduate research. I would also like to thank past and present members of the Wooley group, Dr. Yannick Borguet, Dr. Christopher Fidge, Dr. Marco Giles, Dr. Ashlee Jahnke, Dr. Soon-Mi Lim, Dr. Lu Su, Dr. Guorong Sun, Dr. Celine Besset, Dr. Philip M. Imbesi, Dr. Amandine Noel, Dr. Nam S. Lee, Dr. Ang Li, Dr. Zhou Li, Dr. Koichiro Mikami, Dr. Sandani Samarajeewa, Dr. Ritu Shrestha, Dr. Kevin A. Pollack, Dr. Scott Zawko, Mr. Sangho Cho, Mr. Daniel Dobbins, Mr. Jingwei Fan, Ms. Simcha Felder, Ms. Jeniree Flores, Ms. Amelia Gonzalez, Mr. Xun He, Mr. Gyu Seong Heo, Ms. Sarosh Khan, Mr. Chris Komatsu, Ms. Samantha Kristufek, Mr. Eric Leonhardt, Mr. Young Lim, Ms. Lauren Link, Mr. Alexander Lonnecker, Ms.

Casey McDonald, Mr. Andy Moutray, Ms. Stephanie Pollack, Ms. Danielle Policarpio, Mr. Kenton Rauwerdink, Mr. Joel Russell, Ms. Jennifer Streff, Ms. Adriana Pavia-Sanders, Ms. Kellie Seetho, Ms. Jennifer Summerhill, Mr. Matthew Svach, Ms. Judy Taylor, Mr. Eric Vavra, Ms. Ginny Vance, Mr. Kevin Wacker, Ms. Sarah Ward, and Mr. Ryan Zentay, who created a friendly and safe work environment and supported my research.

Lastly, I would like to thank my wife, my parents, and my parents-in-law for their continued support for my graduate research. I especially thank my wife, Shan Li, for her endless love, patience, trust and support. She has taken good care of my two babies, Ella L Zhang and Eric L Zhang, and let me concentrate on my research. She is always standing by my side whatever happens, and finally we are going to finish this incredible journey together.

For Chapter II, the Welch Foundation is gratefully acknowledged for support through the W. T. Doherty-Welch Chair in Chemistry, Grant No. A-0001. The China Scholarship Council is also gratefully acknowledged for fellowship support.

For Chapter III, I would like to thank Dr. Yanwen Yang at The University of Texas MD Anderson Cancer Center, Houston, TX for his insightful discussion as regards the CCH-OS-O and SJSA osteosarcoma cell lines. The Welch Foundation is gratefully acknowledged for support through the W. T. Doherty-Welch Chair in Chemistry, Grant No. A-0001. D.P.M. Hughes is supported by the NCI of the NIH under award numbers R01CA149501 and R01CA141208. This material is also based upon work supported by the National Science Foundation under the Research Experiences for Undergraduates

(NSF-REU) program, grant number CHE-1062840. The Microscopy & Imaging Center at Texas A&M University is gratefully acknowledged and we thank Dr. Hansoo Kim and Dr. Stanislav Vitha for cryo-TEM studies. We thank the VIBS Histology lab at the Texas A&M College of Veterinary Medicine, specifically Mrs. Lin Bustamante and Mrs. Chaitali Mukherjee for their suggestions as regards preparation of tissue samples and sections, and the Texas A&M Institute for Genomic Medicine for their expertise and advice in the establishment and breeding of our NSG mouse colony.

For Chapter IV, I would like to gratefully acknowledge financial support from the National Heart Lung and Blood Institute of the National Institutes of Health as a Program of Excellence in Nanotechnology (HHSN268201000046C) and the National Science Foundation (DMR-1309724 and DMR-1105304). The Welch Foundation is acknowledged for support through the W. T. Doherty-Welch Chair in Chemistry, Grant No. A-0001. The Microscopy & Imaging Center at Texas A&M University is gratefully acknowledged and we thank Dr. Hansoo Kim for help with the EDS elemental mapping. The authors thank Adriana Pavía-Sanders for her kind assistance with the 3D illustrations of micelles.

NOMENCLATURE

AFM	Atomic force microscopy
AIBN	2,2'-Azobis(isobutyronitrile)
ATR-IR	Attenuated total reflectance infrared spectroscopy
ATRP	Atom transfer radical polymerization
$CDCl_3$	Deuterated chloroform
CDDP	Cisplatin
CMC	Critical micelle concentration
CTA	Chain transfer agent
CuAAC	Copper(I)-catalyzed azide-alkyne cycloaddition
DBU	1,8-Diazabicyclo[5.4.0]-undec-7-ene
DCM	Dichloromethane
DDMAT	S-1-dodecyl-S'-(α, α'-dimethyl-α"-acetic acid)trithiocarbonate
DIPEA	*N*,*N*-diisopropylethylamine
DLS	Dynamic light scattering
DMF	*N*,*N*-dimethylformamide
DMSO	Dimethyl sulfoxide
DNA	Deoxyribonucleic acid
D_2O	Deuterium oxide
DOX	Doxorubicin

DSC	Differential scanning calorimetry
EDCI	1-[3’-(Dimethylamino)propyl]-3-ethylcarbodiimide methiodide
EDDA	2,2’-(Ethylenedioxy) bis(ethylamine)
EPR	Enhanced permeation and retention
FT-IR	Fourier transform infrared spectroscopy
GPC	Gel permeation chromatography
HPLC	High performance liquid chromatography
ICP-MS	Inductively coupled plasma mass spectrometry
MBC	Minimum bactericidal concentration
MHB	Mueller Hinton broth
MIC	Minimum inhibitory concentration
M_n	Number-average molecular weight
MPS	Mononuclear phagocyte system
MWCO	Molecular weight cutoff
NIR	Near-infrared
NMR	Nuclear magnetic resonance spectroscopy
PAA	Poly(acrylic acid)
PBS	Phosphate buffered saline
PDI	Polydispersity index
PEG	Poly(ethylene glycol)
PK	Pharmacokinetics
PMDETA	*N*,*N*,*N′*,*N′*,*N″*-pentamethyldiethylenetriamine

PS	Poly(styrene)
PTA	Phosphotungstic acid
P*t*BA	Poly(*tert*-butyl acrylate)
PTX	Paclitaxel
RAFT	Reversible addition-fragmentation chain transfer
ROP	Ring-opening polymerization
SCK	Shell crosslinked knedel-like nanoparticle
TBD	1,5,7-Triazabicyclo[4.4.0]dec-5-ene
TEA	Triethylamine
TEM	Transmission electron microscopy
TFA	Trifluoroacetic acid
T_g	Glass transition temperature
TGA	Thermogravimetric analysis
THF	Tetrahydrofuran
UV	Ultraviolet

TABLE OF CONTENTS

LIST OF FIGURES

Page

LIST OF TABLES

Page

CHAPTER I

INTRODUCTION

1.1 Nanomedicine

In 1959, American physicist Richard Feynman first introduced the concept of nanotechnology in his prescient talk "There's Plenty of Room at the Bottom", where he talked about the manipulating and controlling things on the atomic and molecular level.[1] Nowadays, nanotechnology is a rapidly growing filed, with numerous applications in fields such as medicine, electronics, and materials. The application of nanotechnology in medicine has led to a new field termed nanomedicine, where nanostructured materials are used to prevent, diagnose, and treat diseases.[2,3] Within the realm of nanomedicine, the development of nanoscale drug delivery systems is a rapidly growing field, accounting for 76% scientific papers and 59% of the patents during 1984-2004.[3] There are several advantages of using nanoscopic carriers for therapeutic agents.

First, nanocarriers can improve drugs' solubility and chemical stability. For example, the aqueous concentration of paclitaxel (PTX) was increased from < 2 μg/mL to 4 mg/mL in the micellar formulation Genexol-PM® (approved for breast cancer in South Korea in 2007), which was self-assembled from amphiphilic block copolymer poly(ethylene glycol)-*b*-poly(D,L-lactide).[4] Additionally, it was found that PTX would undergo epimerization and hydrolysis into several species in aqueous solution.[5] The chemical stability of PTX may be increased by encapsulation in the core of the micelles

via hydrophobic interaction, which limits its exposure to water. These nanocarriers can also protect the drug from biodegradation by enzymes or inactivation by biological compounds such as protein.[6]

Second, nanocarriers can release their payload in a controlled manner.[7] Since the toxicities of drugs are usually dependent on their maximum plasma concentrations, slow and sustained drug release can partially alleviate their side effects.[8,9] For example, cisplatin-incorporating polymeric micelles (NC-6004) formulation, which slowly released 50% cisplatin over 4 days, was shown to reduce the ototoxicity, nephrotoxicity and neurotoxicity of cisplatin *in vivo*.[10,11] Further, carefully designed stimuli-sensitive nanocarriers could release drugs under environmental triggers, such as pH, temperature, enzyme, and light, which can limit premature drug release and thus minimize systemic exposure and reduce side effects.[12,13]

Third, nanomedicine can improve the biodistribution and pharmacokinetics of drugs. Biodistribution and pharmacokinetics of free drugs, which are determined by their intrinsic physic-chemical properties, are usually not optimal and have issues such as rapid renal clearance, binding to plasma proteins and limited ability to penetrate into tumor tissues.[12] On the other hand, nanosized drug delivery vehicles, especially those that were coated with poly(ethylene glycol) or poly(zwitterions)s, for instance, poly(carboxybetaine)s (PCBs), were reported to have decreased the nonspecific protein interactions and slower clearance from the bloodstream, which led to longer blood circulation time.[14-18] Furthermore, drugs incorporated in nanocarriers can preferably accumulate in cancer tissues by passive targeting exploiting a mechanism known as the

enhanced permeability and retention (EPR) effect, and active targeting *via* attaching targeting ligands to the surface of nanocarriers.[19]

The EPR effect was first described by Matsumura and Maeda in 1986 and was one of the greatest breakthroughs in targeted therapeutics delivery.[20,21] Briefly, cancer tissues have higher vascular permeability but comprised lymphatic drainage system compared to normal tissues, which allows macromolecules and nanoparticles to enter the tumor's interstitial spaces and remain there.[20,22] On the other hand, molecules with low molecular weight will return to circulation by diffusion.[20,22] Therefore, drugs loaded in nanocarriers are expected to selectively accumulate in cancer tissues, resulting in improved therapeutic efficacy and minimize side effects.

In addition to passive targeting by the EPR effect, nanocarriers can also actively target the cancer tissues by attaching targeting ligands, such as antibodies, aptamers, peptides and some other small molecules, to the surface of nanocarriers.[19] The targeting ligands can be selectively recognized by the receptors that are overexpressed on the surface of cancer cells, and thus facilitate the selective accumulation of nanocarriers in cancer tissues and subsequent internalization by cancer cells.[23] For example, the overexpression of folate receptors is observed in varieties of human cancers.[23] The folate conjugated liposomes, with doxorubicin loaded, were shown to have 45-fold higher cellular uptake of doxorubicin over non-targeted doxorubicin-loaded liposomes in KB cells.[24] This targeted formulation was also found to be 86-fold higher cytotoxic compared to non-targeted formulations.[24] The ligand-receptor interaction is much more selective and precise than passive targeting; hence, receptor-mediated nanomedicine is

expected to greatly enhance drug efficacy and reduce side effects. However, most of actively targeted formulations have failed to demonstrate benefits in clinical testing, likely due to their intrinsic complexity and a number of anatomical and physiological barriers existing on their way from circulation to cancer cells.[12,19,25]

1.2 Polymeric micelles

Various types of nanoscopic carriers have been developed over the past decades, such as antibody drug conjugates (ADCs), polymer drug conjugates, liposomes, polymeric micelles, dendrimers, and inorganic nanoparticles.[12] There are about 15 nanostructured formulations on the market today (two of the approved antibody drug conjugates have been withdrawn from market in 2010 and 2014).[12] Among them, liposome-based formulations are one of the most successful nanocarriers, with 7 formulations currently on the market and more than 50 formulations in clinic trials.[12] The inner aqueous environment of the liposome makes it especially suitable for water-soluble drugs with high loading capacity, such as doxorubicin hydrochloride (the active ingredient of Doxil®) and vincristine sulfate (the active ingredient of Marqibo®).[12,26-28] Hydrophobic drugs could also be loaded into the lipid bilayer, but with generally low drug loading due to the limited space within the bilayer, for example, the liposome-entrapped paclitaxel easy-to-use (LEP-ETU) formulation had a drug content of 3.3% (w/w).[29]

Recently, polymeric micelles, constructed *via* the self-assembly of amphiphilic block copolymers, have attracted extensive investigation due to their characteristic core-shell morphology, where hydrophobic cores are especially suitable for the incorporation of hydrophobic drugs, such as paclitaxel (PTX), camptothecin (CPT), and their derivatives,

while the hydrophilic shells provide water solubility and functionality for post-modification such as crosslinking, dye labeling, PEGylation, and installation of targeting ligands.[16,30-33] For example, the micellar formulation Genexol-PM®, self-assembled from amphiphilic block copolymer poly(ethylene glycol)-*b*-poly(D,L-lactide), were shown to have a drug loading around 20%.[4,34] Hydrophilic drugs can also be loaded into the shell of micelle by various mechanisms, for example, electrostatic interactions or formation of silver acetylides for silver cations loading, and formation of coordination bonds for cisplatin loading.[35-37] Furthermore, different sizes and morphologies, like spheres, cylinders, toroids, vesicles and helices, can be obtained by tuning the chemical structures of polymer, and the length & ratio of hydrophilic and hydrophobic building blocks.[16,38-40] However, micelles cannot maintain their sizes and morphologies below the critical micelle concentration (CMC), and will dissociate into single polymer chains. Since micelles are dynamic systems, structure reorganization of micellar structure may lead to dissociation of their payload even at concentrations above the CMC.

To overcome micellar dissociation, shell crosslinking is of significant importance to enhance structural stability, as well as to mediate stimuli-responsive drug release.[16,41] Shell crosslinked knedel-like nanoparticles (SCKs), were first introduced by Wooley and coworkers in 1990s.[42] Over the past two decades, the incorporation of crosslinks within the shells of polymeric micelles has been shown to improve their structural stability, while retaining the tunability of size and shape, and enhancing the ability to perform chemical modifications throughout the shell of the nano-sized scaffold or within other selective domains.[42-49] Besides improved stability in aqueous environments, shell

crosslinks serve as an additional physicochemical barrier to protect drugs in the hydrophobic core from hydrolysis or enzymatic degradation, as well as to mediate drug release.[41] Moreover, by incorporating stimuli-responsive crosslinkers, SCKs can have accelerated drug release under external triggers, for instance, SCKs with a redox-responsive disulfide crosslinker were shown to release PTX significantly faster in the presence of glutathione (GSH) compared to those without GSH.[50] In addition, hollow nanocages can be obtained by removal of the core of SCKs, which may have higher loading capacity over their parent micelles.[51]

Both degradable and non-degradable amphiphilic block copolymers have been used as the building units for drug delivery carriers. Though non-degradable polymers, such as polyacrylic acids and polystyrene-based block copolymers, are investigated as potential drug delivery carriers due to facile synthesis, easy manipulation, and no complication with degradation products, biocompatible and biodegradable polymers have drawn more attention as they can be ultimately cleared from biological systems *via* intrinsically built-in degradation pathways.[16,36,52,53] Nowadays, a variety of biodegradable polymers, such as polyesters,[15,54,55] polypeptides,[56,57] polycarbonates,[58-60] polyphosphoesters,[61-63], polyketals,[64] and others,[65] could be obtained with relatively narrow polydispersity indices, due to significant progress made in polymerization techniques, especially living controlled polymerization.[52] Among them, polyphosphoesters have been widely used in biomedical applications, such as drug delivery,[66,67] gene delivery[68,69] and tissue engineering,[70,71] because of their biocompatibility, biodegradability and structural similarity to naturally occurring biomacromolecules, such as DNA and RNA.[52,69,72-74]

Since the phosphorous atom is pentavalent, reactive pendant groups, including hydroxyl, carboxyl, and alkynyl goups, may be introduced as side-chain functionalities, allowing polyphosphoesters to be structurally versatile.[52,61,62]

1.3 Lung cancer and pulmonary infections

Despite current significant advancements in modern medicine, lung cancer and pulmonary infections continue to pose great clinical challenges to successful medical treatment. According to World Health Organization, cancer in total caused 8.2 million of deaths in the world in 2012, among which the lung cancer caused the most deaths comprising 1.6 million.[75] On the other hand, lower respiratory infections were reported to kill more people worldwide compared to lung cancer, accounting for 3.1 million deaths in 2012. In fact, both lung cancer and lower respiratory infections are among the top five leading causes of deaths worldwide in 2012.[76] There is a pressing need to develop novel effective treatments for lung diseases.

One of our target lung diseases is osteosarcoma lung metastases. Osteosarcoma is the most common primary cancer of bone in children and adolescents, with a peak incidence at the ages of 10-14 years, and a high fatality rate (70% survival at 5 years for non-metastatic patients, and < 30% for those presenting with metastasis).[77,78] Osteosarcoma can occur in any bone, with femur as the most common site.[4] The majority of osteosarcoma patients (80-90%) have microscopic metastasis at the time of diagnosis, though only < 20% patients with high-grade osteosarcoma have detectable metastasis.[79,80] The most common site of metastasis is the lung, followed by other bones, with approximately 40% of patients presenting with overt metastasis.[79,80]

Osteosarcoma is often treated by complete surgical excision of the primary tumor, followed by chemotherapy, preferably with more than one therapeutics to prevent or eliminate micrometastatic disease.[81,82] However, once micrometastases grow into recurrent, overt disease, tumors are often resistant to conventional chemotherapy, and unresectable recurrent disease is uniformly fatal.[81,83] More effective treatment of osteosarcoma lung metastases is needed to improve cure rates and improve patient quality of life.

Another target disease is pulmonary infections, especially those associated with cystic fibrosis (CF). CF is an inherited disease of the secretory glands, affecting ~70k people worldwide, especially those of European descent.[84] CF results from defects in a gene encoding the cystic fibrosis transmembrane conductance regulator (CFTR).[84,85] Many organs are affected, including sinuses, lungs, skin, liver, pancreas, intestines, and reproductive organs.[84] The abnormally thick and sticky mucus in the airways of lungs can cause obstructions that lead to severe problems with breathing, and provide an environment for bacterial infections to occur. Indeed, the primary cause of death of patients with CF is respiratory failure from pulmonary infections caused by bacteria, especially *Pseudomonas aeruginosa* (PA).[84] Pulmonary infections are becoming challenging for successful treatment, partly due to widespread antibiotic resistance, which enables antibiotic-resistant bacteria, such as *Enterococcus faecium, Staphylococcus aureus, Klebsiella pneumoniae, Acinetobacter baumanii, Pseudomonas aeruginosa,* and *Enterobacter species* (ESKAPE), to survive despite treatment with existing antibacterial drugs.[86-88] The growing number of multi-drug resistant strains has

made imperative the development of new antibiotics and novel approaches to deliver existing agents.[86,89-91]

The lungs have a large surface area for absorption of solutes with high permeability and low proteolytic activity, which makes them particularly suitable for direct drug delivery to the respiratory tract for lung diseases and systemic diseases as well.[92] Several small molecular drugs, for instance, tobramysin, amikacin and colistin, have been delivered to the lungs to treat respiratory diseases, such as asthma or cystic fibrosis.[92,93] More recently, nanoparticle-based formulations have been explored extensively for the added benefit of controlled drug release.[92] These formulations are most often delivered to the lungs through nebulization into micro-scale droplets with 1-5 μm aerodynamic diameter.[92,94] Larger sized particles mainly deposit in upper airways, while very small particles are more likely to remain suspended or be exhaled.[92] The non-invasive aerosol delivery of drug-loaded nanoparticles has been reported to yield high pulmonary drug concentration, reduced systemic toxicity, and reduced dosage requirements, compared with parenteral and oral administration.[35,95-97] Therefore, we intend to exploit the local delivery of high quantities of the therapeutic agents, PTX for osteosarcoma lung metastases and silver cations for pulmonary infections, with degradable polymer-based nanoparticles being able to overcome key challenges of packaging and transport of sufficient drug quantities directly to the site of the diseases, as well as extravasation of the delivery vehicle from the lungs and secondary organs.

1.4 Scope of the thesis

This dissertation is focused on the design and development of polymeric nanoparticles for the delivery of therapeutics. Well-defined nanoparticles were prepared by self-assembly of amphiphilic block copolymer, especially polyphosphoester-based degradable polymers, for targeted delivery of therapeutic agents, including, cisplatin and PTX for cancer therapy, and silver-based small molecules & other antibiotics for pulmonary infections. These drugs are either physically entrapped or chemically conjugated to the nanocarriers.

In Chapter II, we have investigated the effects of crosslinking on the incorporation of cisplatin into SCKs by forming polymer-metal complexes, where cisplatin was loaded into shells of these nanoparticles. Nanosized particles with unimodal size distribution and low polydispersity were formed. The nanoparticles imparted significant physical stability to the incorporated drug and allowed control over its release from the polymeric particles. Crosslinking of polymeric micelles is often considered to be beneficial for improved stability against dilution. Here, with Pt-complexation, Pt provides complexation-based crosslinks and additional covalent crosslinks diminish sites for Pt complexation, giving lower drug loading and higher *in vitro* immunotoxicity. Therefore, any covalent crosslinking within future nanoparticle designs should be incorporated into an alternate region within the nanoparticle framework, to avoid consuming functionalities required for the drug-complexation. More recently, nanoscopic delivery vehicles comprised of degradable polymers have been developed, where cisplatin was

loaded into either core or shell of these nanoparticles without additional covalent crosslinking (Appendix A).

Nanomaterials have great potential to offer effective treatment against devastating diseases by providing sustained release of high concentrations of therapeutic agents locally, especially when the route of administration allows for direct access to the diseased tissues. In Chapter III, biodegradable polyphosphoester-based polymeric micelles and SCKs have been designed from amphiphilic block-graft terpolymers, poly(2-ethylbutoxy phospholane)-*block*-poly(2-butynyl phospholane)-*graft*-poly(ethylene glycol) (PEBP-*b*-PBYP-*g*-PEG), which effectively incorporate high concentrations of PTX. Well-dispersed nanoparticles physically loaded with PTX were prepared, exhibiting desirable physiochemical characteristics. Encapsulation of 10 *wt*% PTX, into either micelles or SCKs, allowed for aqueous suspension of PTX at concentrations up to 4.8 mg/mL, as compared to < 2.0 μg/mL for the aqueous solubility of the drug alone. Drug release studies indicated that PTX released from these nanostructures was defined through a structure-function relationship, whereby the half-life of sustained PTX release was doubled through crosslinking of the micellar structure to form SCKs. *In vitro,* physically-loaded micellar and SCK nanotherapeutics demonstrated IC_{50} values against osteosarcoma cell lines, known to metastasize to the lungs (CCH-OS-O and SJSA), similar to the pharmaceutical Taxol® formulation. Evaluation of these materials *in vivo* has provided an understanding of the effects of nanoparticle structure-function relationships on intratracheal delivery and related biodistribution and pharmacokinetics. In this study, we have demonstrated the potential

of these novel nanotherapeutics towards future sustained release treatments *via* administration directly to the sites of lung metastases of osteosarcoma. More recently, PTX was also chemically conjugated to the polymer side chains. The drug conjugates maintained the ability to physically encapsulate PTX to achieve a >15 mg/mL PTX total concentration in water (Appendix B).

In Chapter IV, polymeric micelles constructed from PEBP-*b*-PBYP-*g*-PEG were utilized as the drug carrier for silver cations *via* formation of silver acetylides with different coordination geometries, towards the treatment of pulmonary infections associated with cystic fibrosis. The amount of silver loaded into the micelles was quantified by inductively coupled plasma-mass spectrometry (ICP-MS) using rhodium as an internal standard. Up to 15% (w/w) loading could be achieved, consuming most of the pendant alkyne groups along the backbone. Raman spectroscopy of Ag-loaded micelles revealed that silver was loaded into the nanoparticles mainly by two coordination geometries at a molar feed ratio of 1:1 (alkyne : silver acetate). A combination of DLS, TEM and AFM indicated that the nanoscopic polymer assemblies were well-defined, having a hydrodynamic diameter of *ca.* 11 nm, and that they underwent significant flattening upon adsorption onto substrates. The co-localization of silver, oxygen and phosphorous, visualized by EDS elemental mapping, further confirmed that silver was loaded into the polymeric matrices. Silver was found to release in a sustained and controlled manner over 5 days, with release half-life values of 28 h in nanopure water and 16 h in 10 mM phosphate buffer containing 10 mM NaCl. The superior stability of silver cations when loaded into the micelles has the potential to

avoid the inactivation by anions and other biological compounds in the human body. Furthermore, these silver-loaded nanoparticles were measured to have higher antimicrobial activities against a series of cystic fibrosis pathogens and lower toxicities to human bronchial epithelial cells *in vitro*, as compared to the free drug (silver acetate), demonstrating advantageous features of this nanoscopic silver delivery platform. Evaluation of these silver-loaded nanoparticles as antimicrobial agents for pulmonary infections *in vivo*, as well as determination of their *in vitro* and *in vivo* degradation profiles, are currently under investigation. Combination delivery of silver and other antibiotics is also currently under investigation (Appendix C).

In addition, non-degradable poly(acrylic acid)[35,40], polyphosphoesters,[61,66,98-101] polypeptides[57,102-104] and polylactides[15,105] based nanomaterials were also extensively investigated, and related co-authored publication were listed in Appendix D.

CHAPTER II

SHELL CROSSLINKED KNEDEL-LIKE NANOPARTICLES FOR DELIVERY OF CISPLATIN: EFFECTS OF CROSSLINKING*

2.1 Introduction

Cisplatin (*cis*-dichlorodiammineplatinum(II); CDDP) is one of the most potent anti-cancer drugs, and has been widely used for many malignancies, such as testicular, ovarian, bladder, and lung cancers.[106] However, its clinical use is limited due to its severe side effects, including nausea, vomiting, auditory toxicity, neurotoxicity and nephrotoxicity.[107] In recent years, numerous nanometer-sized drug delivery systems, including polymeric micelles, dendrimers, nanogels, liposomes and star polymers, have been exploited to minimize the side effects of CDDP and improve its antitumor efficacy.[108-113] In particular, CDDP-loaded polymeric micelles *via* the formation of polymer-metal complexes have been showing promising results.[114-118] For example, NC-6004 micellar formation, where CDDP was conjugated onto poly(ethylene glycol)-*b*-poly(glutamic acid) diblock copolymers *via* coordination bonds, reached a remarkable 39% (w/w) loading, and demonstrated significantly lower toxicity and superior anti-tumor activity than CDDP.[11,109]

* Reprinted (adapted) with permission from "Shell crosslinked knedel-like nanoparticles for delivery of cisplatin: Effects of crosslinking" by Zhang, F.; Elsabahy, M.; Zhang, S.; Lin, L. Y.; Zou, J.; Wooley, K. L., *Nanoscale*, 2013, *5,* 3220-3225. http://pubs.rsc.org/en/content/articlehtml/2013/nr/c3nr34320k.

Polymeric micelles, constructed *via* the self assembly of amphiphilic block copolymers, have long been investigated for drug delivery applications due to their distinctive core-shell morphology, where the hydrophobic cores serve as reservoirs for drugs while the hydrophilic shells provide water solubility.[31,119] Over the past sixteen years, the incorporation of crosslinks within the shells of polymeric micelles, to afford shell crosslinked knedel-like nanoparticles (SCKs), has been shown to provide enhanced structural stability, while retaining tunability of size and shape, and enhancing the ability to perform chemical modifications throughout the shell of the nano-sized scaffold or within other selective domains.[42-49] Recently, we have demonstrated that SCKs could load relatively large payloads of doxorubicin (DOX) and paclitaxel (PTX) chemotherapeutic agents, mainly into their hydrophobic cores.[45,120] Herein, we explore the potential of SCKs as the delivery carriers for CDDP. Towards this aim, we synthesized the amphiphilic block copolymer poly(acrylic acid)-*b*-polystyrene (PAA-*b*-PS), which was then self assembled into polymeric micelles and subsequently transformed into SCKs by crosslinking the shell domain of the micelles *via* amidation chemistry. These micelles and SCKs contained carboxyl groups in the shell region of the nanostructures, which provided sites for complexation with CDDP.[114] The effects of crosslinking were studied by comparing the release kinetics of these CDDP-loaded micellar *vs*. SCK nanoparticles in PBS, in addition to their stabilities in aqueous milieu, *in vitro* cytotoxicities in OVCAR-3 ovarian cancer cells and RAW 264.7 mouse macrophages, and *in vitro* immunotoxicities in RAW 264.7 mouse macrophages.

2.2 Materials and methods

2.2.1. Materials

Cisplatin was purchased from Strem Chemicals, Inc. (Newburyport, MA). All other chemicals were purchased from Aldrich Chemical Co. (St. Louis, MO) and used without further purification unless otherwise noted. Slide-A-Lyzer dialysis cassettes (10 kDa molecular weight cut-off, MWCO) were purchased from Pierce Biotech. (Rockford, IL). The Spectra/Por Dialysis Membranes (MWCO 6-8 kDa) were purchased from Spectrum Laboratories, Inc (Rancho Dominguez, CA). Nanopure water (18 MΩ•cm) was acquired by means of a Milli-Q water filtration system, Millipore Corp. (Bedford, MA).

2.2.2 Instrumentation

^{1}H NMR and ^{13}C NMR spectra were recorded on Inova 300 or Mercury 300 spectrometer interfaced to a UNIX computer using VnmrJ software. Chemical shifts were referenced to the solvent residual signals.

FTIR spectra were recorded on an IR Prestige 21 system using a diamond ATR lens (Shimadzu Corp., Japan) and analyzed using IRsolution v. 1.40 software.

Gel permeation chromatography (GPC) was performed on a Waters Chromatography, Inc., 1515 isocratic HPLC pump equipped with an inline degasser, a model 2414 differential refractometer (Waters, Inc.), and four PLgel polystyrene-*co*-divinylbenzene gel columns (Polymer Laboratories, Inc.) connected in series: 5 μm Guard (50×7.5 mm), 5 μm Mixed C (300×7.5 mm), 5 μm 10^4 (300×7.5 mm), and 5 μm 500 Å (300×7.5 mm). The instrument was operated at 40 °C with tetrahydrofuran (THF) as eluent (flow rate

set to 1.0 mL/min). Polymer solutions were prepared at a known concentration (*ca.* 3 mg/mL) and an injection volume of 200 μL was used. Data collection and analysis was performed with the Breeze (version 3.30, Waters, Inc.) software. The system was calibrated with polystyrene standards (Polymer Laboratories, Amherst, MA).

Dynamic light scattering (DLS) measurements were conducted using Delsa Nano C (Beckman Coulter, Inc., Fullerton, CA) equipped with a laser diode operating at 658 nm. Size measurements were made in nanopure water ($n = 1.3329$, $\eta = 0.890$ cP at 25 ± 1 °C). Scattered light was detected at 165° angle and analyzed using a log correlator over 70 accumulations for a 3.0 mL sample in a glass sizing cell (4.0 mL capacity). The photomultiplier aperture and the attenuator were automatically adjusted to obtain a photon counting rate of ca. 10 kcps. Calculation of the particle size distribution and distribution averages was performed using CONTIN particle size distribution analysis routines. The peak averages of histograms from number distributions out of 70 accumulations were reported as the average diameters of the particles.

Glass transition temperatures (T_g) were measured by differential scanning calorimetry on a Mettler-Toledo DSC822® (Mettler-Toledo, Inc., Columbus, OH), with a heating rate of 10 °C/min. Measurements were analyzed using Mettler-Toledo Star^e v. 7.01 software. The T_g was taken as the midpoint of the inflection tangent, upon the third heating scan. Thermogravimetric analysis was performed under N_2 atmosphere using a Mettler-Toledo model TGA/SDTA851^e, with a heating rate of 10 °C /min. Measurements were analyzed by using Mettler-Toledo Stare v. 7.01 software.

Transmission electron microscopy (TEM) images were collected on a JEOL 1200EX operating at 100 kV and micrographs were recorded at calibrated magnifications using a SIA-15C CCD camera. A FEI Tecnai G2 F20 ST operated at 200 kV was also adopted to obtain high resolution TEM (HR-TEM) image, as well as the high-angle annular dark field imaging in the scanning TEM mode (HAADF-STEM). The samples as aqueous solutions (4 μL) were deposited onto carbon-coated copper grids, which were pre-treated by a glow discharge on a PELCO easiGlow™ to increase the surface hydrophilicity. Excess sample was wicked off using filter paper and the grids were allowed to dry in air overnight. For samples without platinum loading, a drop of 1% phosphotungstic acid (PTA) stain was then added, and allowed to stand for 30 seconds before excess stain was wicked away.

The concentration of platinum was measured by inductively coupled plasma-mass spectrometry (ICP-MS) on Perkin Elmer DRCII ICP-MS. The element/mass detected was ^{195}Pt and the internal standard used was ^{193}Hf.

2.2.3. Experimental procedures

Preparation of poly(*tert*-butyl acrylate), P*t*BA$_{90}$. A flame-dried 100-mL Schlenk flask equipped with a magnetic stir bar was charged with S-dodecyl-S′-(α,α′-dimethyl-α″-acetic acid) trithiocarbonate (DDMAT, 0.547 g, 1 *eq*.), *tert*-butyl acrylate (*t*-BA, 57.7 g, 300 *eq*.), azobisisobutyronitrile (AIBN, 12.3 mg, 0.05 *eq*.), and 2-butanone (27 mL). The flask was sealed with a rubber septum and allowed to stir for 10 min at room temperature to ensure homogeneous mixing. The reaction mixture was degassed by several freeze-pump-thaw cycles (N>3), after which the flask was allowed to return to

room temperature and was allowed to stir for an additional 10 min. The flask was then immersed into a pre-heated oil bath at 52 °C to start the polymerization. The polymerization was monitored by analyzing aliquots collected at pre-determined times by ^{1}H-NMR spectroscopy. As the expected monomer conversion was reached, after *ca*. 3 h depending on the desired block chain lengths, the polymerization was quenched by quick immersion of the reaction flask into liquid N_2 and opening to air. THF (20 mL) was added to the reaction flask and the polymer was purified by precipitation into 2 L of a methanol/ice (1:1) mixture four times. The precipitants were collected and dried under vacuum overnight to afford the final product as a yellow powder (13.6 g, 31.3% conversion, 73% yield). GPC: M_n = 12400 Da, PDI = 1.11. IR: 3026–2885, 1720, 1450, 1365, 1250, 1142, 841, 749 cm^{-1}. ^{1}H NMR ($CDCl_3$, 300 MHz): δ 0.86 (t, J = 6 Hz, $C\boldsymbol{H}_3CH_2$–), 1.13–1.90 (br, –CH$C\boldsymbol{H}_2$– of the polymer backbone, alkyl chain of initiator, and HOOCC(C$\boldsymbol{H}_3)_2$–), 1.28–1.58 (br, C$\boldsymbol{H}_3$C), 2.12–2.38 (br, –C$\boldsymbol{H}CH_2$– of the polymer backbone), 3.31 (t, J = 2 Hz, –SCSC$\boldsymbol{H}_2$–), 4.62–4.72 (br, –$CH_2C\boldsymbol{H}$S) ppm. ^{13}C NMR ($CDCl_3$, 75 MHz): δ 28.2, 34.0–38.5, 41.1–42.9, 80.1–81.0, 173.6–174.6 ppm. DSC: T_g = 47 °C. TGA in N_2: 200–260 °C, 47% mass loss; 260–480 °C, 41% mass loss, 12 % mass remaining above 480 °C.

Preparation of poly(*tert*-butyl acrylate)-*b*-polystyrene, P*t*BA$_{90}$-*b*-PS$_{120}$. To a flame-dried 50 mL Schlenk flask equipped with a magnetic stir bar, P*t*BA$_{90}$ (2.48 g, 1 *eq*.), styrene (16.6 g, 798 *eq*. based on desired polymer chains), AIBN (1.6 mg, 0.05 *eq*.) and 1,4-dioxane (4.2 mL) were added. The flask was sealed with a rubber septum and allowed to stir for 10 min. The reaction mixture was then degassed by several freeze-

pump-thaw cycles (N>3). After allowing the flask to return to room temperature, it was allowed to stir in a pre-heated oil bath at 60 °C to start the polymerization. The polymerization was monitored by analysis of aliquots taken at various times by ^{1}H-NMR spectroscopy. The polymerization was quenched at *ca*. 50 h (depending on desired block chain lengths) by immersing the flask in liquid nitrogen and opening to air. The product was purified by precipitation into methanol/water (5:1) mixture three times and dried under vacuum overnight to yield a pale yellow powdery product (4.85 g, 16.7% conversion, 92% yield). GPC: M_n = 25300 Da, PDI = 1.13. IR: 3109–2792, 1728, 1489, 1450, 1365, 1250, 1149, 848, 756 cm^{-1}. ^{1}H NMR (CD_2Cl_2, 300 MHz): δ 0.89 (t, J = 6 Hz, $C\boldsymbol{H}_3CH_2$–), 1.15–2.13 (br, –CH$C\boldsymbol{H}_2$– of the polymer backbone, alkyl chain of initiator, and HOOCC(C$\boldsymbol{H}_3$)$_2$-), 1.12–1.64 (br, C$\boldsymbol{H}_3$C), 2.12–2.36 (br, $C_5H_5C\boldsymbol{H}CH_2$– of the polymer backbone), 3.20–3.32 (br, -SCSC$\boldsymbol{H}_2$–), 6.34–7.56 (br, Ar–H) ppm. ^{13}C NMR (CD_2Cl_2, 75 MHz): δ 28.4, 36.1–38.2, 40.6–43.0, 80.9, 125.8–129.4, 145.2-147.0, 174.4–175.2 ppm. DSC: $(T_g)_1$ = 48 °C, $(T_g)_2$ = 102 °C. TGA in N_2: 190–270 °C, 16% mass loss; 270–470 °C, 54% mass loss, 30 % mass remaining above 470 °C.

Preparation of poly(acrylic acid)-*b*-polystyrene, PAA$_{90}$-*b*-PS$_{120}$. A flame-dried 100 mL round bottom flask equipped with a magnetic stir bar was charged with P*t*BA$_{90}$-*b*-PS$_{120}$ (1.00 g) and dichloromethane (4 mL). Trifluoroacetic acid (TFA, 47 mL, 162 *eq*.) was added to the stirring solution and the reaction was allowed to stir 24 h at room temperature, after which the solvent was removed under vacuum. The crude product was resuspended in 20 mL of THF and transferred to a pre-soaked dialysis tubing (MWCO *ca*. 6–8 kDa), and dialyzed against nanopure water for 3 days. The solution

was then lyophilized to yield a yellowish solid (0.791 g, 95% yield). IR: 3600–2400, 1708, 1492, 1451, 1238, 1177, 1067, 1029, 754, 696 cm^{-1}. ^{1}H NMR (DMSO-d_6, 300 MHz): δ 1.02-1.08 (m, $C\boldsymbol{H}_3CH_2$–), 1.00–2.02 (br, –CH$C\boldsymbol{H}_2$– of the polymer backbone, alkyl chain of initiator, and HOOCC(C$\boldsymbol{H}_3$)$_2$-), 2.09–2.39 (br, $C_5H_5C\boldsymbol{H}CH_2$– of the polymer backbone), 2.71–2.73 (br, –SCSC$\boldsymbol{H}_2$–), 6.29–7.39 (br, Ar–H) ppm. ^{13}C NMR (DMSO-d_6, 75 MHz): δ 34.2–36.8, 40.1–41.6, 124.7–128.6, 144.8-145.8, 175.5-176.0 ppm. DSC: $(T_g)_1$ = 103 °C, $(T_g)_2$ = 145 °C. TGA in N_2: 190–290 °C, 5% mass loss; 290–490 °C, 69% mass loss 26 % mass remaining above 490 °C.

Preparation of micelles and shell crosslinked knedel-like (SCK) nanoparticles. Micelles: PAA_{90}-*b*-PS_{120} (*ca*. 25 mg) was dissolved in DMF (25 mL) in a 100 mL round bottom flask and allowed to stir for 30 min at room temperature. To this solution, an equal volume of nanopure water was added dropwise *via* a syringe pump over a period of 2 h. The reaction mixture was allowed to stir overnight at room temperature and dialyzed against nanopure water for 2 days in a presoaked dialysis tubing (MWCO *ca.* 6–8 kDa) to afford a micelle solution with a final polymer concentration of *ca*. 0.22 mg/mL.

SCKs: To the micelle solution of PAA-*b*-PS was added a solution of 2,2′-(ethylenedioxy)diethylamine (EDDA) in nanopure water (*ca.* 2 mg/mL, 0.05 or 0.15 *eq*., with respect to acid residues, nominal 10% or 30% crosslinking, respectively) dropwise, and the solution was allowed to stir for 2 h. To this solution, 1-[3´-(dimethylamino)propyl]-3-ethyl-carbodiimide methiodide (EDCI) in nanopure water (*ca.* 1 mg/mL, 0.15 or 0.30 *eq*., with respect to acid residues) was added dropwise over 20

min and the resulting mixture was allowed to stir overnight before dialysis against nanopure water for 2 days in presoaked dialysis tubing (MWCO *ca*. 6–8 kDa) to afford SCK solutions with a final polymer concentration of *ca*. 0.22 mg/mL.

Loading cisplatin into micelles and SCK nanoparticles. In a typical experiment, to a vial containing a magnetic stir bar and micelle or SCK solution (10 mL, polymer PAA_{90}-*b*-PS_{120} concentration 0.22 mg/mL, acid residues had been neutralized by addition of 0.1 M $NaOH_{(aq)}$), a solution of cisplatin (1.0 mg/mL in water, 0.5 molar ratio with respect to the PAA carboxylate residues) was added dropwise. The solution was stirred for three days and then dialyzed against nanopure water at room temperature to remove free cisplatin. Dynamic light scattering (DLS), transmission electron microscopy and inductively coupled plasma mass spectrometry (ICP-MS) were used to measure the particle dimensions and platinum concentrations, respectively.

Release studies of cisplatin-loaded micelles and SCK nanoparticles. In a typical procedure, a solution of CDDP-loaded micelles or SCKs (0.9 mL) was transferred into a presoaked dialysis cassette (Slide-A-Lyzer, 10 kDa MWCO, Pierce Biotechnology, Rockford IL). The cassette was allowed to stir in a beaker containing PBS (180 mL, 10 mM phosphate, 137 mM NaCl, pH 7.4 at 37 ^{o}C), and samples (2 mL) were collected from the dialysate at pre-determined times and analyzed by ICP-MS, with fresh PBS (2 mL) added back into the beaker.

***In vitro* cytotoxicity assays**. OVCAR-3 ($5x10^3$ cells/well) or RAW 264.7 ($2x10^4$ cells/well) cells were plated in a 96-well plate in RPMI media and Dulbecco's Modified Eagle Medium (DMEM) (20% and 10% fetal bovine serum, for the OVCAR-3 and

RAW 264.7, respectively, and 1% penicillin/streptomycin). Cells were incubated at 37 °C in a humidified atmosphere containing 5% CO_2 for 24 h to adhere. Then, the medium was replaced with a fresh media 1 h prior to the addition of the various formulations at concentrations that ranged from $7x10^{-4}$ to 150 μM of cisplatin. For each well, 20 μL of the formulations was added to 100 μL of the medium. The cells were incubated with the formulations for 72 h and washed once with PBS and 100 μL of the complete media was added to the cells. MTS combined reagent (20 μL) was added to each well (Cell Titer 96® Aqueous Non-Radioactive Cell Proliferation Assay, Promega Co., Madison, WI). The cells were incubated with the reagent for 2 h at 37 °C in a humidified atmosphere containing 5% CO_2 protected from light. Absorbance was measured at 490 nm using SpectraMax M5 (Molecular Devices Co., Sunnyvale, CA). The cell viability was calculated based on the relative absorbance to the control untreated cells. The IC_{50} values were calculated using GraphPad Prism four-parameter fit, considering the 0% and 100% viabilities are for media control (no cells) and cells with no treatment, respectively.

Multiplex assay. RAW 264.7 ($2x10^4$ cells/well) cells were plated in a 96-well plate in DMEM, as described in the previous section. Cells were incubated at 37 °C in a humidified atmosphere containing 5% CO_2 for 24 h to adhere. Then, the medium was replaced with a fresh media 1 h prior to the treatment with medium (control), micelles and SCKs of varying degrees of crosslinking (10 and 30%) at concentrations of 32 μg/mL. The supernatants were then collected and centrifuged for 10 min at 13,000 rpm. Serial dilutions of standards of cytokines were also prepared in the same diluent utilized

for the samples (*i.e.* cell-culture medium). Control, standards and nanoparticle-treated samples (50 µL) were incubated with antibody-conjugated magnetic beads for 30 min in the dark. After washing, the detection antibody was added to the wells and incubated in the dark for 30 min under continuous shaking (300 rpm). After washing, streptavidin-phycoerythrin was added to every well and incubated while protected from light for 10 min under the same shaking conditions. Finally, after several washings and re-suspension in the assay buffer and shaking, the expression of the mouse cytokines, interleukin (IL)-1α, IL-1β, IL-2, IL-3, IL-4, IL-5, IL-6, IL-9, IL-10, IL-12 (P40), IL-12 (P70), IL-13, IL-17, Eotaxin, granulocyte-colony-stimulating factor (G-CSF), granulocyte macrophage-colony-stimulating factor (GM-CSF), interferon-γ (IFN-γ), keratinocyte-derived chemokine (KC), monocyte chemotactic protein (MCP)-1, macrophage inflammatory protein (MIP)-1α, MIP-1β, regulated upon activation normal T-cell expressed and presumably secreted (RANTES) and tumor necrosis factor-α (TNF-α) was measured immediately using Bio-plex 200 system with HTF and Pro II Wash station and the data were analyzed using the Bio-plex Data Pro software (Bio-Rad Laboratories, Inc., Hercules, CA)..

2.3 Results and discussions

The amphiphilic block copolymer poly(acrylic acid)-*b*-polystyrene (PAA_{90}-*b*-PS_{120}) was synthesized according to the previously reported method (Figure 2.1a).[45] Reversible addition−fragmentation chain transfer (RAFT) polymerization, a well-studied controlled radical polymerization technique that can be used to generate complex polymer

structures, was employed to prepare the amphiphilic block copolymer precursor.[121] Briefly, poly(*tert*-butyl acrylate)$_{90}$ (P*t*BA$_{90}$) was synthesized by polymerization of *tert*-butyl acrylate (*t*-BA), using S-1-dodecyl-S′-(α,α′-dimethyl-α″-acetic acid) trithiocarbonate (DDMAT) as the chain transfer agent and azobisisobutyronitrile (AIBN) as the initiator. Chain extension with styrene from the macrotransfer agent P*t*BA$_{90}$ was conducted to afford the diblock copolymer poly(*tert*-butyl acrylate)-*b*-polystyrene (P*t*BA$_{90}$-*b*-PS$_{120}$). Gel permeation chromatographic (GPC) analysis showed that both P*t*BA$_{90}$ and P*t*BA$_{90}$-*b*-PS$_{120}$ exhibited mono-modal molecular weight distributions with low polydispersity indices (1.11 and 1.13, respectively, Figure 2.1b). The decreased retention time of P*t*BA$_{90}$-*b*-PS$_{120}$, relative to P*t*BA$_{90}$, demonstrated the increase of apparent molecular weight. The degrees of polymerization of these polymers were finally confirmed by ^{1}H NMR spectroscopy, which were in agreement with the GPC

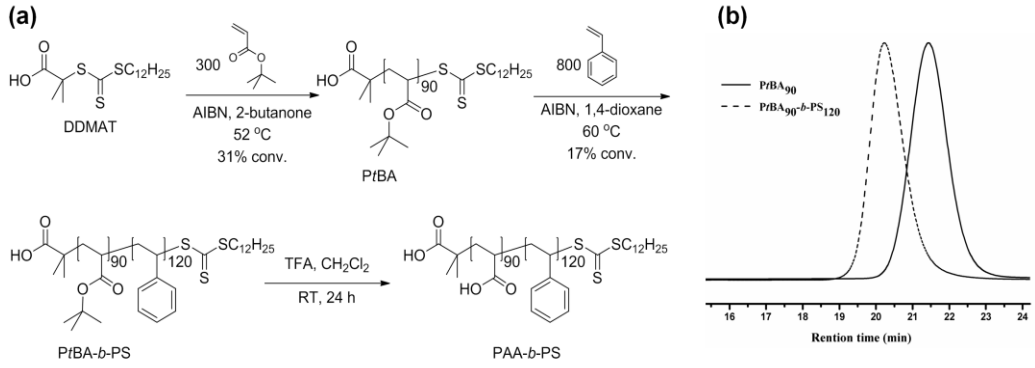

Figure 2.1. (a) Synthesis of PAA-*b*-PS copolymer *via* sequential RAFT polymerizations of *tert*-butyl acrylate and styrene, followed by the removal of the *tert*-butyl protecting groups. (b) Gel permeation chromatography traces of P*t*BA$_{90}$ homopolymer (solid line) and P*t*BA$_{90}$-*b*-PS$_{120}$ diblock copolymer (dashed line).

analysis. The removal of *tert*-butyl protecting groups of the P*t*BA$_{90}$-*b*-PS$_{120}$ by using trifluoroacetic acid generated the final polymer PAA$_{90}$-*b*-PS$_{120}$.

The SCKs were prepared by supramolecular assembly of PAA$_{90}$-*b*-PS$_{120}$ into micelles, followed by amidation-based shell crosslinking (Figure 2.2). *N,N*-dimethylformamide (DMF) is a good solvent for both the PAA and the PS blocks, and was chosen to dissolve the diblock polymer. Subsequent addition of water directed the hydrophobic PS segments to aggregate and form the core domains of the micelles, while the hydrophilic PAA blocks formed the shell domains. The SCKs were then constructed by crosslinking

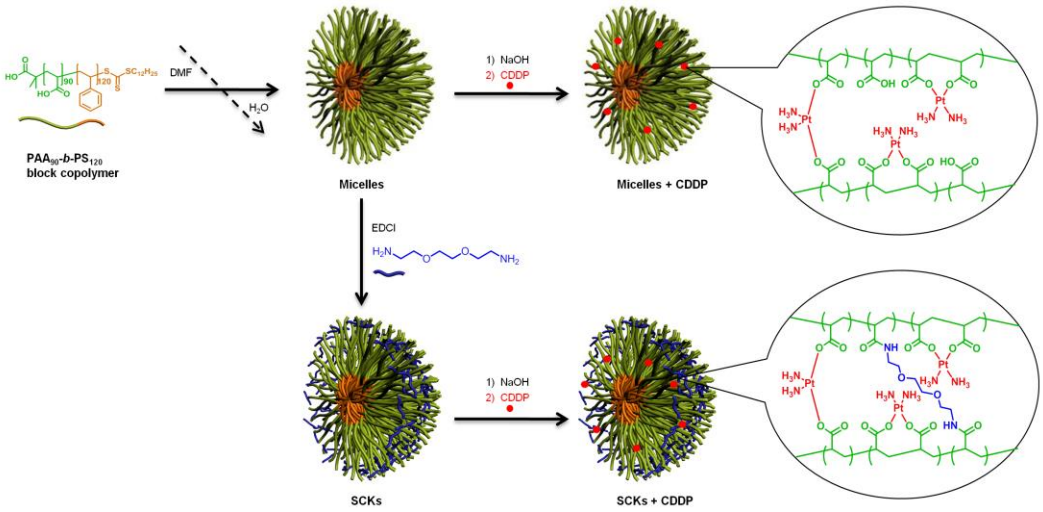

Figure 2.2. Preparation of SCKs *via* self assembly of amphiphilic block copolymer PAA$_{90}$-*b*-PS$_{120}$ followed by crosslinking. Cisplatin incorporation into each of the micelles and SCKs was conducted *via* polymer-metal complex formation.

the shell region of these micelles with 2,2′-(ethylenedioxy)diethylamine (EDDA) in the presence of 1-[3´-(dimethylamino) propyl]-3-ethyl-carbodiimide methiodide (EDCI). SCKs having nominally 10 and 30% crosslinking were prepared by employing 5 and 15

mol% of the diamine, respectively, relative to the acrylic acid residues of the PAA chain segments.

Loading of the micelles and SCKs with CDDP was then performed to investigate the influence of shell crosslinking on the loading capacities and release kinetics. The coordination bonds between chloride ligands and platinum are usually labile and subject to ligand substitution reactions, therefore, in this study, the carboxylic acid residues from the PAA regions of the micelles and SCKs were first deprotonated by reacting with equal molar amounts of sodium hydroxide to expedite the substitution process.[114] CDDP in water was then added to the aqueous solutions of micelles or SCKS, which allowed for the CDDP chloride ligands to undergo displacement by carboxylate groups in the nanoparticle shell domains and also with water, to coordinate Pt within the micelle and SCK shells while also generating various aqua derivatives in the aqueous environment.[115] Since CDDP has two available sites for substitutions, it may crosslink two polymer chains or form an intramolecular loop (Figure 2.2). After removal of excess CDDP by dialysis, the loaded amount of CDDP was determined by inductively-coupled plasma mass spectrometry (ICP-MS) (Table 2.1). For micelles, the loading was as high as 48% (w/w, relative to the mass of PAA_{90}-*b*-PS_{120} block copolymer precursors), while a lower loading was found with SCKs. Moreover, the loading decreased with increasing the degree of crosslinking, for example, SCKs with 10% crosslinking (SCKs-10) had a 32% (w/w) loading, which was higher than that of SCKs with 30% crosslinking (SCK-30, 26% loading, w/w), but lower than that of micelles. This trend can be explained by the decrease in the concentration of carboxylate binding

sites available for ligand substitution, caused by their consumption during crosslinking; the higher the crosslinking degree, the fewer carboxylate groups remaining for ligand substitution.

Table 2.1. CDDP loading into micelles and SCKs.

Nanoparticles	Degree of crosslinking	CDDP conc. (mg/mL)	Polymer conc.(mg/mL)	CDDP loading (wt %)
Micelles	0	0.11	0.23	48
SCKs-10	10	0.070	0.22	32
SCKs-30	30	0.055	0.21	26

The sizes and size distributions of these micelles and SCKs were characterized by dynamic light scattering (DLS) and transmission electron microscopy (TEM). As indicated by DLS histograms, all particles showed mono-modal and narrow hydrodynamic diameter distributions (Figure 2.3). The number-averaged hydrodynamic diameters of micelles, SCKs-10, SCKs-30, micelles-CDDP, SCKs-10-CDDP and SCKs-30-CDDP were 27 ± 8 nm, 23 ± 7 nm, 24 ± 7 nm, 17 ± 5 nm, 18 ± 5 nm, and 23 ± 6 nm, respectively. Bright-field TEM images of these nanoparticles were uniform with diameters of approximately 20 nm (Figure 2.4). Since CDDP was introduced to these nanoparticles by ligand exchange with carboxylate groups, platinum predominantly bonded to the shell regions, which was clearly observed in the TEM analysis. In the images of Figure 2.3d, 3e, 3f and especially the image with the high-magnification 2.3g, the peripheral regions of these nanoparticles were darker than their cores, indicating higher concentrations of platinum in the shell

regions, since no staining solutions were used in the TEM sample preparation. In addition, some elemental platinum was observed as <2 nm nanoparticles surrounding the micelles or SCKs, which was measured to have metallic Pt lattice spacing $d_{Pt(111)}$ = 2.3 Å (Figure 2.4g), indicating some Pt(II) had been reduced in the polymeric nanoparticle matrices.[122-124] Figure 2h is an image obtained in the high-angle annular dark field imaging in the scanning TEM mode (HAADF-STEM), where bright round rings were observed, serving as further evidence of shell loading of cisplatin.

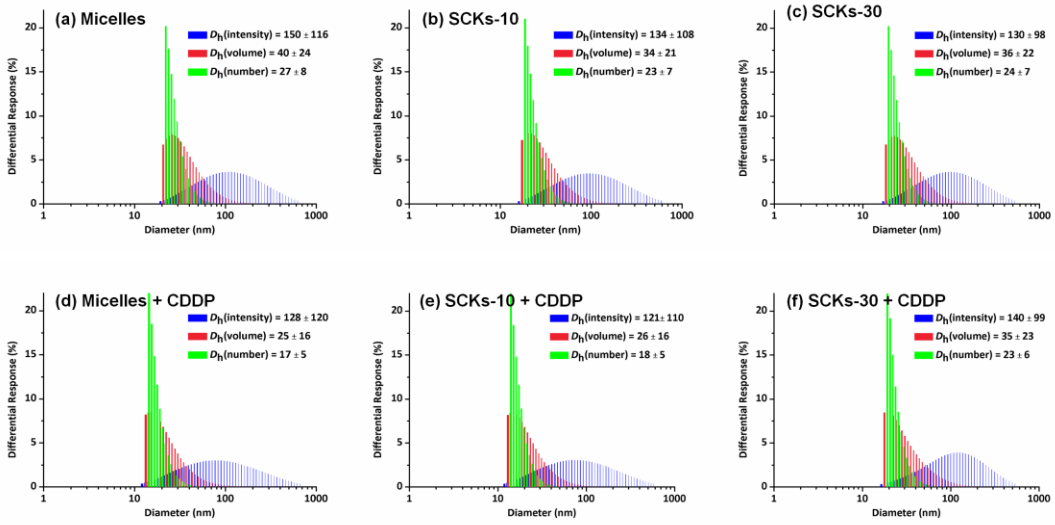

Figure 2.3. Characterization of nanoparticles by DLS. DLS histograms of intensity-averaged (D_h(intensity)), volume-averaged (D_h(volume)), number-averaged hydrodynamic diameters (D_h(number)): (a) micelles, (b) SCKs-10, (c) SCKs-30, (d) CDDP-loaded micelles, (e) CDDP-loaded SCKs-10, and (f) CDDP-loaded SCKs-30, each in nanopure water.

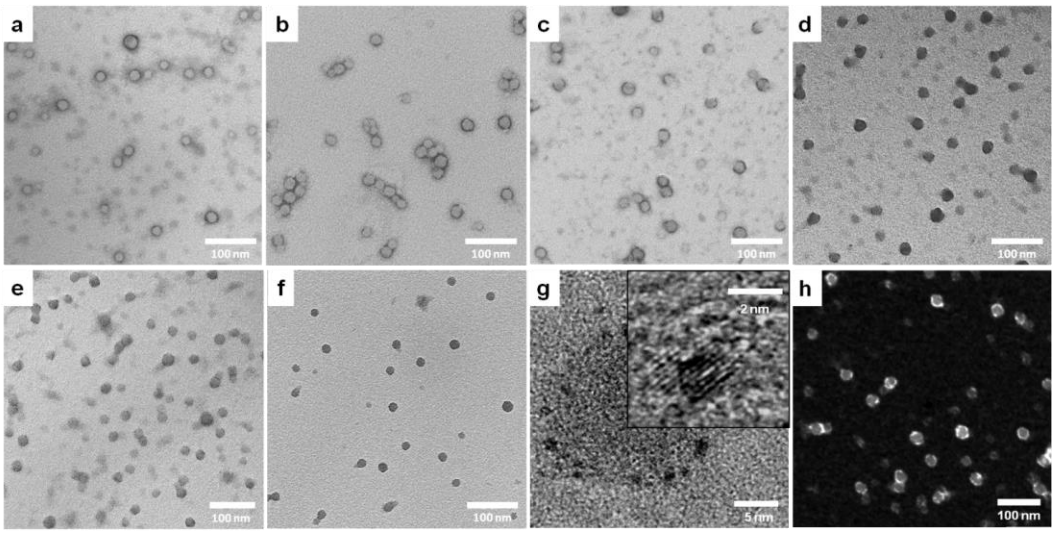

Figure 2.4. Transmission electron microscopy (TEM) images of (a) micelles, D_{av} =19 ± 3 nm, (b) SCKs-10, D_{av} =20 ± 3 nm, (c) SCKs-30, D_{av} =20 ± 3 nm, (d) CDDP-loaded micelles, D_{av} =19 ± 3 nm, (e) CDDP-loaded SCK-10, D_{av} =19 ± 2 nm, (f) CDDP-loaded SCKs-30, D_{av} =17 ± 3 nm, and (g) CDDP-loaded SCKs-10 (high magnification). (h) Scanning TEM image of CDDP-loaded SCKs. Samples a, b, c were stained by phosphotungstic acid, and the remaining samples were not stained. The average diameters were calculated after measuring more than 100 particles.

Release of platinum from micelles and SCKs was evaluated by monitoring the increase of platinum concentration in PBS at pH 7.4, after escaping from dialysis cassettes (Figure 2.5). The high concentration of chloride anions in PBS is necessary for the effective release of platinum, whereby carboxylate ligands are substituted by chloride anions *via* ligand exchange reactions.[109,117] Regardless of crosslinking degrees, all CDDP-loaded nanoparticles released the platinum in a sustained and slow manner over 5 days. Previously, we had observed that shell crosslinks inhibited drug transport through the shell, giving slower release of doxorubicin from PAA-*b*-PS based SCKs compared to the corresponding micelle precursors.[41,45] Interestingly, there was no noteworthy difference in CDDP release kinetics among micelles and SCKs, probably

because CDDP was incorporated in the shell and served as additional crosslinkers within either type of nanoparticles. As a control experiment, the release of free CDDP from the dialysis cassette, for solutions with similar Pt concentration as the nanoparticle loaded systems, was found to be complete within 2 h.

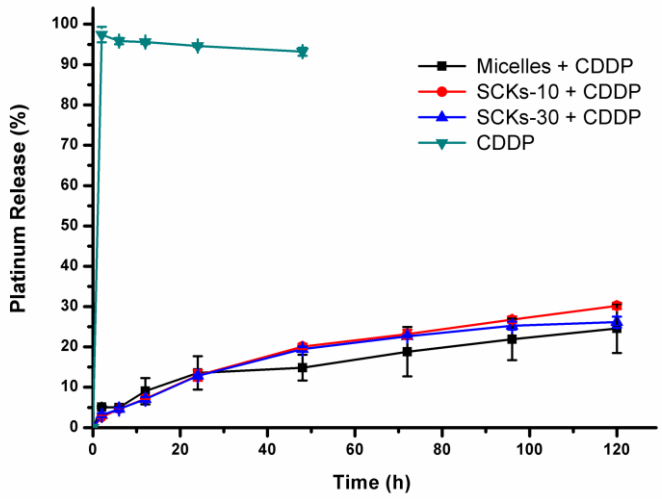

Figure 2.5. Release of CDDP that was either free or loaded into micelles and SCKs (PBS, pH 7.4, 37 ºC), measured by ICP-MS of aliquots collected from the dialysate over five days.

The apparent stability of free CDDP and CDDP-loaded micelles and SCKs was qualitatively determined by incubating the aqueous solutions at room temperature while being stirred in the dark. After 5 days, there were many black precipitates on the stir bar in the sample for which free CDDP was dissolved in nanopure water (Figure 4c), while almost none were observed in the CDDP-loaded micelle (Figure 4a) and SCK samples (Figure 4b). When CDDP was dissolved in water, it converted into various aqua

derivatives, among which hydroxide-bridged diplatinum complexes could be responsible for formation of the irreversible black precipitates.[115,125] On the other hand, the CDDP-loaded polymer-metal complexes were stable in nanopure water, and only minor amounts of platinum species were released and underwent decomposition.

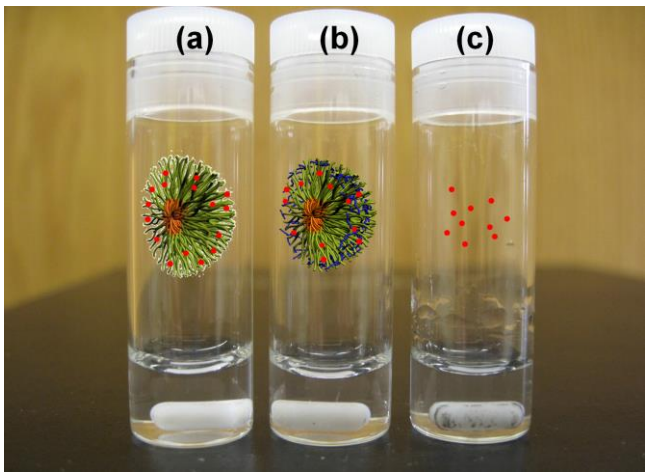

Figure 2.6. Apparent physical stability of the CDDP-loaded (a) micelles (0.11 mg/mL) and (b) SCKs-10 (0.07 mg/mL), as compared to (c) the free CDDP (0.10 mg/mL). All samples were incubated at room temperature and protected from light for 5 days. All concentrations correspond to the cisplatin concentrations in solutions in nanopure water.

The cytotoxicities of CDDP and CDDP-loaded nanoparticles were determined *in vitro* by using OVCAR-3 ovarian cancer cells and RAW 264.7 mouse macrophages (Table 2.2). Both the CDDP-loaded micelles and SCKs showed higher IC_{50} values than that measured for free CDDP against both cell lines, which was consistent with results of other reported CDDP-loaded polymeric micelle systems.[11,115,118] The obvious reason is the slow release of platinum. As shown in Figure 2.5, only *ca*. 20% of platinum was released after 72 h, in other words, the actual available

platinum was far less than the amount available with the free CDDP solution. Worth noting, the CDDP-loaded SCKs-10 showed higher cytotoxicity compared to micelles, which may result from the possible higher cellular uptake induced by crosslinking.[117] However, the advantage of crosslinking in this case should be treated cautiously, since the crosslinking also decreased the loading capacity of the nanoparticles, for instance, the SCKs-10 only had *ca.* 60% loading capacity, in comparison to the micelles. In addition, the RAW 264.7 mouse macrophages seemed to be more sensitive to platinum-based formulations than were the OVCAR-3 cancer cells. The polymers themselves did not induce any toxicity on both cell lines at the tested concentrations.

Table 2.2. IC50 values for free CDDP *vs.* CDDP-loaded micelles and SCK nanoparticles, measured against two cell lines.

Formulation	IC_{50} (μM)	
	OVCAR-3	RAW 264.7
CDDP	0	0.11
Micelles	10	0.070
SCKs-10	30	0.055

The immunotoxicities of nanoparticles were evaluated by a multiplex assay, as described previously.[126] Briefly, the expression levels of 23 cytokines were measured upon treatment of RAW 264.7 mouse macrophages for 24 h with the micelles and SCKs of 10% and 30% crosslinking at concentrations of 32 μg/mL. The CDDP-loaded nanoparticles also were tested but at non-cytotoxic concentrations (0.6 μM CDDP and 0.08 μg/mL of nanoparticles). As expected, the nanoparticles, either free or loaded with

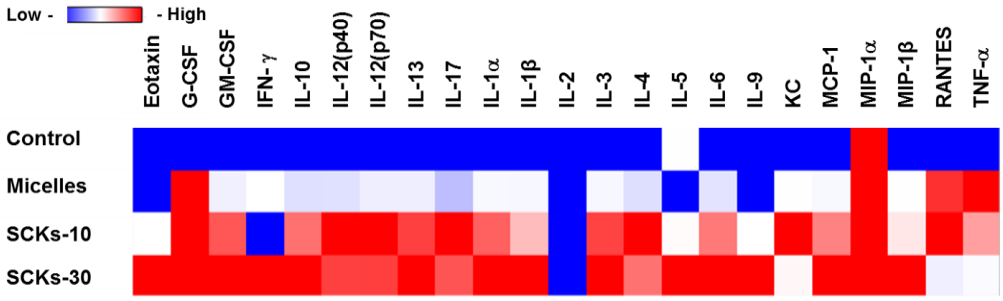

Figure 2.7. Heat map of the relative expression of the following mouse cytokines, interleukin (IL)-1α, IL-1β, IL-2, IL-3, IL-4, IL-5, IL-6, IL-9, IL-10, IL-12 (P40), IL-12 (P70), IL-13, IL-17, Eotaxin, granulocyte-colony-stimulating factor (G-CSF), granulocyte macrophage-colony-stimulating factor (GM-CSF), interferon-γ (IFN-γ), keratinocyte-derived chemokine (KC), monocyte chemotactic protein (MCP)-1, macrophage inflammatory protein (MIP)-1α, MIP-1β, RANTES (regulated upon activation normal T-cell expressed and presumably secreted) and tumor necrosis factor-α (TNF-α), following the treatment of RAW 264.7 cells with medium (control), micelles and SCKs of varying degrees of crosslinking (10 and 30%) at 32 μg/mL.

CDDP, were not immunotoxic at these low concentrations. The micelles and SCKs led to higher secretion of cytokines at 32 μg/mL. The expression of the following mouse cytokines, GM-CSF, IL-3, IL-10, IL-12 (P40), IL-12 (P70), IL-13, IL-1α, IL-1β, KC, MCP-1, MIP-1β and RANTES were significantly higher for cells treated with micelles and SCKs, as compared to the control-untreated cells. Consistently, there was an enhancement in the secretion of cytokines upon increasing the degree of crosslinking (Figure 2.7 and 2.8). The SCKs with 30% crosslinking induced higher release of IL-10 (p = 0.001), IL-12 (P70) (p = 0.007), IL-13 (p = 0.008), IL-1α (p = 0.02) and IL-3 (p = 0.04) than the non-crosslinked micelles. The latter induced higher secretion than the SCKs for only one cytokine (RANTES, p = 0.007). The higher immunotoxicity of the crosslinked nanoparticles may be, in part, due to the amine residues from incomplete crosslinking *via* the amidation chemistry.[126,127]

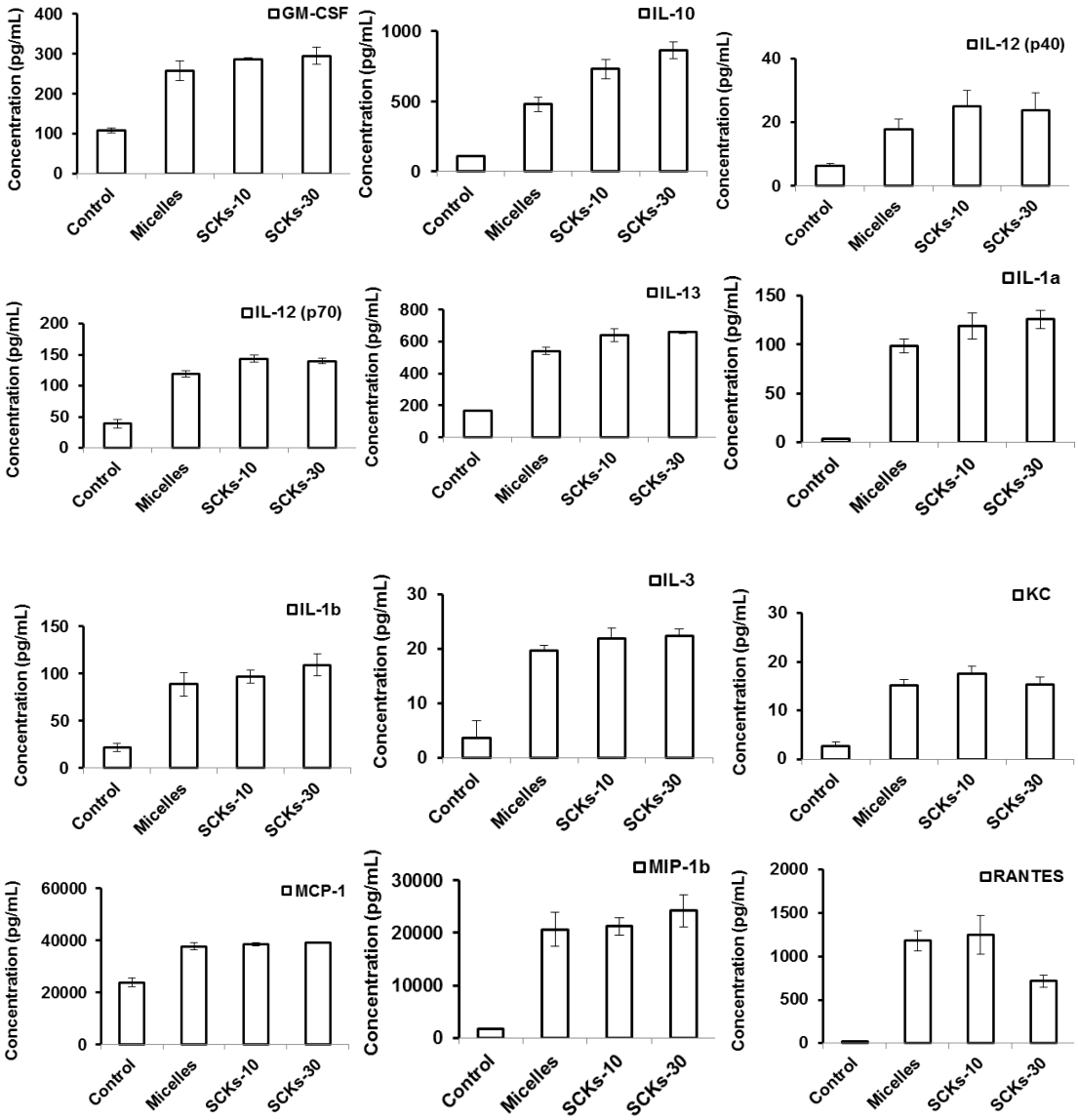

Figure 2.8. The expression of the mouse cytokines, GM-CSF, IL-3, IL-10, IL-12 (P40), IL-12 (P70), IL-13, IL-1α, IL-1β, KC, MCP-1, MIP-1β and RANTES following the treatment of RAW 264.7 cells with media (control), micelles and SCKs of varying degrees of crosslinking (10 and 30%) at 32 μg/mL.

2.4 Conclusions

In this study, we have demonstrated the feasibility of incorporation of CDDP into the shells of micelles and SCKs by forming polymer-metal complexes with ultra-high

loading, which was decreased upon increasing the degree of crosslinking. Nanosized particles with unimodal size distribution and low polydispersity were formed. The nanoparticles imparted significant physical stability to the incorporated drug and allowed control over its release from the polymeric particles. Since the toxicities of CDDP are related to the maximum plasma concentration of free drug, the slow and sustained release of CDDP can possibly reduce its systemic toxicity.[112] These CDDP-loaded nanoparticles exhibited cell killing abilities *in vitro* that are comparable with reported micellar formulations. Crosslinking of polymer micelles are often considered to be beneficial for improved stability against dilution. Here, with Pt-complexation, Pt provides complexation-based crosslinks and additional covalent crosslinks diminish sites for Pt complexation, giving lower wt% loading of drug. Although cytotoxicity increased with covalent crosslinking, the lower drug loading counterbalances the overall effect. In addition, upon incubating the micellar and crosslinked nanoparticles with the mouse macrophages, the crosslinked nanoparticles resulted in higher *in vitro* immunotoxicity. Therefore, any covalent crosslinking within future nanoparticle designs should be incorporated into an alternate region within the nanoparticle framework, to avoid consuming functionalities required for the drug-complexation.

Though CDDP-loaded micelles and SCKs showed decreased cytotoxicity *in vitro* mainly due to the slow release kinetics, they may provide superior efficacy than free CDDP *in vivo* by enhancing the accumulation of the drug in tumor tissues *via* the enhanced permeability and retention effect.[20] In addition, the nanostructures allow

an opportunity for active targeting by decorating their surfaces with active targeting ligands, such as folic acid or an aptamer.[128-130] Also, it is expected that CDDP-loaded nanoparticles prepared in this study may show reduced side effects including nephrotoxicity, neurotoxicity, and ototoxicity, as compared to the free drug.[10,11] In addition, in this work, the CDDP was loaded in the shell, and thus the core of the nanoparticles remains available for incorporation of other hydrophobic drugs, which could be utilized for combinational therapy. For instance, our previous results have demonstrated that DOX and PTX can be loaded at the core-shell interface or into the core of SCKs effectively.[45,120] Therefore, the co-delivery of drugs that operate by different cellular mechanisms within one nanoparticle is possible, which is a promising approach for future cancer therapy that has the potential to exert synergistic efficacy and reduce side effects.[125,131,132]

CHAPTER III

IMPROVING PACLITAXEL DELIVERY: IN VITRO AND IN VIVO CHARACTERI-ZATION OF PEGYLATED POLYPHOSPHOESTER-BASED NANOCARRIERS[*]

3.1 Introduction

Nanomedicines have great potential to provide effective treatment against devastating diseases, by providing sustained release of significant quantities of therapeutic agents locally, especially when the route of administration allows for direct access to the diseased tissues. Our interest focuses on the design of polymer-based nanotherapeutics towards the treatment of osteosarcoma lung metastases. Osteosarcoma is the most common primary cancer of bone in children and adolescents, with a peak incidence in adolescence (age range: <5 to ~40 years), no proven etiology and a high fatality rate (70% survival at 5 years for non-metastatic patients, and <30% for those presenting with metastasis).[77,78] The most common site of metastasis is the lung, followed by other bones, with approximately 40% of patients presenting with overt metastasis, and 90% estimated to have micrometastatic disease at diagnosis.[79,80] Osteosarcoma is treated with

[*] Reprinted (adapted) with permission from "Improving paclitaxel delivery: *In vitro* and *in vivo* characterization of PEGylated polyphosphoester-based nanocarriers" by Zhang, F.; Zhang, S.; Pollack, S. F.; Li, R.; Gonzalez, A. M.; Fan, J.; Zou, J.; Leininger, S. E.; Pavía-Sanders, A.; Johnson, R.; Nelson, L. D.; Raymond, J. E.; Elsabahy, M.; Hughes, D. M. P.; Lenox, M. W.; Gustafson, T. P.; Wooley, K. L., *J. Am. Chem. Soc.* 2015*, 137,* 2056-2066. Copyright 2015 American Chemical Society.

combination chemotherapy (believed essential to eliminate micrometastatic disease) and complete surgical excision of the primary tumor (either amputation or limb salvage).[81,82] Once micrometastases grow into recurrent, overt disease, tumors are often resistant to conventional chemotherapy, and unresectable recurrent disease is uniformly fatal.[81,83]

It has been demonstrated that drugs delivered to the respiratory tract in liposomal formulation resulted in high pulmonary drug concentration, reduced systemic toxicity, and reduced dosage requirements compared with parenteral and oral administration.[95-97] Standard delivery formulations for paclitaxel (PTX) are generally administered intravenously, resulting in rapid elimination of PTX and multiple undesirable side effects.[133] Further, the poor solubility of this drug, together with the need to dissolve it in toxic carriers prior to delivery, limits the ability to deliver maximally effective doses to patients. To improve efficacy while minimizing systemic toxicity and harmful side effects, it has been suggested that targeting of PTX to the site of disease *via* aerosol-based delivery would be desirable, and may hold great potential. Unfortunately, the unmodified drug's solubility and overall stability at the high concentrations necessary for such administration remains a hurdle to the success of such delivery methods.[134] Our hypothesis is that local inhalation-based delivery of high quantities of the chemotherapeutic agent PTX will be effective in the treatment of lung tumors, with degradable polymer-based nanoparticles being able to overcome key challenges of packaging and transport of sufficient drug quantities directly to the site of the metastatic disease, as well as extravasation of the delivery vehicle from the lungs and secondary organs. Therefore, this study is a first step toward the development of a PTX

formulation containing high PTX concentrations within well-defined, degradable nanoparticles for the treatment of lung metastasis of osteosarcoma and other cancers that occur in the lung.

PTX, a mitotic inhibitor originally isolated from the bark of the Pacific yew *Taxus brevifolia*, is a potent chemotherapeutic agent for the treatment of a variety of cancers, including ovarian, breast and lung cancers.[135,136] Due to its poor solubility in aqueous solutions, PTX is currently formulated with 1:1 blend of Cremophor EL (polyoxyethylated castor oil) and ethanol, under the trademark of Taxol®.[137] However, the intrinsic toxicity of Cremophor EL has caused serious side effects, such as hypersensitivity reactions, nephrotoxicity, neurotoxicity and myelosuppression.[135,138-140] To avoid these side effects, alternative formulations[141-143] are under development to improve PTX water solubility and biocompatibility, including Cremophor-free, albumin-bound PTX (Abraxane®, PTX water solubility 5 mg/mL) as a protein-drug suspension.[141,144-146] By taking advantage of the natural tumor uptake of nanosized albumin in the human body, Abraxane® has demonstrated increased antitumor activity and reduced toxicity, relative to Taxol®.[141,144] Although the packaging of PTX within a prevalent natural protein is an attractive strategy, there are questions as to how to achieve high drug loading without alteration of the protein while maintaining control over protein assembly.[141] Alternatively, synthetic nanoparticles have the potential for greater control over their compositions, structures and properties, while also allowing for selective domains into which the drug molecules can be packaged.[16]

Recently, an increasing number of polymeric nanoscopic platforms, including polymeric micelles,[142,147] dendrimers,[148] nanogels,[149] brush polymers,[150,151] and liposomes,[95,96,152] have been developed for the delivery of PTX and other chemotherapeutics.[153-155] In particular, polymeric micelles have been rigorously investigated due to their characteristic core-shell morphology, where hydrophobic cores are utilized for incorporation of hydrophobic drugs (herein PTX) while the hydrophilic shells provide water solubility and prolonged systemic circulation.[16,31,36] For example, NK105, is a micellar nanoparticle formulation currently in clinical trials, where PTX is incorporated in the core of polymeric micelles constructed from an amphiphilic block copolymer comprised of poly(ethylene glycol) (PEG) and polyaspartate segments.[142,156] By utilizing the enhanced permeability and retention (EPR) effect, NK105 demonstrated improved efficacy with reduced toxicity.[30,156,157] However, dissociation of polymeric micelles upon administration *in vivo* may cause premature release of therapeutics with loss in the control of delivery.[16,158-160]

To overcome micellar dissociation, shell crosslinking is of significant importance to enhance structural stability, as well as to mediate stimuli-responsive drug release.[16,41] We have previously demonstrated that shell crosslinked knedel-like nanoparticles (SCKs) display improved structural stability while retaining the tunability of size, shape and surface properties.[16,161,162] Recently, we have demonstrated that PTX could be loaded into the hydrophobic cores of SCKs, increasing the water solubility of PTX while maintaining comparable cytotoxicities to free PTX against several cancer cell lines.[50] However, these initial nanotherapeutics suffered from relatively low drug loading

percentages and their solubility limits led to fairly low overall PTX concentrations (< 30 μg/mL), making them undesirable for clinical applications. To improve upon these systems, we aimed to design biocompatible and fully degradable drug delivery carriers capable of effective incorporation of PTX at high concentrations in water. Such systems are of high interest due to their increased potential to effectively deliver chemotherapeutics and to be cleared from biological systems *via* intrinsically built-in degradation pathways.[52]

Polyphosphoesters have been receiving attention due to their biocompatibility, biodegradability and structural similarity to naturally-occurring biomacromolecules, such as DNA and RNA.[52,69,72-74] Since the phosphorous atom is pentavalent, reactive pendant groups, including hydroxyl, carboxyl, and alkynyl, may be introduced as side chain functionalities, allowing polyphosphoesters to be structurally versatile.[52,61,62] Recently, our lab developed a hydrophobic-functional AB diblock copolymer *via* rapid sequential organocatalyzed ring-opening polymerizations of hydrophobic alkyl- and reactive alkynyl-functionalized cyclic phosphotriesters monomers in a stepwise one-pot manner.[61] By taking advantage of radical-mediated thiol-yne reactions on the clickable alkynyl groups of the B block, this diblock copolymer could be transformed into a variety of amphiphilic block copolymers and assembled into functional nanoparticles tailored for biomedical applications.[61] In this study, we made use of this structurally-versatile platform to develop a drug carrier *via* copper(I)-catalyzed azide-alkyne cycloaddition (CuAAC) for transformation to an amphiphilic labeled polymer, capable of supramolecular assembly into PTX-loaded nanoparticles. Our results demonstrate

that these new nanotherapeutic delivery vehicles show potential towards future sustained release treatments *via* administration directly to the site of lung metastasis of osteosarcoma, whereby shell crosslinking reduced the rate of drug release and increased the lung retention time

3.2 Materials and methods

3.2.1. Materials

Paclitaxel was purchased from Alfa Aesar, Co. (Ward Hill, MA). 2-chloro-2-oxo-1,3,2-dioxaphospholane (95%) was used as received from Thermo Fisher Scientific Inc (Pittsburgh, PA). Chelex® 100 resin was used as received from Bio-Rad Laboratories (Hercules, CA). Tetrahydrofuran (THF) and dichloromethane (DCM) were dried through solvent purification system (J. C. Meyer Solvent Systems, Inc., Laguna Beach, CA). α-Methoxy-ω-azido PEG_{2k} (M_n = 1,950 kDa, M_w/M_n = 1.03) was purchased from RAPP POLYMERE (Tuebingen, Germany). IRDye® 800CW near infrared dye (IR800CW) was purchased from LI-COR® Biosciences (Lincoln, NE). All other chemicals were purchased from Sigma-Aldrich (St. Louis, MO) and used without further purification unless otherwise noted. Slide-A-Lyzer dialysis cassettes (10 kDa molecular weight cut-off, MWCO) were purchased from Pierce Biotech. (Rockford, IL). The Spectra/Por dialysis membranes (MWCO 12-14 kDa) were purchased from Spectrum Laboratories, Inc. (Rancho Dominguez, CA). Nanopure water (18 MΩ·cm) was acquired by means of a Milli-Q water filtration system, Millipore Corp. (Bedford, MA). CCH-OS-O and SJSA cell lines were obtained from the laboratory of Dr. Dennis Hughes, The University of Texas MD Anderson Cancer Center, Houston, TX. RAW

264.7 and OVCAR-3 cell lines, as well as RPMI and DMEM media were obtained from the American Type Culture Collection (Manassas, VA). Media additives (fetal bovine serum, penicillin/streptomycin) were obtained from Sigma-Aldrich (St. Louis, MO). Cell culture 96-well round bottom plates were purchased from Corning Costar Co. (Corning, NY). The CellTiter 96 non-radioactive cell proliferation assay was obtained from Promega Co. (Madison, WI).

3.2.2 Instrumentation

^{1}H NMR and ^{13}C NMR spectra were recorded on a Varian Inova 300 or Mercury 300 spectrometer interfaced to a UNIX computer using VnmrJ software. Chemical shifts were referenced to the solvent residual signals. FTIR spectra were recorded on an IR Prestige 21 system using a diamond ATR lens (Shimadzu Corp., Japan) and analyzed using IRsolution v. 1.40 software. The DMF gel permeation chromatography (GPC) was conducted on a Waters Chromatography, Inc. (Milford, MA) system equipped with an isocratic pump model 1515, a differential refractometer model 2414, and a three-column set of Styragel HR 4 5 μm DMF (300 × 7.5 mm), Styragel HR 4E 5 μm DMF (300 × 7.5 mm), and Styragel HR 2 5 μm DMF (300 × 7.5 mm). The system was equilibrated at 70 °C in pre-filtered DMF containing 0.05 M LiBr, which served as polymer solvent and eluent (flow rate set to 1.00 mL/min). Polymer solutions were prepared at a concentration of *ca*. 3 mg/mL and an injection volume of 200 μL was used. Data collection and analysis were performed with Empower 2 v. 6.10.01.00 software (Waters, Inc.). The system was calibrated with polystyrene standards (Polymer Laboratories, Amherst, MA) ranging from 615 to 442,800 Da.

All steady-state emission, excitation, and anisotropy spectra were obtained with a Horiba FluoroMax4 with automatic polarizers. Steady-state spectra were analyzed in FluorEssence (Horiba, Kyoto, Japan) and in Origin 9.0 Pro (Origin Lab, Northampton, MA). Time-correlated single-photon counting (TCSPC) was employed to obtain all fluorescence lifetime and fluorescence anisotropy decay spectra. Measurements were achieved *via* a Fluorotime 100 fluorometer with a 640 nm solid-state picoseconds diode laser source (PicoQuant, West Springfield, MA) in matched quartz 0.7 mL cells (NSGPrecision Cells, Farmingdale, NY). Instrument response functions (IRF) were determined from the scattering signal with a solution of Ludox HS-40 colloidal silica (0.01% w/w particles in water). TCSPC analysis was performed on Fluorofit (PicoQuant) software and confirmed by tail-fitting in Origin 9 Pro. All fluorescence confocal microscopy was carried out on a FV1000 confocal microscope with an IX-81 inverted base (Olympus, Center Valley, PA) and PMT detectors.

Dynamic light scattering (DLS) measurements were conducted using a Delsa Nano C (Beckman Coulter, Fullerton, CA) instrument equipped with a laser diode operating at 658 nm. Size measurements were made in nanopure water (n = 1.3329, η = 0.890 cP at 25 ± 1 °C). Scattered light was detected at a 165° angle and analyzed using a log correlator over 70 accumulations for a 3.0 mL sample in a glass sizing cell (4.0 mL capacity). The photomultiplier aperture and the attenuator were automatically adjusted to obtain a photon counting rate of *ca*. 10 kcps. Calculations of the particle size distribution and distribution averages were performed using CONTIN particle size distribution analysis routines. The peak averages of histograms from number

distributions out of 70 accumulations were reported as the average diameters of the particles. The particle zeta-potential values were determined by a Delsa Nano C particle analyzer equipped with a 30 mW dual laser diode (658 nm). The ζ-potential of the particles in suspension was obtained by measuring the electrophoretic movement of charged particles under an applied electric field. Scattered light was detected at a 15° angle at 25 °C. The zeta-potential was measured at five regions in the flow cell, and a weighted mean was calculated. These five measurements were used to correct for electro-osmotic flow that was induced in the cell due to the surface charge of the cell wall. All determinations were repeated five times.

Glass transition temperatures (T_g) were measured by differential scanning calorimetry on a Mettler-Toledo DSC822® (Mettler-Toledo, Inc., Columbus, OH), with a heating rate of 10 °C/min. Measurements were analyzed using Mettler-Toledo Star^e v. 7.01 software. The T_g was taken as the midpoint of the inflection tangent, upon the third heating scan. Thermogravimetric analysis was performed under N_2 atmosphere using a Mettler-Toledo model TGA/SDTA851^e, with a heating rate of 10 °C/min. Measurements were analyzed by using Mettler-Toledo Star^e v. 7.01 software.

Transmission electron microscopy (TEM) images were collected on a JEOL 1200EX operating at 100 kV and micrographs were recorded at calibrated magnifications using a SIA-15C CCD camera. The samples as aqueous solutions (4 μL) were deposited onto carbon-coated copper grids, and after 1 min, the excess of the solution was quickly wicked away by a piece of filter paper. A drop of 1 *wt*% uranyl acetate was then added, and allowed to stand for 30 seconds before excess stain was wicked away. The grids

were allowed to dry in air overnight. Cryo-TEM images were taken with an FEI Tecnai G2 F20 (FEI, Hillsboro, OR) operated at 200 kV and equipped with cryogenic accessories. Specimens were prepared on CFLAT holey carbon film TEM grids which were pretreated with glow discharge plasma for 30 s to improve the wetting of the hydrophobic grids. The samples were frozen in liquid ethane using an FEI Vitrobot apparatus and submerged in liquid nitrogen, where it was kept until imaging.

3.2.3. Experimental procedures

Synthesis of EBP and BYP monomers. 2-(but-3-yn-1-yloxy)-2-oxo-1,3,2-dioxaphospholane (BYP) and 2-(2-ethylbutoxy)-1,3,2-dioxaphospholane (EBP) were synthesized as previously described.[61]

Synthesis of PEBP-*b*-PBYP diblock copolymer. A solution of EBP (1.5 g, 7.2 mmol) and benzyl alcohol (15.6 mg, 0.14 mmol) in 2.1 mL anhydrous dichloromethane was transferred *via* syringe into a flame-dried vial equipped with a stir bar and rubber septum, under N_2, in an water/ice bath. A solution of 1,5,7-triazabicyclo[4.4.0]dec-5-ene (TBD) (40.2 mg, 0.29 mmol) in 0.3 mL anhydrous dichloromethane was injected quickly into the vial. After being stirred for 2.5 min, another 2.4 mL of anhydrous dichloromethane was injected into the vial to dilute the reaction mixture, and the vial was transferred to a cooling bath composed of equal amounts of ice/water and sodium chloride at -10 °C. Less than 0.1 mL of the reaction mixture was withdrawn and diluted with $CDCl_3$ to determine the EBP conversion by ^{31}P NMR. After being stirred for another 3 min, to the reaction mixture was added a solution of BYP (1.27 g, 7.2 mmol) in 2.4 mL anhydrous dichloromethane *via* syringe. The reaction was quenched by

adding an excess amount of acetic acid dissolved in DCM after another 3 min, and an aliquot of the mixture was used to determine the conversion of BYP by ^{31}P NMR. The PEBP-*b*-PBYP was purified by precipitation from acetone into a pentane/diethyl ether mixture (3:1 volume ratio) three times and then dried under vacuum. ^{1}H NMR (300 MHz, $CDCl_3$, ppm): δ 0.90 (t, *J* = 7.4 Hz, $POCH_2CH(CH_2CH_3)_2$), 1.37 (m, $POCH_2CH(CH_2CH_3)_2$), 1.51 (m, $POCH_2CH$), 2.11 (s, $POCH_2CH_2CCH$), 2.61 (m, $POCH_2CH_2CCH$), 4.00 (m, $POCH_2CH$), 4.12–4.39 (m, $POCH_2CH_2OP$, $POCH_2CH_2$), 5.08 (d, *J* = 8.3 Hz OC*H2*Ar), 7.31–7.40 (m, Ar-*H*); ^{13}C NMR (75 MHz, $CDCl_3$, ppm): δ 10.99, 20.69, 22.75, 41.55, 65.52-67.11, 70.08, 70.88, 79.59; ^{31}P NMR (121 MHz, $CDCl_3$, ppm): δ -1.25, -1.81. GPC: M_n = 18900 g/mol, PDI = 1.24. DSC: T_g = - 58 °C. TGA in N_2: 170–270 °C, 50% mass loss; 270–360 °C, 9.2% mass loss, 360–600 °C, 11% mass loss, 30 % mass remaining above 600 °C. IR (cm^{-1}): 3700-3100, 3020-2820, 1640, 1460, 1380, 1267, 1010, 965, 866, 805.

Azide-alkyne Huisgen cycloaddition of PEBP-*b*-PBYP with α-methoxy-ω-azido PEG (CH_3O-PEG_{2k}-azido). In a typical experiment, an oven dried vial containing a magnetic stir bar was charged with PEBP-*b*-PBYP (0.89 g, 46 μmol, 1 eq.), α-methoxy-ω-azido PEG (0.36 g, 180 μmol, 4 eq.), *N*,*N*,*N*′,*N*′,*N*″-pentamethyldiethylenetriamine (PMDETA, 13 mg, 74 μmol, 1.6 eq.) and 7 mL of DMF. The reaction mixture was degassed by several freeze-pump-thaw cycles (N>3), during which copper(I) bromide (5.3 mg, 37 μmol, 0.8 eq.) was added. The flask was allowed to return to room temperature after the final cycle and stirred for another 3 h under N_2. The solution was subsequently filtered through a neutral alumina column and dialyzed against Chelex®

100 resin in nanopure water in presoaked dialysis tubing (MWCO *ca*. 12–14 kDa) for 2 d to remove copper ions, followed by lyophilization to yield a white powder with a 72 % yield. Inductively coupled plasma-mass spectrometry (ICP-MS) confirmed that *ca.* 10 ppm of copper was present in the polymer. ^{1}H NMR (300 Hz, $CDCl_3$, ppm): δ 0.89 (t, *J* = 7.4 Hz, $POCH_2CH(CH_2CH_3)_2$), 1.36 (m, $POCH_2CH(CH_2CH_3)_2$), 1.50 (m, $POCH_2CH$), 2.05-2.24 (b, $POCH_2CH_2CCH$), 2.56-2.65 (b, $POCH_2CH_2CCH$), 3.12 (m, NCH_2CH_2), 3.37 (s, OCH_3), 3.63 (s, OCH_2CH_2), 4.00 (m, $POCH_2CH$), 4.14-4.39 (m, POCH2CH2, POCH2CH2OP), 5.07 (d, *J* = 8.3 Hz, OCH_2Ar), 7.31-7.40 (m, Ar-*H*), 7.63 (m, $CH_2CH_2CCHNCH_2$). ^{13}C NMR (75 MHz, $CDCl_3$, ppm): δ 11.03, 20.72, 22.79, 41.60, 65.52-67.15, 70.13, 70.68, 70.95, 79.72, 128.06, 128.73. ^{31}P NMR (121 MHz, $CDCl_3$, ppm): δ -0.99, -1.64. GPC: M_n = 21800 g/mol, PDI = 1.24. DSC: T_g = - 51 °C; T_m = 46 °C. TGA in N_2: 140–270 °C, 40% mass loss; 270–360 °C, 35% mass loss, 360–600 °C, 3% mass loss, 22 % mass remaining above 600 °C. IR (cm^{-1}): 3700-3100, 3050-2800, 166, 1465, 1342, 1275, 1109, 1016, 962, 841, 808.

Determination of critical micelle concentrations (CMCs) for PEBP-*b*-PBYP-*g*-PEG. The CMC for the terpolymers PEBP-*b*-PBYP-*g*-PEG in nanopure water was determined by using pyrene as the fluorescent probe. The sample solutions were prepared by adding 75 μL pyrene aqueous stock solution (6.0×10^{-7} mol/L) and from 0.25 to 0.001 mg of polymer from an aqueous 1 mg/mL stock solution into a 5 mL vial, and the final volumes were adjusted to 1.0 mL by addition of nanopure water. All the sample solutions were then stirred at 4 °C for 24 h to allow for equilibration of pyrene into the micelles. The fluorescence measurements were conducted at room temperature,

pyrene was excited at 334 nm and its emission spectrum was recorded from 360 to 460 nm. The experiment was repeated three times and the ratios of intensities at 369 and 382 nm, corresponding to the first and third pyrene vibrational peaks respectively, were plotted against the polymer concentrations in the sample solutions. The CMC was taken as the intersection of the tangent to the curve at the inflection with tangent through the points at low polymer concentration. The CMC of the amphiphilic terpolymer was measured to be 0.018 ± 0.009 mg/mL.

Preparation of shell crosslinked (SCK) nanoparticles from PEBP-*b*-PBYP-*g*-PEG. In a typical experiment, 30.0 mg PEBP-*b*-PBYP-*g*-PEG was dissolved in 15.0 mL methanol in a 100 mL flask and allowed to stir for 30 min at room temperature. To this solution, 15.0 mL nanopure water was added dropwise *via* a syringe pump over a period of 4 min. The mixture was allowed to stir another 30 min at room temperature and bubbled with nitrogen. To the micelle solution was added a solution of hexa(ethylene glycol) dithiol (3.5 mg, 0.2 eq., with respect to alkyne, nominally 20% crosslinking) in 1:1 methanol/nanopure water mixture, 2,2-dimethoxy-2-phenylacetophenone in methanol (DMPA, 2.9 mg, 0.2 eq., with respect to alkyne residues). The resulting mixture was placed under an UV lamp and irradiated at 365 nm for 3 h, dialyzed against nanopure water for 2 d in presoaked dialysis tubing (MWCO *ca*. 12–14 kDa), and then lyophilized to yield a yellowish powder with a 87% yield. Hydrodynamic diameters of SCKs in nanopure water as measured by DLS: $D_{h(intensity)}$ = 407 ± 475 nm, $D_{h(volume)}$ = 19 ± 11 nm, $D_{h(number)}$ = 14 ± 3 nm; ζ-potential in nanopure water: - 34 ± 2 mV; Diameter as measured by TEM: 23 ± 3 nm.

NIR-labeling of micelles and SCKs. In a typical experiment, an oven-dried vial containing a magnetic stir bar was charged with micelles or SCKs (PEBP-*b*-PBYP-*g*-PEG, 88 mg, 3.2 μmol, 1 eq.), IR800CW (2.1 mg from a 1 mg/mL stock solution in DMSO, 1.6 μmol, 0.5 eq.), copper(II) sulfate pentahydrate (0.8 mg, 3.2 μmol, 1 eq.), sodium ascorbate (6.4 mg, 32 μmol, 10 eq.) and 9.0 mL nanopure water. The reaction mixture was degassed for 10 min *via* nitrogen bubbling, wrapped with aluminum foil and stirred for another 24 h at 37 °C. The solution was subsequently passed through a Sephadex G-25 desalting column and dialyzed against Chelex® 100 resin in nanopure water in presoaked dialysis tubing (MWCO *ca*. 12–14 kDa) for 2 d, to remove copper ions and unreacted IR800CW, followed by lyophilization to yield green powder.

Dye-labeled micelles: 91% yield with a conjugation efficiency of 64%. Hydrodynamic diameters of micelles in nanopure water as measured by DLS: $D_{h(intensity)}$ = 36 ± 23 nm, $D_{h(volume)}$ = 16 ± 8 nm, $D_{h(number)}$ = 11 ± 3 nm; ζ-potential in nanopure water: - 36 ± 1 mV; Diameter as measured by TEM: 36 ± 4 nm.

Dye-labeled SCKs: 90% yield with a conjugation efficiency of 63%. Hydrodynamic diameters of micelles in nanopure water as measured by DLS: $D_{h(intensity)}$ = 129 ± 155 nm, $D_{h(volume)}$ = 16 ± 10 nm, $D_{h(number)}$ = 11 ± 3 nm; ζ-potential in nanopure water: - 36 ± 1 mV; Diameter as measured by TEM: 24 ± 4 nm.

PTX loading into PEBP-*b*-PBYP-*g*-PEG micelles and SCKs. In a typical experiment, to a vial containing 4.5 mL of polymer or SCK solution in ethanol (polymer or SCK concentration: 4.0 mg/mL), PTX at 2.0 mg/mL in ethanol, 10 *wt%* was added. The vial was shaken vigorously to mix the solution, and then ethanol was completely

removed *in vacuo*. Subsequently, the micelles/SCKs with PTX were resuspended in 2.0 mL of nanopure water. After sonication for 5 min, a well dispersed nanoparticle suspension was obtained. DLS and TEM were used to characterize these PTX-loaded nanoparticles, and HPLC was used to confirm the actual loading amount of PTX.

PTX-loaded micelles: hydrodynamic diameters in nanopure water as measured by DLS: $D_{h(intensity)}$ = 38 ± 20 nm, $D_{h(volume)}$ = 19 ± 9 nm, $D_{h(number)}$ = 14 ± 4 nm; ζ-potential in nanopure water: - 39 ± 4 mV; Diameter as measured by TEM: 42 ± 5 nm

PTX-loaded SCKs: hydrodynamic diameters in nanopure water as measured by DLS: $D_{h(intensity)}$ = 70 ± 43 nm, $D_{h(volume)}$ = 32 ± 15 nm, $D_{h(number)}$ = 24 ± 6 nm; ζ-potential in nanopure water: - 43 ± 2 mV; Diameter as measured by TEM: 24 ± 4 nm

PTX-loaded dye-labeled micelles: hydrodynamic diameters in nanopure water as measured by DLS: $D_{h(intensity)}$ = 70 ± 55 nm, $D_{h(volume)}$ = 21 ± 12 nm, $D_{h(number)}$ = 14 ± 4 nm; ζ-potential in nanopure water: - 45 ± 5 mV; Diameter as measured by TEM: 38 ± 4 nm

PTX-loaded dye-labeled SCKs: hydrodynamic diameters in nanopure water as measured by DLS: $D_{h(intensity)}$ = 77 ± 59 nm, $D_{h(volume)}$ = 23 ± 13 nm, $D_{h(number)}$ = 16 ± 5 nm; ζ-potential in nanopure water: - 24 ± 3 mV; Diameter as measured by TEM: 25 ± 3 nm

Release of PTX from PTX-loaded micelles and SCKs. The release profiles of the PTX-loaded micelles and SCKs were studied by monitoring the decrease of PTX concentration over time in dialysis cassettes by high-performance liquid chromatography (HPLC) using a UV detector at 228 nm. In a typical procedure, PTX-loaded

nanoparticles were diluted with phosphate buffered saline (PBS), yielding a concentration of 50 μg/mL. A portion of the PTX-loaded micelles or SCKs solution (3.0 mL) was transferred into a presoaked dialysis cassette (Slide-A-Lyzer, 10 kDa MWCO, Pierce Biotechnology, Rockford IL). The cassette was allowed to stir in a beaker containing 3000 mL PBS (pH 7.4 at 37 °C). Aliquots (0.1 mL) were taken at pre-determined times and analyzed by HPLC. The release was evaluated in triplicate.

Sample preparation for steady-state anisotropy and fluorescence lifetime. (1)IRDye 800CW azide was dissolved in DMSO at a concentration of 1.0 mg/mL and diluted with water or PBS to achieve a final concentration of *ca.* 1.3 μg/mL with an absorption of *ca.* 0.25. (2)IRDye 800CW labeled micelles or SCKs were dissolved at a concentration of 9.8 mg/mL in water and diluted with water or PBS to achieve a final concentration of *ca.* 320 μg/mL with an absorption of *ca.* 0.25. (3)Physical mixtures were prepared by mixing IRDye 800CW azide and micelle or SCKs at the same ratio as dye conjugates and diluted with water or PBS to achieve a final concentration of *ca.* 320 μg/mL polymer concentration with an absorption of *ca.*0.25.

Cytotoxicity assays. Human ovarian adenocarcinoma cells (OVCAR-3) (5×10^3 cells/well), RAW 264.7 mouse macrophages (2×10^4 cells/well), CCH-OS-O (5×10^3 cells/well) and SJSA (5×10^3 cells/well) were plated in 96-well plates in RPMI-1640 medium (OVCAR-3) and Dulbecco's Modified Eagle's Medium (DMEM) (20% fetal bovine serum for the OVCAR-3, 10% fetal bovine serum for RAW 264.7, CCH-OS-O and SJSA, and 1% penicillin/streptomycin). Cells were incubated at 37 °C in a humidified atmosphere containing 5% CO_2. The medium was replaced with fresh

medium 24 h after seeding. Formulations of PTX-loaded micelles and SCKs dissolved in PBS were prepared at concentrations that ranged from 1.0×10^{-4} to 6.6 μM. For each well, 20 μL of every formulation was added to 100 μL of the medium. Negative controls were created by addition of 20 μL of PBS to wells containing cells and 100 μL of the medium. The cells were incubated for 72 h, and after this period, the medium was replaced with 100 μL of the fresh medium. Then, 20 μL of the MTS combined reagent was added to each well (Cell Titer 96® Aqueous Non-Radioactive Cell Proliferation Assay, Promega Co., Madison, WI). The cells were incubated with the reagent for 3 h at 37 °C in a humidified atmosphere containing 5% CO_2, and protected from light. Absorbance was measured at 490 nm using SpectraMax M5 (Molecular Devices Co., Sunnyvale, CA). The cell viability was calculated based on the relative absorbance to the control untreated cells. The calculation of the IC_{50} values and the statistical analysis were performed using GraphPad Prism four-parameter fit, the 0% and 100% viabilities are for media control (no cells) and cells with no treatment, respectively.

Preparation of cells for confocal microscopy. CCH-OS-O cells were trypsinized and counted with a hemocytometer. The cell pellet was dissolved in phosphate buffered solution (PBS pH = 7.0) to a final concentration of $2x10^5$ cells/mL. To a glass bottom 6-well plate (No.0 Uncoated y-irradiated, MatTek Corporation) 0.5 mL of the cell solution was added to each well by placing 0.1 mL spots in a star pattern around the glass surface of the well to promote localization of cells. Dulbecco's Modfied Eagle Medium (DMEM) supplemented with 10% fetal bovine serum (FBS) was added to each well to

achieve a final volume of 2.0 mL. Plates were incubated for 24 h in a humidified atmosphere with 5% CO_2

Preparation of polymer solutions for cellular uptake. Lyophilized micelles and SCKs physically loaded with PTX were dissolved in PBS (pH = 7.0) to a final concentration of 9.8 mg/mL of polymer (33 μM IR800CW dye, 1270 μM PTX). IR800CW labeled micelles and SCKs without PTX were prepared under the same conditions to a concentration of 9.8 mg/mL of polymer.

Addition of formulations to measure cellular uptake. One of the formulations described above (micelles or SCKs) was added to each well by removing 500 μL of the well's media, and mixing 400 μL of media with 100 μL of the prepared formulations. The resulting mixture was then added back to the well so that the total volume of media did not change. The final concentration of polymer, IR800CW and PTX were *ca.* 2 mg/mL, 20 μM and 254 μM respectively. Formulations were added 2 h prior to imaging. After 1.5 h, Hoechst 33345 was added to each well to stain the nucleus (1ug/mL, Life Technologies) and incubated for 15 min. The wells were washed twice with Opti-MEM medium (Gibco) and imaged live.

Confocal microscopy of live CCH-OS-O cells for measuring cellular uptake. A FV1000 confocal microscope with an IX-81 inverted base and PMT detectors was used for all confocal microscopy. For excitation of the Hoechst-33342 nuclear stain, a 405 nm diode laser was used, and emission was collected from 420-450 nm. The NIR dye IR800CW (conjugated to the nanomaterials) was excited using a 635 nm solid-state laser, and emission was collected using a 775 nm long pass filter. To confirm for the

lack of autofluorescence, samples of cells lacking nuclear stain and without polymer were imaged as a control. Preliminary studies of unlabeled polymers also showed lack of autofluorescence. A 20x UPlanSApo lens (na 0.75 infinity corrected) was used for all measurements. The zoom function of the microscope was used to reach a total magnification of 60x to 100x for all images. Each final image was taken at a scan rate of 40 μs/pixel at 1025 by 1025 pixels. Images were acquired and contrast was adjusted using Fluoview Viewer software V. 3.1.2.2 (Olympus, Center Valley, PA).

***In vivo* studies**. All animal studies were conducted in accordance to protocols approved by the Texas A&M University Institutional Animal Care and Use Committee.

In vivo imaging studies were carried out on a Bruker In-Vivo Xtreme multimodal preclinical imaging system (Bruker BoiSpin Corp., Billerica, MA) outfitted with a back-thinned, back-illuminated 4MP CCD detector and Bruker hard coated emission filters. *In vivo* images were acquired *via* a pre-established 3 step imaging protocol acquiring sequential X-ray, fluorescence and reflectance images. X-rays were collected with a standard 0.4 mm aluminum x-ray filter and an exposure time of 20 s using an X-ray energy of 35 KVP (f-stop = 2.80, FOV = 100 mm, vertical and horizontal resolution = 520 ppi). Fluorescence images were collected at ex 760 nm and em 830 nm with a 20 s exposure (binning = 4×4, f-stop = 1.10, FOV = 100 mm, vertical and horizontal resolution = 130 ppi). The background was subtracted automatically using an illumination correction reference obtained under the same conditions. Reflectance images were obtained using a standard 3 second exposure and the same parameters as

per the X-ray image. All Images were evaluated using Bruker molecular imaging software.

Intratracheal (IT) administration of NIR contrast agents and *in vivo* imaging. Mice were anesthetized by Ketamine/Xylazine cocktail at 87 mg/kg and 13 mg/kg respectively, whereby each mouse is given 0.1 cc/10 g body weight IP, and imaged. Mice were then intubated orally with a 20 gauge flexible catheter by direct visualization of the vocal chords. Assurance of successful intubation was assessed visually and by monitoring breathing sounds. Following successful intubation IT injection was carried out by attaching a pre-loaded syringe to the catheter, such that 50 μL of the appropriate solution (33 μM free NIR Dye or micelles or SCKS containing 33 μM IR800CW in sterile water (approximately 0.5 mg of polymer) was administered. Mice were extubated, upon re-establishment of normal breathing *in vivo* imaging was carried out at t = 0, 2, 6, 12 & 24 h, and then daily for 7 – 14 days. For imaging post-injection (PI) mice were lightly anesthetized by administration of Isoflurane (1.5 – 2% v/v in 100% oxygen), using a precision vaporizer, *via* chamber or nose cone. Analysis of all *in vivo* images was carried out using Bruker Molecular Imaging Software.

***Ex vivo* biodistribution analysis**. At all study end points animals were euthanized by CO_2 asphyxiation and relevant organs were plated for fluorescence imaging (liver, kidney, spleen, skin, muscle, heart, lung, blood and brain). *Ex vivo* images were then obtained using a pre-established 2-step imaging protocol acquiring sequential X-ray and fluorescence images. X-rays were collected with a standard 0.2 mm aluminum x-ray filter and an exposure time of 3.5 s using an X-ray energy of 30 KVP (f-stop = 2.00,

FOV = 175 mm, vertical and horizontal resolution = 300 ppi). Fluorescence images were collected at λ_{ex} = 760 nm and λ_{em} = 830 nm with an 8 s exposure (binning = 4×4, f-stop = 2.00, FOV = 175 mm, vertical and horizontal resolution = 75 ppi). The background was subtracted automatically using an illumination correction reference obtained under the same conditions. All Images were evaluated using Bruker molecular imaging software. To quantify the fluorescence intensity for each organ a rectangular region of interest (ROI) was created surrounding the organ. For each ROI the net intensity minus the background was determined by the Molecular Imaging software, along with the area (cm^2) of the ROI. The net intensity was normalized by both organ weight (g) and ROI area. The standard deviation was calculated for each organ based upon a population of n = 3.

Pharmacokinetic (PK) calculations. Analysis of all *in vivo* images was carried out using Bruker Molecular Imaging Software. A ROI was created utilizing 1 mouse over the entire lung region, and saved as a template. This template was then applied to images of each mouse obtained pre-injection and at 0, 3, 6, 12 and 24 h PI, and then daily for up to 14 days. For each ROI the location was adjusted to cover the entire lung region of the animal, but the total area was not changed. For each time point, for each mouse, the mean intensity minus the background was determined by the Molecular Imaging software and the pre-injection mean intensity was subtracted such that the intensity before injection of the contrast agent equals zero. The fluorescence intensities were then normalized from 0 – 100 creating the PK profile for each material (IR800CW Azide, Micelles and SCKs). Utilizing Origin 9.1 the rate of extravasation and half-life

of each material was determined by obtaining a non-linear curve fit of the appropriate PK profile. The standard deviation, at each time point, and for each material, was calculated based upon a population of n = 3.

***Ex vivo* tissue collection for confocal imaging**. At all study end points animals were euthanized by CO_2 asphyxiation. For cryosectioning the lungs were filled with a 50/50 solution of sterile water and optimum cutting temperature compound (OCT) utilizing a 20 gauge syringe bent at a 45º angle. All tissues were provided to the Veterinary Integrative Biosciences (VIBS) histology lab, sectioned to a thickness of 20 μm with a cryostat and stored on plus coated slides (Mercedes Medical, Sarasota, FL) at -80 C. Before confocal fluorescence imaging slides were warmed to room temperature, 1 drop of VECTASHIELD® mounting media containing DAPI (Vector Laboratories, Berlingame, CA) was applied and the tissue was covered with #1 cover glass. Confocal images were acquired on a FV1000 confocal microscope with an IX-81 inverted base and PMT detectors was used for all confocal microscopy. The DAPI nuclear stain was excited with a 405 nm diode laser, and emission was collected from 420-450 nm. The NIR dye IT800CW (conjugated to the nanomaterials) was excited using a 635 nm solid-state laser, and a 775 nm long-pass emission filter. Tissue from untreated mice were used as a control to confirm the lack of autofluorescence. A 10 or 20X UPlanSApo lens (na 0.75 infinity corrected) was used for all measurements. Each final image was taken at a scan rate of 12.5 or 20 μs/pixel at 1025 by 1025 pixels at a final magnification of 10 or 160x. Images were acquired and contrast was adjusted using Fluoview Viewer software V. 3.1.2.2.

3.3 Results and discussion

In order to construct high capacity and scalable polymer-based nanotherapeutics, we designed supramolecular and covalently-stabilized nanoparticles, formed from biocompatible, degradable and structurally-versatile amphiphilic block terpolymers that were prepared by efficient "click-type" chemistries, including rapid ring-opening polymerizations (ROPs) and azide-alkyne Huisgen cycloaddition reactions (Figure 3.1). The block copolymer consists of a degradable and water-soluble polyphosphoester backbone, for which the first block contains alkyl side chains for creating a hydrophobic

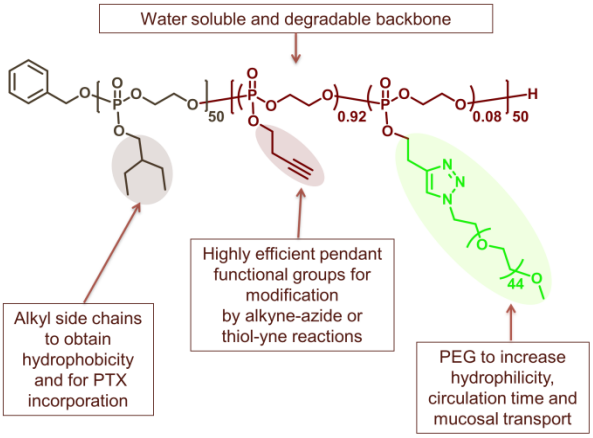

Figure 3.1. Design of the amphiphilic block terpolymer for therapeutic delivery.

environment and the second block is comprised of alkynyl side chains for post-polymerization modifications. The alkynes in the second block were used to graft PEG chains onto the block copolymer through CuAAC, to increase the polymer hydrophilicity, and also the conjugation of near infrared fluorescent dyes (IRDye®

800CW), to facilitate imaging *in vivo* and determination of particle pharmacokinetics (PK).

The amphiphilic nature of the resulting copolymers allowed for the formation of micelles in aqueous solution, which are capable of encapsulating PTX through hydrophobic interactions within the core. Crucial to biomedical applications is that PEG is a well-known and non- to minimally-toxic coating for nanoparticles that imparts "stealth" effects. PEGylation often results in minimal protein adsorption and mononuclear phagocyte system (MPS) clearance, and leads to prolonged blood circulation times and an increase in mucosal transport.[15,16,163-167] Mucosal transport, in particular, is key to the development of inhalation-based chemotherapeutics in the treatment of lung metastasis of osteosarcoma. Important for tailoring this platform is the presence of remaining unreacted alkynes, which were utilized for post-graft crosslinking and could be adapted for further modification.

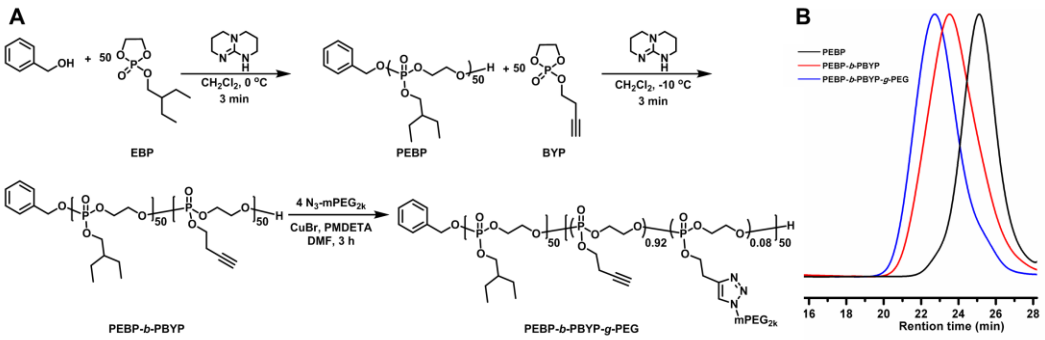

Figure 3.2. (A) Synthesis of PEBP-*b*-PBYP-*g*-PEG *via* sequential ring-opening polymerization of EBP and BYP, followed by PEGylation *via* CuAAC. (B) GPC traces of PEBP homo-polymer (black line), PEBP-*b*-PBYP diblock copolymer (red line) and PEBP-*b*-PBYP-*g*-PEG terpolymer (blue line).

The amphiphilic block terpolymer PEBP-*b*-PBYP-*g*-PEG was synthesized utilizing click-type chemistries, which are attractive as they occur rapidly, involve (near) quantitative conversions of reagents, high functional group tolerance and minimal side reactions (Figure 3.2A). A hydrophobic-functional AB diblock polyphosphoester was synthesized *via* sequential ROPs, a well-established approach to synthesize degradable polymers such as polyesters,[15,54,55] polypeptides,[56,57] polycarbonates,[58-60] and polyphosphoesters.[61-63] Briefly, the diblock copolymer poly(2-ethylbutoxy phospholane)-*block*-poly(2-butynyl phospholane) (PEBP-*b*-PBYP) was synthesized *via* sequential ROPs of 2-ethylbutoxy phospholane (EBP) and 2-butynyl phospholane (BYP), catalyzed by organocatalyst 1,5,7-triazabicyclo[4.4.0]dec-5-ene (TBD) at 0 °C and -10 °C, respectively, in dichloromethane, with benzyl alcohol as an initiator (Figure 3.2A). Phosphorus-31 nuclear magnetic resonance (^{31}P NMR) spectroscopy was used to monitor monomer conversion. It was found that over 99% conversion was reached after 3 min for the alkyl monomer, while the second alkyne monomer required less than 3 min to reach 99% conversion, even at lower monomer concentration and temperature. The reaction was quenched by the addition of acetic acid, and purified by precipitation from dichloromethane into pentane and diethyl ether (3:1) mixture, followed by centrifugation. Gel permeation chromatographic (GPC) analysis showed that both PEBP and PEBP-*b*-PBYP exhibited monomodal molecular weight distributions with relatively low polydispersity indices (PDIs) of 1.14 and 1.24, respectively (Figure 3.2B). The decreased retention time of PEBP-*b*-PBYP, relative to PEBP, demonstrated successful chain extension. PEGylation was achieved in *N*,*N*-dimethylformamide (DMF) *via*

CuAAC quantitatively for CH_3O-PEG_{2k}-azido-functionalized PEG grafts, as confirmed by proton NMR (^{1}H NMR) spectroscopy and GPC (Figure 3.2). To remove copper ions, the reaction mixture was passed through a neutral alumina column and dialyzed against nanopure water suspended with Chelex for 2 d in a cold room at *ca.* 4 °C. A white powder-like product was obtained after lyophilization. The residual copper concentration was analyzed by ICP-MS, revealing a mass fraction of less than 10 ppm, which is acceptable for drug delivery applications.

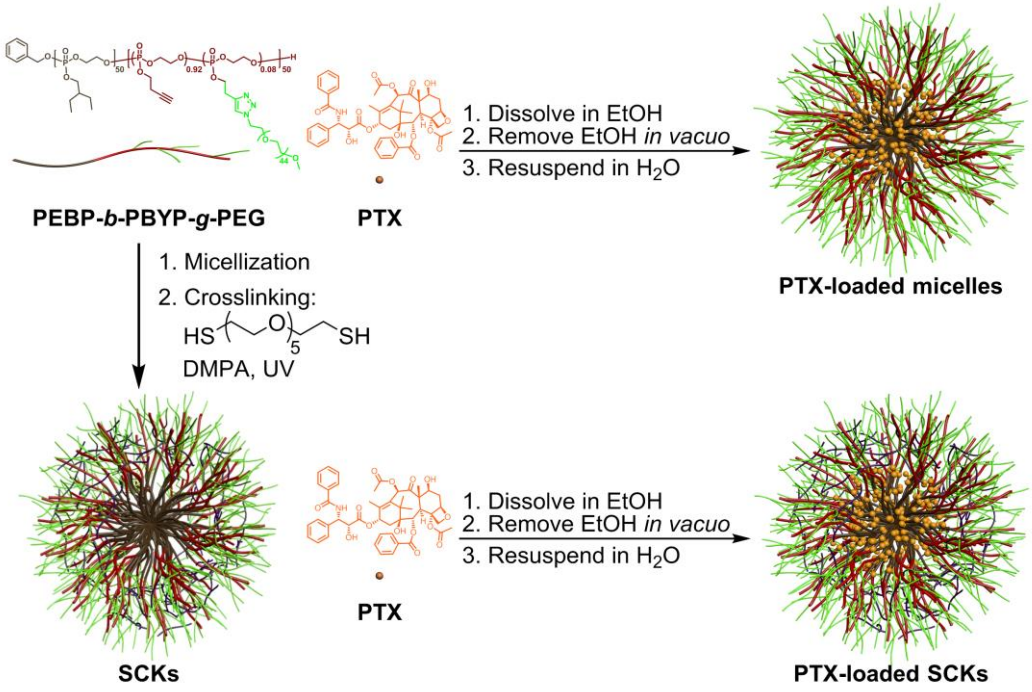

Figure 3.3. Schematic representation of the formation of micelles and SCKs physically loaded with PTX.

With an average of only four PEG grafts per polyphosphoester block terpolymer backbone, PEBP-*b*-PBYP-*g*-PEG was found to be highly water soluble and PTX-loaded

micelles and SCKs could be prepared in a facile manner (Figure 3.3). PTX-loaded micelles were formed by dissolving the polymer and PTX in ethanol, followed by the removal of ethanol *in vacuo* and resuspension in nanopure water, with 5 min sonication to allow for the formation of well-dispersed micelles.

The SCKs were prepared by supramolecular assembly of PEBP-*b*-PBYP-*g*-PEG into micelles, followed by shell crosslinking *via* thiol-yne click chemistry. The block graft terpolymer was first dissolved in methanol; subsequent addition of water directed the hydrophobic PEBP segments to aggregate and form the core domains of the micelles, while the hydrophilic PEG formed the shell domains. The formed micelles were then shell crosslinked with hexa(ethylene glycol) dithiol (0.2 equivalents to alkyne groups) in the presence of 2,2-dimethoxy-2-phenylacetophenone (DMPA) and UV irradiation at 365 nm. The resulting SCKs were dialyzed for 2 d to remove organic solvent and other small molecules and subsequently lyophilized to yield a yellowish powder. Upon dissolution in ethanol, the SCK suspension displayed strong light scattering when a laser light was passed through the solution indicating successful crosslinking, with a number-averaged diameter of *ca.* 33 nm as measured by dynamic light scattering (DLS) (Figure 3.4). PTX was loaded into SCKs utilizing the procedure for the PTX-loaded micelles, using SCKs in place of the polymer PEBP-*b*-PBYP-*g*-PEG (Figure 2). Importantly, long term storage (> 6 months) of lyophilized PTX-loaded micelles and SCKs did not affect their properties upon re-suspension in aqueous solution.

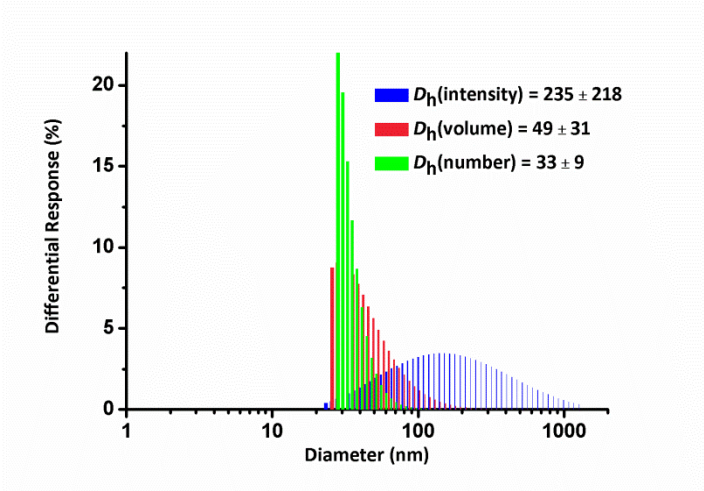

Figure 3.4. DLS histograms of D_h(intensity), D_h(volume),, D_h(number) hydrodynamic diameters of empty SCKs in ethanol.

The PTX concentration and loading capacity were optimized, for both the micelles and SCKs, by tuning PTX loading percentages and polymer or SCK concentrations (Table 3.1). The actual PTX concentrations were determined by HPLC at a flow rate of 1 mL/min using a mixture of CH_3CN and 20 mM aqueous NH_4OAc at a ratio of 45:55 as the eluent. At 10 *wt*% loading, the PTX concentrations increased from 1.0 mg/mL to 4.8 mg/mL with increasing polymer concentration for both micelles and SCKs (Table 3.1, entries 1-4 and 7-9, respectively). These nanoparticles were visually stable in nanopure water, without any precipitation and could be stored for more than 1 month at 4 °C. However, when the loading percentage increased to 15 or 20 *wt*% (Table 3.1, entries 5 and 6, respectively), the obtained nanoparticles were only stable in nanopure water for *ca.* 2 d, at which time significant quantities of white precipitates were visualized. Incorporation of PTX into micelles or SCKs appeared to be highly effective, as all initially added PTX was visibly dispersed within the transparent particle solutions at

high concentrations of 10 *wt*% (entry 4 for micelles, entry 9 for SCKs). At such concentrations, both micelles and SCKs demonstrated homogeneous light scattering when a red laser was passed through the solutions, suggesting that well-dispersed nanoparticles encapsulating PTX were prepared (Figure 3.5). Compared with our previous SCK formulations, the PTX concentration in aqueous solution achieved in this study was increased approximately 160 times to 4.8 mg/mL, which is equal to benchmarking systems such as Abraxane® and NK105, as well as many of the high loading polymeric micellar delivery systems reported in the literature.[54,66,142,147]

Table 3.1 Loading capacity of micelles and SCKs and their apparent solution-state stability

Entry	Sample	Polymer (mg/mL)	PTX[a] (μg/mL)	PTX[b] (μg/mL)	Stability[c]
1	micelles-10%-A	9.0	1000	1040	> 1 month
2	micelles-10%-B	13.5	1500	1510	> 1 month
3	micelles-10%-C	18.0	2000	2040	> 1 month
4	micelles-10%-D	45.0	5000	4820	> 1 month
5	micelles-15%	8.5	1500	1490	2 d[d]
6	micelles-20%	32.0	800	-	2 d[d]
7	SCKs-10%-A	9.0	1000	980	> 1 month
8	SCKs-10%-B	18.0	2000	1960	> 1 month
9	SCKs-10%-C	45.0	5000	4950	> 1 month

[a]Theoretical concentration
[b]Concentration measured by HPLC
[c]Stability when stored at 4 °C unless otherwise noted
[d]Sample precipitated when stored at room temperature.

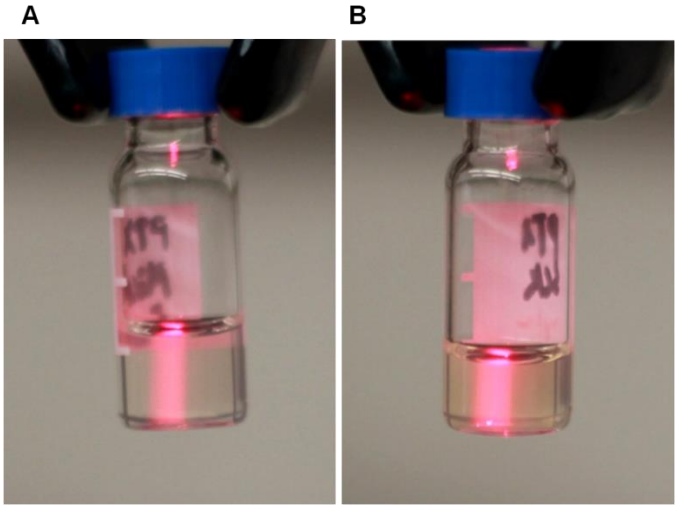

Figure 3.5. Photos of (A) PTX-loaded micelles in nanopure water and (B) PTX-loaded SCKs in nanopure water both at a PTX concentration of 4.8 mg/mL, with a red laser passing through.

The sizes of the micelles and SCKs physically loaded with PTX were characterized both by DLS and transmission electron microscopy (TEM). DLS analysis indicated that the number-averaged hydrodynamic diameters ($D_{h(number)}$) of the particles were 14 ± 4 nm and 24 ± 6 nm (Figure 3.6 A, D), respectively, with negative zeta potentials of -40 mV. TEM images demonstrated that both micelles and SCKs were well-dispersed and had relatively uniform dry-state substrate-adsorbed diameters of *ca.* 42 ± 5 nm and 24 ± 4 nm, respectively (Figure 3.6 B, E). As PPEs are soft materials (T_g = - 51 °C), the micellar structures could not maintain their spherical shapes in the dry state on TEM grids, tending to become flattened, leading to an observed diameter larger than their D_h. Crosslinking to create SCKs limited the extent of deformation of the nanostructures. In an effort to more accurately determine the dry state diameters, cryo-TEM measurements were performed on both PTX-loaded micelles and SCKs, where specimens were

prepared in vitreous ice to view the unaltered macromolecular co–assembly, without shape deformation or staining perturbation (Figure 3.6 C, F). It was confirmed that both micelles and SCKs had diameters of *ca*. 17 nm with narrow size distributions, which was in agreement with data obtained from DLS measurements.

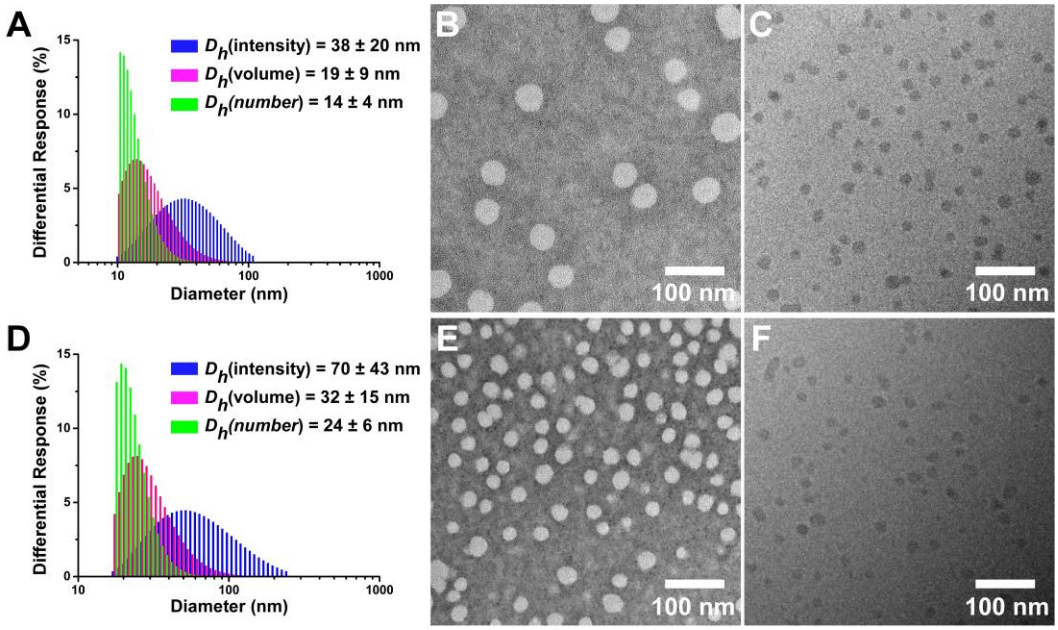

Figure 3.6. Characterization of nanoparticle sizes for PTX loaded micelles (A-C) and SCKs (D-F). Displayed from left to right respectively: DLS histograms displaying their hydrodynamic diameters in nanopure water, TEM sample negatively stained by uranyl acetate, and cryo-TEM images without staining.

The release of PTX from micelles or SCKs was evaluated by monitoring the decreasing concentration of PTX from a solution of loaded micelles or SCKs dialyzed (MWCO 10 kDa) against PBS at 37 °C over 3 days (Figure 3.7). It was found that both micelles and SCKs released PTX at a slow and sustained rate. As expected, shell

crosslinking created an additional physicochemical layer that retarded drug transport through the shell, providing a decreased rate of release for PTX from SCKs, as compared to the corresponding micelle precursors. The apparent PTX release half-life ($t_{1/2}$) from micelles and SCKs were determined to be 6.5 and 12 h, respectively. Therefore, the release profiles can be potentially tuned simply by altering the degree of crosslinking.[41]

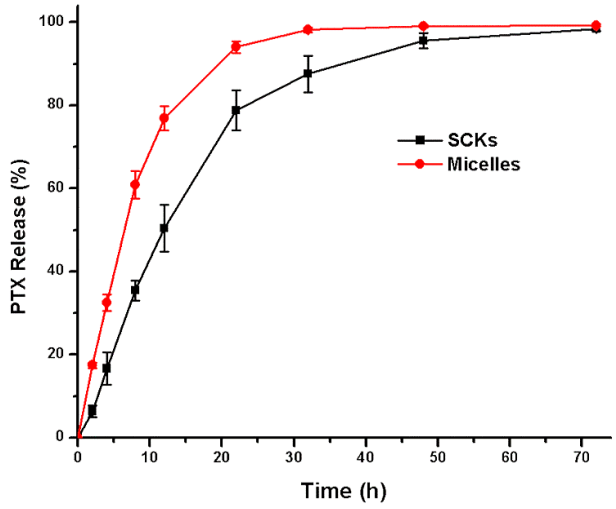

Figure 3.7. Release of paclitaxel that was either loaded into micelles or SCKs and studied by a dialysis method over 3 days at 37 °C in PBS, measured in triplicate.

The *in vitro* hydrolytic degradation of the PEBP-*b*-PBYP-*g*-PEG micelles was evaluated at different pH values utilizing ^{31}P NMR spectroscopy to monitor the cleavage of their phosphodiester backbones and phosphoester side chains (Figure 3.8).[67,168] At neutral pH = 7.4, the nanoparticles displayed high stability, observing only a small degradation peak (<10%) at 0.35 ppm by ^{31}P NMR after incubation in PBS for 103 days

(Figure 3.8 A). Generally, it has been shown that the hydrolytic degradation rate is greatly influenced by side-chain functionalities, for example, amino group-containing cationic nanoparticles degraded much faster compared to anionic, non-ionic and zwitterionic nanoparticles.[67,100,169-171] We hypothesize that the increased stability of PEBP-*b*-PBYP-*g*-PEG arises from not only a lack of nucleophiles in the neutral PBS, but also the densely-packed $mPEG_{2k}$ grafted surface, which leads to limited exposure of the polymer to nucleophiles within the surrounding environment. As expected, the extent of hydrolysis increased significantly under both acidic (pH = 1, Figure 3.8 B) and basic conditions (pH = 10, Figure 3.8 C).[168] For example, at pH = 10 the ^{31}P NMR signal from PBYP decreased by more than 70% after 115 d.

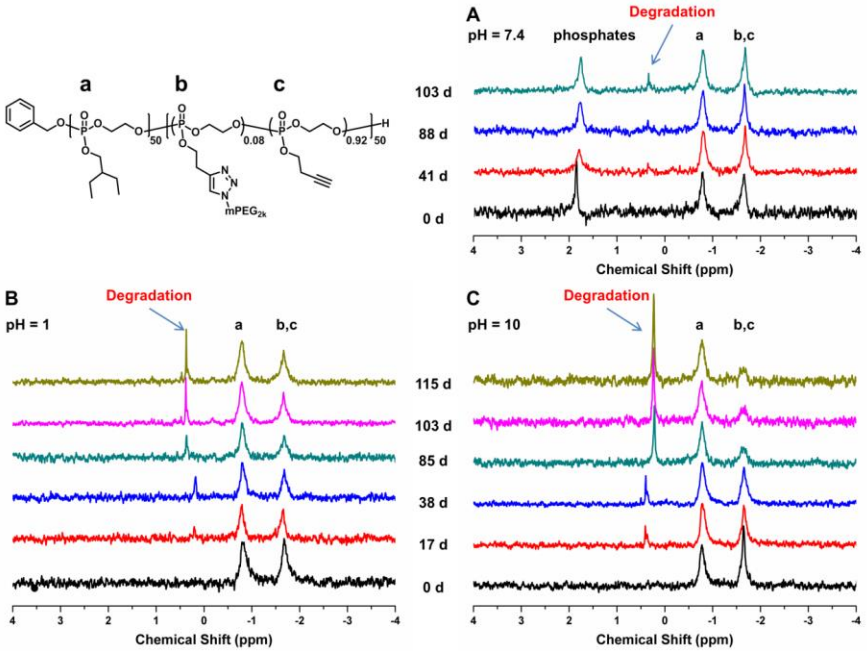

Figure 3.8. Changes in ^{31}P NMR for micelles as a function of hydrolytic degradation times in (A) PBS (pH = 7.4), (B) HCl/H_2O (pH = 1) and (C) Na_2CO_3/ $NaHCO_3$ (pH = 10).

To investigate the *in vitro* cellular uptake and *in vivo* biodistribution and PK of the PEBP-*b*-PBYP-*g*-PEG micelles and SCKs, a hydrophilic near-infrared (NIR) fluorescent dye IR800CW azide was grafted to the polymer *via* CuAAC in nanopure water (Figure 3.9). The unreacted dye was removed using a Sephadex G-25 column followed by dialysis for 2 d (MWCO 12-14 kDa). Removal of the unconjugated IR800CW dye was confirmed by the disappearance of the free dye peak in DMF GPC (Figure 3.10). Confirmation of covalent dye conjugation for the purified polymer-dye conjugate was also examined by fluorescence spectroscopy. As previously reported for PPE block copolymers, the PPE is capable of undergoing degradation during gel electrophoresis and, thus, alternative spectroscopic techniques (fluorescence anisotropy (r) and intensity averaged fluorescence lifetime (τ_i)) were utilized to confirm successful conjugation (Table 3.2).[172]

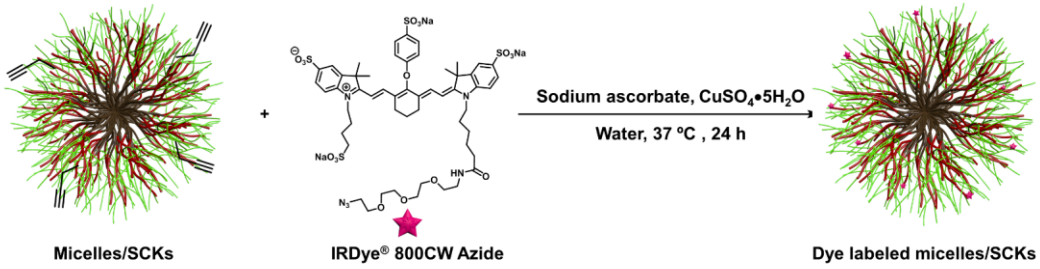

Figure 3.9. Schematic representation of NIR labeling of PEBP-*b*-PBYP-*g*-PEG micelles with IRDye 800CW azide (0.5 eq. to polymer precursor).

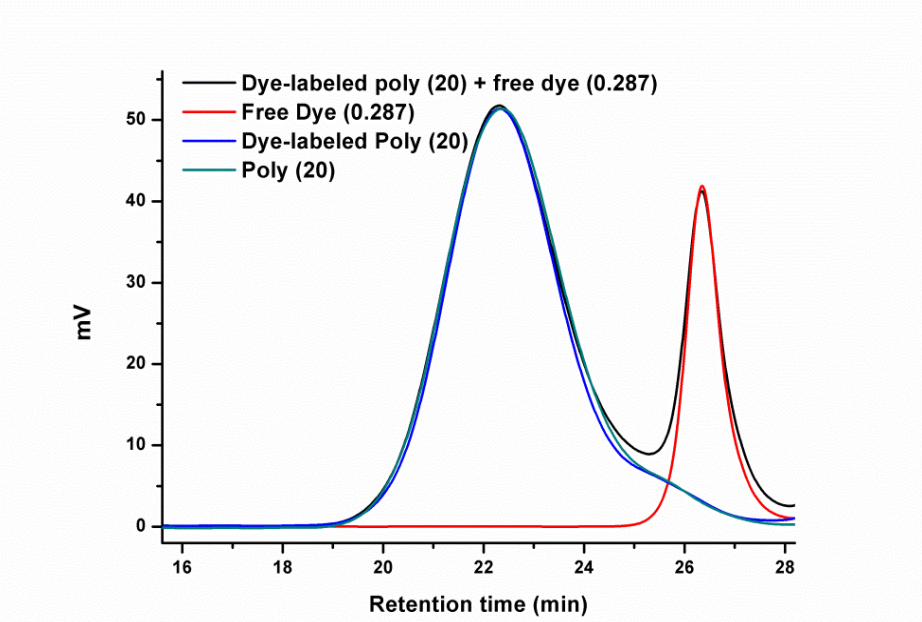

Figure 3.10. The DMF gel permeation chromatography (GPC) traces of free dye (red line), polymer (dark cyan), dye-labeled polymer (blue line), and mixture of free dye and dye-labeled polymer (black line). The values in parentheses correspond to the polymer/dye concentrations (mg/mL) injected into the DMF GPC.

The use of spectroscopic techniques to evaluate dye-nanoparticle conjugation is advantageous, as the results can provide valuable information on the dynamic behavior of the fluorophores within their supramolecular and external environments.[172] In the case of evaluating dye-macromolecule conjugation of NIR cyanine dyes, such as IR800CW, the use of r and τ_i measurements is often considered difficult. The trouble with measuring changes in these spectroscopic properties following conjugation of NIR dyes lies with their short fluorescence lifetimes in aqueous solvents (< 1.0 ns), traditionally elongated structures that lead to high r measurements for the unconjugated dyes (> 0.2) and reliance upon extended linkers utilized for conjugation resulting in higher local mobility or "wobbling" of NIR dyes upon coupling.[173] Therefore, when

utilizing such techniques, small changes that may not be considered of interest in the case of longer-lived and more compact visible-emitting dyes take on increased significance when evaluating conjugation of NIR cyanine-based dyes.

Table 3.2. Fluorescence properties of IR800CW nanoparticle conjugates

Solvent	Sample	λabs (nm)	λem (nm)	*r*	τ_i (ns)	Φ_{FL}
Nanopure H2O	IRDye 800 CW	774	788	0.218 ± 0.006	0.500 ± 0.011	0.086
	Micelles + IR800CW$_a$	774	787	0.221 ± 0.006	0.493 ± 0.012	-
	SCKs + IR800CW[a]	774	789	0.216 ± 0.005	0.492 ± 0.012	-
	IR800CW Micelles	778	792	0.239 ± 0.005	0.668 ± 0.015	0.071
	IR800CW SCKs	778	792	0.241 ± 0.007	0.703 ± 0.017	0.074
PBS pH 7.4	IRDye 800 CW	774	789	0.221 ± 0.006	0.501 ± 0.017	-
	Micelles and Dye[a]	774	789	0.219 ± 0.003	0.489 ± 0.012	-
	SCKs and Dye[a]	774	790	0.220 ± 0.006	0.495 ± 0.012	-
	Dye labeled-micelles	778	792	0.247 ± 0.004	0.678 ± 0.016	-
	Dye labeled-SCKs	778	792	0.240 ± 0.006	0.708 ± 0.016	-

[a]Physical mixtures of polymeric nanomaterial with IR800CW, *r* = steady-state anisotropy, λ_{ex} = 700 nm, and λ_{em} = 820 nm, τ_i = intensity-weighted lifetime, Φ_{FL} = fluorescence quantum yield (relative to ICG = 0.027 in water[174]) [172]

Following grafting of the dye IR800CW to PEBP-*b*-PBYP-*g*-PEG micelles and SCKs, both *r* and τ_i, were evaluated, and changes in both spectroscopic properties were observed (Table 3.2). The *r* and τ_i of both the free dye and physical mixtures of the free dye with polymeric nanomaterials resulted in starting anisotropy values *ca.* 0.220 and τ_i

near 0.500 ns. Upon grafting of the dye to both micelles and SCKs, statistically significant increases in *r* and τ_i were observed in both water and pH 7.4 PBS, indicating that the dye was covalently attached to, rather than physically associated with, the polymeric nanomaterials. By utilizing both aqueous solvents (water and PBS), the effect of crosslinking on the ability of the polymeric materials to interact with the surrounding solvated environment could be probed. In this case, the SCK displayed no change in either the *r* or τ_i measurements, while the micellar particles displayed small changes that are not statistically different. Given the noted nature of such measurements with NIR cyanine dyes, these changes cannot be entirely discounted to lack meaning, but rather may be considered indicative that crosslinking does have an effect upon the ability of these polymeric materials to freely interact with their surrounding environment, which is also supported by previous findings.[16,41,162]

Table 3.3. Comparison of the IC_{50} values of PTX (as a Taxol-mimicking formulation), physically-loaded PTX micelles (both with and without the NIR label IR800CW) and SCKs in both control (OVCAR-3) and osteosarcoma (CCH-OS-O and SJSA) cell lines.

Formulation	IC_{50} (μM)			
	OVCAR-3	RAW 264.7	CCH-OS-O	SJSA
Taxol[a]	0.005 ± 0.002	0.040 ± 0.010	0.019 ± 0.001	0.047 ± 0.006
PTX Micelles	0.015 ± 0.010	0.100 ± 0.040	0.028 ± 0.001	
IR800CW PTX Micelles	0.016 ± 0.009		0.028 ± 0.001	0.068 ± 0.007
PTX SCKs	0.010 ± 0.008	0.080 ± 0.020	0.014 ± 0.001	

[a]Taxol-mimicking formulation: Cremophor-EL and ethanol, 1:1 v/v

The *in vitro* cytotoxic effects of the physically PTX-loaded micelles and SCKs were measured against human ovarian adenocarcinoma cells (OVCAR-3), RAW 264.7 mouse macrophages (RAW 264.7), CCH-OS-O and SJSA cell lines to establish their IC_{50} values at 72 h incubation time, as compared to that of PTX (as a Taxol-mimicking formulation; Cremophor-EL and ethanol, 1:1 *v*/*v*) (Table 3.3). OVCAR-3 cells serve as a control for comparability to previously-studied polymeric chemotherapeutic delivery vehicles,[66,142,175] while the osteosarcoma cell lines CCH-OS-O and SJSA demonstrate the effective toxicity of the PTX-loaded materials towards the targeted disease, lung metastasis of osteosarcoma. Polymeric micelles and SCKs physically-loaded with 10 *wt%* PTX displayed *in vitro* cytotoxicities comparable to those of the Taxol-mimicking formulation. Despite the slower PTX release, PTX-loaded SCKs exhibited only slightly higher cytotoxicity compared to PTX-loaded micelles. As a result of their greater sensitivity to PTX, the difference was more significant on OVCAR-3 cells, in comparison to the other cell lines. The reduced cytotoxic effects of these nanoscopic carriers may be, in part, due to the fast release of lipophilic PTX from the small molecular Cremophor-EL surfactants, which can diffuse passively through cell membranes and cause cytotoxicity. Grafting of IR800CW to the micellar polymer structures had no effect on nanoparticle cytotoxicity in OVCAR-3 or CCH-OS-O cell lines and, thus, is not expected to change the outcomes in RAW 264.7 and SJSA cell lines or as regards the cytotoxicity of the SCKs. As a control, the cytotoxicity of the corresponding nanoparticles without PTX was evaluated, and they were found to be non-toxic at the tested concentrations.

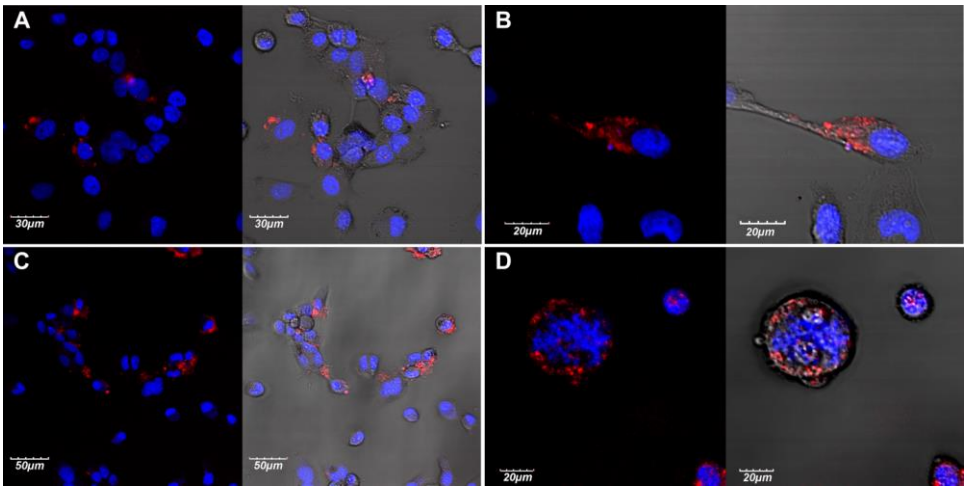

Figure 3.11. Confocal microscopy images demonstrating cellular internalization of both unloaded micelles (A, B) and micelles physically loaded with PTX (C, D) into CCH-OS-O cells (A, magnification = 60x, scale bars = 30 μm; C, magnification = 40x, scale bars = 50 μm; B, D, magnification = 100x, scale bars = 20 μm; blue = DAPI (nuclear stain) and red = IR800CW from NIR labeled micelles). Images to the right overlay fluorescence on the DIC.

After establishing that the IC_{50} values for the PTX-loaded micelles and SCKs in osteosarcoma cell lines were comparable to the pharmaceutical Taxol-mimicking formulation, a cell uptake study by confocal microscopy was conducted, using CCH-OS-O osteosarcoma cells. The resulting images support cellular internalization of both the micellar (Figure 3.11) and SCK (Figure 3.12) nanostructures, whereby nuclear degradation appeared to occur, presumably, upon PTX release within the cellular environment following internalization of PTX-loaded nanoparticles (Figure 3.11 C-D, micelles). When the unloaded micelles and SCKs were taken up by the CCH-OS-O cells (Figure 3.11 A-B, micelles), there appeared to be no effect, which reflected the reported lack of cytotoxicity. These studies further demonstrate the cytotoxicity of these PTX-

loaded materials and highlight their ability to deliver PTX and effectively disrupt the growth of osteosarcoma cells.

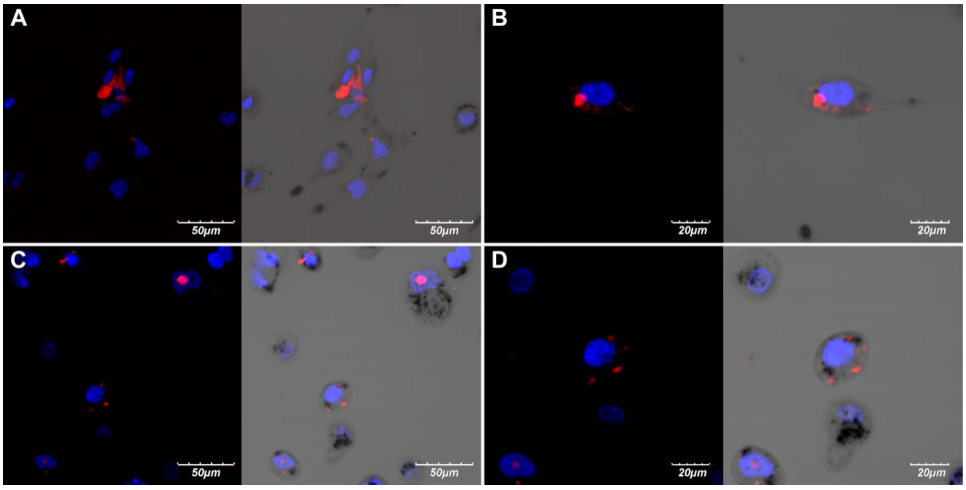

Figure 3.12. Confocal microscopy images demonstrating cellular internalization of both unloaded SCKs (A, B) and SCKs physically loaded with PTX (C, D) into CCH-OS-O cells (A, C, magnification = 60x, scale bars = 50 μm; B, D, magnification = 100x, scale bars = 20 μm; blue = DAPI (nuclear stain) and red = IR800CW from NIR labeled SCKs). Images to the right overlay fluorescence on the DIC.

Previous research utilizing liposomal[95-97] and nanoparticle[176,177] drug formulations has demonstrated that drugs delivered directly to the respiratory tract can result in high pulmonary drug concentration, reduced systemic toxicity, and reduced dosage requirements *vs*. parenteral or oral administration.[95-97] Additionally, these studies revealed that delivery of therapeutics by inhalation-based methods shows great promise towards increased efficacy of treatment, relative to systemic delivery. However, unlike in the case of systemic delivery, these studies have largely avoided evaluating the overall behavior of the nanoparticles themselves as regards lung extravasation and whole body biodistribution. Studies addressing nanoparticle disposition and biokinetics from

aerosol-based treatments have focused on non-degradable and/or inorganic nanoparticles evaluated by *ex vivo* tissue analysis, or concentrated on specific interactions, such as translocation of particles from the lungs to lymph nodes.[97,176-178] While these studies provide valuable information as to nanoparticle location and toxicology, initial screening *via* optical imaging *in vivo* would allow for monitoring of real time trafficking, from which PK data and routes of excretion can be evaluated. Of significant interest was evaluation of the PK of the degradable PEBP-*b*-PBYP-*g*-PEG micelles and SCKs, and determination of whether crosslinking would affect the rate of extravasation (k_{ex}), with correlation to the *in vitro* findings.

In the case of the PEBP-*b*-PBYP-*g*-PEG micelles and SCKs presented herein, it was hypothesized that the degradable polymer-based nanoparticles themselves would be capable of extravasation from the lungs and secondary organs on a timeline compatible with repeated dosing of PTX, but that the rate of lung extravasation for micelles *vs.* SCKs would be different, due to the increased stability imparted to SCKs through crosslinking. The hypothesis, as regards extravasation of micelles *vs.* SCKs, was supported by previously reported findings where crosslinked SCKs were shown to have higher morphological stability, undergo slower disintegration, and elicit lower immuno-toxicity than their non-crosslinked micellar analogs.[100] Nanoparticle PK were indirectly evaluated by NIR optical imaging, following intratracheal administration to ensure that extravasation of the majority of the delivery vehicle largely occurred within the 1-2 week time frame largely considered appropriate for repeated dosing.[179]

IR800CW Azide, PEBP-*b*-PBYP-*g*-PEG-*g*-IR800CW micelles or SCKs (λ_{ex} = 778 nm, λ_{em} = 792 nm) were administered intratracheally to six mice each. All mice were monitored over 7 to 14 days by whole body optical imaging on a Bruker Xtreme™ *in vivo* preclinical imaging system. The biodistribution of each dye/nanoparticle was imaged at regular intervals, directly post injection (PI), at 2, 6, 12 and 24 h PI and then daily until the appropriate endpoint of either 7 or 14 d PI (n = 3 mice at each endpoint *per* injected dye/nanoparticle to reach statistical significance) (Figure 3.13 A). For all images, normalized fluorescence intensities over the lung region were obtained through image analysis and plotted *vs.* time to generate PK profiles (Figure 3.13 B) for each experimental group (IR800CW azide, micelles or SCKs). The rate of extravasation from the lungs (k_{ex}) and $t_{1/2}$ were obtained by fitting the PK profile with a non-linear curve fit (Table 3.4). At the study endpoint, tissue and organs were harvested (liver, kidney, spleen, skin, muscle, brain, lung, heart, blood and the GI tract (stomach, intestines, cecum, *etc*.)) and imaged *ex vivo* to obtain endpoint biodistribution data (Figure 3.13 C). PK analysis established the lung extravasation $t_{1/2}$ for the PEBP-*b*-PBYP-*g*-PEG-*g*-IR800CW micelles to be *ca*. 4 d (Table 3.4), whereas the small molecule NIR probe exhibited a $t_{1/2}$ of 4 h, with > 85% cleared from the lungs within 12 h and the entire body within 1-2 d (Figure 3.13 A, B). The micellar $t_{1/2}$ was supported by the imaging results, suggesting that micelles exhibit extended lung retention of >14 d, at which time the $t_{1/2}$ indicates *ca.* 7 - 10% of the original micelle dose should remain present. Alternatively, the polymeric SCKs display a $t_{1/2}$ of *ca.* 8 d, twice that of their micellar counterparts. The difference in extravasation rates is most likely due to a change in the structure-

function relationship, whereby crosslinking leads to added structural stability and decreased interactions with the surrounding biological environment, as compared to the micellar structures, supporting the findings of the NIR spectroscopy study above. We hypothesize that the resulting decrease in external interactions with fluids and other biological elements (proteins, enzymes, *etc*.) would decrease opportunities for externally induced degradation (*e.g.* enzymatic) resulting in the observed longer $t_{1/2}$. These studies and findings may be complicated by the indirect detection method, whereby the dye is being tracked independent of whether it is bound to the original nanoparticle, disassembled polymer chains, or partial fragments due to cleavage of the dye from the polymer backbone or polymer backbone degradation. However, the significantly faster biological clearance of the small molecule dye suggests that the micelle and SCK studies were, in fact, measurements predominantly of nanoparticle/polymer clearance rates.

Table 3.4. Pharmacokinetics of the dye IR800CW azide and its micellar and SCK conjugates.

Agent	Latency (d)	k_{ex} (d^{-1})	$t_{1/2}^{*}$ (d)
IR800CW Azide	0.08	9.29	0.16
Micelles	0.08	0.17	4.18
SCKs	2.00	0.11	8.28

K_{ex} = rate of extravasation from the lungs
*$t_{1/2} = t_{1/2}$ + Latency

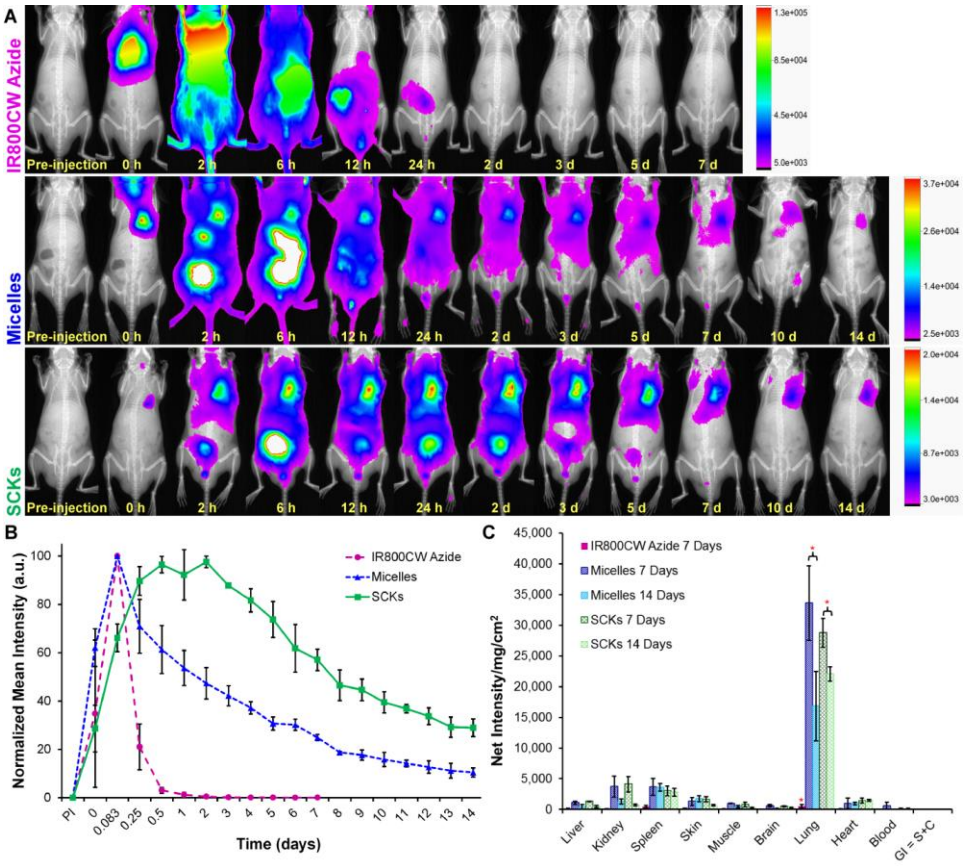

Figure 3.13. (A) The overlaid optical on X-ray images of the small molecule dye IR800CW Azide (top) *vs.* PEBP-*b*-PBYP-*g*-PEG-*g*-IR800CW micelles (middle) and SCKs (bottom) collected as a function of time. (B) PK profiles of normalized mean fluorescence intensity as a function of time for the free dye (IR800CW azide) and IR800CW labeled micelles and SCKs. (C) The quantified biodistribution data collected *ex vivo* on harvested organs at 7 and 14 days PI for IR800CW azide *vs.* IR800CW labeled micelles and SCKs.

Ex vivo fluorescence imaging of the collected tissue and organs was evaluated to confirm that the nanomaterials remained largely in the lungs, and to identify secondary organ systems that may have accumulated small quantities of nanomaterials or potential degradation products. Semi-quantitative analysis (Figure 3.13 C) reveals that the major site of nanoparticle accumulation, for both micelles and SCKs, was in the lungs (the site

of administration) at both 7 and 14 days PI. The clearly observed difference between retention of nanoparticle formulations and unconjugated IR800CW azide over 7 days is statistically significant based upon a student's t-test (n = 3), and supports the reported *in vivo* PK studies. Evaluation of both the *in vivo* and *ex vivo* findings suggests that at least two routes of extravasation from the lungs and excretion from the body may have taken place concurrently. *In vivo* studies revealed both early clearance to the bloodstream and through the mucociliary tract, due to repeated coughing up and swallowing of the micelles or SCKs. Over time, extravasation from the lungs *via* the mucociliary tract was observed to become negligible, as later images revealed accumulation largely within the kidney and liver, indicating the primary route of extravasation was into the blood. *Ex vivo* findings indicated limited accumulation of both nanomaterials in the kidney and liver, demonstrating that both micelles and SCKs were excreted concomitantly *via* both the renal and hepatobiliary pathways. When considering the degradable nature of these materials, the findings were not unexpected, as degradation by-products could be of a multitude of sizes (from partly intact polymers or nanoparticle pieces to small molecules) that are capable of undergoing excretion from the body *via* either pathway, depending on size.[16] Overall, the $t_{1/2}$ and biodistribution results support the ability of both the micelles and SCKs to undergo extravasation from the lungs and whole body excretion within a timeline reasonable for repeated dosing on a weekly or biweekly basis.

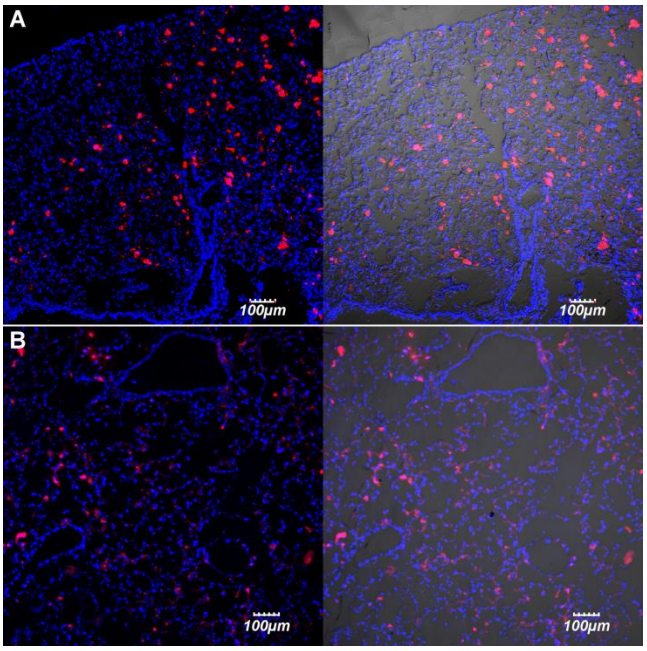

Figure 3.14. Representative *ex vivo* confocal microscopy z-stack of 20 μm lung sections 7 days PI of IR800CW labeled (A) micelles and (B) SCKs (10x, scale bar = 100 μm) supporting distribution of the nanoparticles throughout the lungs of healthy mice (blue = DAPI (nuclear stain) and red = IR800CW NIR labeled nanoparticles). Images to the right overlay fluorescence on the DIC.

To confirm that intratracheal delivery did not solely deliver the PEBP-*b*-PBYP-*g*-PEG-*g*-IR800CW micelles and SCKs to the location of deposition within the lungs, but rather that the nanoparticles are capable of distributing throughout the lung tissue, the general location of the particles was evaluated by confocal microscopy on frozen lung sections. The lungs of mice treated with IR800CW micelles and SCKs (n = 3 for each particle) were filled with a 50/50 solution of sterile water/OCT, frozen and sliced at a thickness of 20 μm in a cross-sectional manner from the distal to proximal end, such that both the left and right lobes were included in each section. Fluorescence images of lung sections (Figures 3.14 and 3.15 display representative images) were obtained after

applying mounting media containing DAPI for nuclear staining. NIR signal from IR800CW-labeled nanoparticles was observed throughout both the left and right lobes at distal, medial and proximal locations for all treated mice, while untreated controls lacked fluorescence signal in the NIR region. Such outcomes indicated that the nanomaterials were capable of migrating from the point of administration throughout the lung, which would be vital in the treatment of widespread metastatic disease.

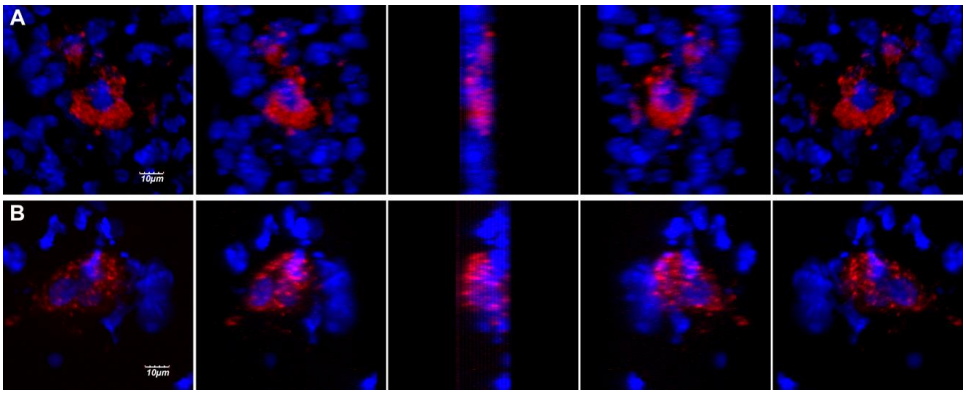

Figure 3.15. Representative *ex vivo* confocal microscopy images of a 3D reconstruction of 20 μm lung sections (From left to right: 0º, 45º, 90º, 135º, 180º) 7 days PI of IR800CW labeled (A) Micelles and (B) SCKs (160x, scale bar = 10 mm) indicating the nanomaterials are able to enter the cellular microenvironment surrounding the nucleus *in vivo*. (blue = DAPI (nuclear stain) and red = IR800CW NIR labeled nanoparticles).

3.4 Conclusions

Polyphosphoester-based amphiphilic block graft terpolymers have been prepared by efficient "click-type" reactions, and were able to undergo co-assembly with PTX to form well-defined nanoparticles, as supramolecular micelles and covalently-stabilized SCKs. Characterization of the resulting nanotherapeutics demonstrated that they exhibited

desirable physiochemical properties when loaded with up to 10 wt% of PTX, a concentration of 4.8 mg/mL in aqueous solution that was a 160-fold increase over our previous SCK formulations.[50] During subsequent drug release studies, it was observed that the $t_{1/2}$ of PTX release for SCKs is nearly double that of their micellar counterparts (12 *vs*. 6.5 h respectively). These results demonstrated that crosslinking was capable of mediating PTX release by forming an additional physicochemical layer through the shell, the tuning of which could be utilized to further tune the performance of these nanoscopic containers. Residual alkynyl groups along the backbones were modified by attaching the NIR dye IR800CW, enabling their use *in vivo* and *ex vivo* imaging-based studies.

The promising features displayed by these PTX-loaded nanoparticles led to further investigation of their *in vitro* and *in vivo* characteristics to evaluate potential efficacy against known metastatic osteosarcoma cell lines and the potential of the particles towards direct administration to the lung for the treatment of metastatic osteosarcoma tumors. *In vitro*, these micellar formulations had comparable cytotoxicities with the commercially available Taxol®- mimicking formulation, further validating them as excellent candidates for translational studies. *In vivo* evaluation of the pharmacokinetics and biodistribution, following intratracheal delivery, revealed that crosslinking has the ability to control the rate of nanoparticle extravasation from the lungs. SCKs were observed to be retained for almost twice the time of their micellar equivalents, *ca.* 8 d *vs*. 4 d respectively. These extravasation timelines appear to be reasonable for translational development when considering the repeating dosing schedules already in place for PTX

chemotherapeutics. Interestingly, we have shown that the structure-function relationship of nanomaterials not only affects *in vitro* outcomes, but also has implications on *in vivo* performance and pharmacokinetics following intratracheal delivery to the lungs.

Given the findings presented herein, these new PEBP-*b*-PBYP-*g*-PEG chemotherapeutic delivery vehicles have great potential as nanocarriers, providing sustained release treatments *via* administration directly to the site of lung metastasis of osteosarcoma. This initial work has established the ability to load drugs into well-designed polymer nanoparticle frameworks, achieve *in vitro* efficacy against relevant cancer cells, and probe the *in vivo* biodistribution of the non-loaded nanoparticles in healthy animals to understand their trafficking behaviors. Important for tailoring this platform is the presence of remaining unreacted alkynes, which could be adapted for further modification, such as attachment of targeting ligands and grafting of imaging agents to evaluate biodistribution and nanoparticle location within tissues. However, key issues remain to be investigated, including the relationships between *in vitro vs*. *in vivo* rates of degradation of the particles and release of drug molecules, the independent trafficking globally and at the cellular level in diseased *vs*. healthy tissues, and the behaviors for each of the drug and carrier components, whether intact or in a fragmented form. Clearly, there is much chemistry and biology remaining to be understood, with this work being an important first step, for continuing ongoing studies.

CHAPTER IV

DEGRADABLE POLYPHOSPHOESTER-BASED SILVER-LOADED NANOPARTICLES AS THERAPEUTICS FOR BACTERIAL LUNG INFECTIONS [*]

4.1 Introduction

Despite current advancements in modern medicine, infectious diseases, especially pulmonary infections, continue to pose great clinical challenges to successful medical treatment.[86,180] In 2012, lower respiratory infections were reported as the second leading cause of years-of-life lost (YLL) worldwide.[181] One of the contributing factors is widespread antibiotic resistance, which enables antibiotic-resistant bacteria, such as *Enterococcus faecium, Staphylococcus aureus, Klebsiella pneumoniae, Acinetobacter baumanii, Pseudomonas aeruginosa,* and *Enterobacter species* (ESKAPE), to survive despite treatment with existing antibacterial drugs.[86-88] The growing number of multi-drug resistant strains has made imperative the development of new antibiotics and novel approaches to deliver existing agents.[86,89-91]

Silver has been used as an antimicrobial agent for centuries, especially in the

[*] Reprinted (adapted) with permission from "Degradable polyphosphoester-based silver-loaded nanoparticles as therapeutics for bacterial lung infections" by Zhang, F.; Smolen, J. A.; Zhang, S.; Li, R.; Shah, P. N.; Cho, S.; Wang, H.; Raymond, J. E.; Cannon, C. L.; Wooley, K. L., *Nanoscale*, 2015, *7,* 2265-2270. http://pubs.rsc.org/en/content/articlehtml/2015/nr/c4nr07103d. Copyright 2015 The Royal Society of Chemistry (RSC).

topical treatment of wounds and burns.[182] Silver cations are well known to be highly toxic against a broad spectrum of microorganisms, while metallic silver has minimal antimicrobial activity.[183-185] Although their biocidal mechanisms are not fully understood, silver cations have been reported to cause bacterial protein denaturation, enzyme oxidation, and interference with DNA replication.[186,187] Furthermore, unlike traditional antibiotics, silver cations exhibit low toxicity to human tissues and documented instances of bacterial resistance are rare.[180,188,189] Therefore, various silver-based antimicrobials have been developed. For example, silver sulfadiazine (AgSD) cream, which was introduced in the 1960s, has become a routine remedy in the treatment of burns over the last few decades.[182,190] However, silver cation-based small molecules are often not practical *in vivo*, because free Ag^+ will interact with anions and other biological compounds in the human body, decreasing the bioavailability of free Ag^+.[180,185,191] Therefore, there is a remaining need to develop a drug-delivery system that can effectively carry the silver-based antimicrobials to the infected tissues with minimal inactivation of these drugs.

Recently, several nanosized systems for the delivery of silver-based small molecules have been developed to improve bioavailability and efficacy.[35,191-194] Our group has investigated shell crosslinked knedel-like (SCK) nanoparticles, comprised of poly(acrylic acid)-*block*-polystyrene (PAA-*b*-PS) block copolymers, for the packaging and delivery of both silver cation and hydrophobic 1-hexyl-3-methyl-4,5-dichloro-imidazole-2-ylidene silver(I) acetate (silver carbene complex, SCC10). Although these PAA-*b*-PS based SCKs displayed lower antimicrobial activities

compared to $AgNO_3$ *in vitro*, they exhibited remarkably-enhanced therapeutic efficacy *in vivo*.[35,193] A key drawback to these materials, however, is their stable, non-degradable structure, which raises concerns about their clearance from the body, possible side effects from their extended retention, and also their environmental persistence. Moreover, the electrostatic interaction between silver cations and the carboxylates of the acrylic acid residues is weak, leading to instability, formation of AgCl precipitates when challenged by saline solution, and relative ineffectiveness *in vivo* for the SCKs loaded only with Ag cations.[35,193]

To address these problems, we have designed and synthesized an amphiphilic block terpolymer with a hydrolytically-degradable polyphosphoester-based backbone and side chain functionalities that allow for stronger binding of silver cations.[61,74,99,100,195] The alkyne side chains are designed to incorporate silver *via* reversible interactions between silver cations and alkynes, which has been traditionally employed in various catalytic processes.[196-199] A portion of the alkynes was consumed for the installation of methoxypolyethylene glycol (mPEG), which was grafted onto the backbone *via* copper(I)-catalyzed alkyne-azide cycloaddition (CuAAC) reactions to increase hydrophilicity and enhance mucosal transport.[15,163-165,200] These alkyne groups also offer opportunities for further modifications, such as crosslinking to increase nanoparticle stability and addition of fluorescent probes or radiolabeling sites for investigation of trafficking *in vitro* and *in vivo*.[15,36,100,117,201] Finally, the alkyl side chains impart hydrophobicity, allowing the formation of micelles with core-shell morphology, as well as providing avenues to load potential

hydrophobic drugs, for example hydrophobic silver carbene complexes including SCC10,[192] for combination drug delivery.

4.2 Materials and methods

4.2.1 Materials

2-Chloro-2-oxo-1,3,2-dioxaphospholane (95%) was used as received from Thermo Fisher Scientific, Inc. (Pittsburgh, PA). Chelex 100 resin was used as received from Bio-Rad Laboratories (Hercules, CA). Tetrahydrofuran (THF) and dichloromethane (DCM) were dried through a purification column system (J. C. Meyer Solvent Systems, Inc., Laguna Beach, CA). α-Methoxy-ω-azido PEG_{2k} (M_n = 1,950 kDa, M_w/M_n = 1.03) was purchased from RAPP POLYMERE (Tuebingen, Germany). All other chemicals were purchased from Sigma-Aldrich (St. Louis, MO) and used without further purification, unless otherwise noted. Slide-A-Lyzer dialysis cassettes (10 kDa molecular weight cut-off, MWCO) were purchased from Pierce Biotech. (Rockford, IL). The Spectra/Por dialysis membranes (MWCO 12-14 kDa) were purchased from Spectrum Laboratories, Inc. (Rancho Dominguez, CA). Nanopure water (18 MΩ·cm) was acquired by means of a Milli-Q water filtration system, Millipore Corp. (Bedford, MA). Dr. Maynard Olson (University of Washington, Seattle, WA) provided the laboratory strain PAO1-V, and Dr. Thomas Ferkol (Washington University, St. Louis, MO) provided the mucoid, cystic fibrosis clinical isolate PAM57-15. PAHP3, BG80, BM54, SALL06, and SAEH05 were cultured and isolated from cystic fibrosis patient sputum at St. Louis Children's Hospital (St. Louis, MO). The USA300 strain of methicillin-resistant *S. aureus*, TCH1516, was acquired from ATCC (BAA-1717).

4.2.2. Instrumentation

^{1}H NMR and ^{13}C NMR spectra were recorded on a Varian Inova 300 spectrometer interfaced to a UNIX computer using VnmrJ software. Chemical shifts were referenced to the solvent residual signals.

FTIR spectra were recorded on an IR Prestige 21 system using a diamond ATR lens (Shimadzu Corp., Japan) and analyzed using IRsolution v. 1.40 software.

The DMF gel permeation chromatography (GPC) was conducted on a Waters Chromatography, Inc. (Milford, MA) system equipped with an isocratic pump model 1515, a differential refractometer model 2414, and a three-column set of Styragel HR 4 5 μm DMF (300 × 7.5 mm), Styragel HR 4E 5 μm DMF (300 × 7.5 mm), and Styragel HR 2 5 μm DMF (300 × 7.5 mm). The system was equilibrated at 70 °C in pre-filtered DMF containing 0.05 M LiBr, which served as polymer solvent and eluent (flow rate set to 1.00 mL/min). Polymer solutions were prepared at a concentration of *ca*. 3 mg/mL and an injection volume of 200 μL was used. Data collection and analysis were performed with Empower 2 v. 6.10.01.00 software (Waters, Inc.). The system was calibrated with polystyrene standards (Polymer Laboratories, Amherst, MA) ranging from 615 to 442,800 Da.

Dynamic light scattering (DLS) measurements were conducted using a Delsa Nano C (Beckman Coulter, Inc., Fullerton, CA) instrument equipped with a laser diode operating at 658 nm. Size measurements were made in nanopure water ($n = 1.3329$, $\eta = 0.890$ cP at 25 ± 1 °C). Scattered light was detected at a 165° angle and analyzed using a log correlator over 70 accumulations for a 3.0 mL sample in a glass sizing cell (4.0 mL

capacity). The photomultiplier aperture and the attenuator were automatically adjusted to obtain a photon counting rate of *ca*. 8 kcps. Calculations of the particle size distribution and distribution averages were performed using CONTIN particle size distribution analysis routines. The peak averages of histograms from number distributions out of 70 accumulations were reported as the average diameters of the particles. The particle ζ-potential values were determined by a Delsa Nano C particle analyzer (Beckman Coulter, Fullerton, CA) equipped with a 30 mW dual laser diode (658 nm). The ζ-potential of the particles in suspension was obtained by measuring the electrophoretic movement of charged particles under an applied electric field. Scattered light was detected at a 15° angle at 25 °C. The ζ-potential was measured at five regions in the flow cell, and a weighted mean was calculated. These five measurements were used to correct for electro-osmotic flow that was induced in the cell due to the surface charge of the cell wall. All determinations were repeated five times.

Glass transition temperatures (T_g) were measured by differential scanning calorimetry on a Mettler-Toledo DSC822® (Mettler-Toledo, Inc., Columbus, OH), with a heating rate of 10 °C/min. Measurements were analyzed using Mettler-Toledo Star^e v. 7.01 software. The T_g was taken as the midpoint of the inflection tangent, upon the third heating scan. Thermogravimetric analysis was performed under N_2 atmosphere using a Mettler-Toledo model TGA/SDTA851^e, with a heating rate of 10 °C /min. Measurements were analyzed by using Mettler-Toledo Star^e v. 7.01 software.

Transmission electron microscopy (TEM) images were collected on a JEOL 1200EX operating at 100 kV and micrographs were recorded at calibrated magnifications using a

SIA-15C CCD camera. The samples as aqueous solutions (4 μL) were deposited onto carbon-coated copper grids, and after 1 min, the excess of the solution was quickly wicked away by a piece of filter paper. A drop of 1 *wt*% uranyl acetate was then added, and allowed to stand for 30 seconds before excess stain was wicked away. The grids were allowed to dry in air overnight. High-resolution scanning transmission electron microscopy (STEM) and elemental mapping were conducted on a FEI Tecnai G2 F20 FE-TEM coupled with energy-dispersive X-ray (EDX), operating at a voltage of 200 kV with a Gatan CCD camera.

The atomic force microscopy (AFM) imaging was performed on a MFP-3D system (Asylum Research) in tapping mode using standard silicon tips (VISTAprobes, CSR-25, resonance constant: 28 kHz, tip radius: <10 nm, spring constant: 0.1 N/m). For AFM sample preparation, nanoparticles were dissolved in nanopure water at 0.025 mg/mL, and 10 μL of the sample was spin-coated onto a mica surface and allowed to dry in air overnight.

A B&W Tek iRaman system (785 nm, 300 mW max) was used to assess the polyphosphoester system upon association with silver. Measurements were obtained through a 20x objective (PLL, Olympus) at 30 mW with 1 s integration averaged over 10 spectra. Relative populations for the species in the acetylide fingerprint region were assessed by peak deconvolution using Origin 9.0 Pro software package.

The concentration of silver was measured by inductively coupled plasma-mass spectrometry (ICP-MS) on Perkin Elmer DRCII ICP-MS. The element/mass detected was ^{107}Ag and the internal standard used was ^{103}Rh.

4.2.3. Experimental procedures

Synthesis of EBP and BYP monomers. 2-(But-3-yn-1-yloxy)-2-oxo-1,3,2-dioxaphospholane (BYP) and 2-(2-ethylbutoxy)-1,3,2-dioxaphospholane (EBP) were synthesized as previously described.[61]

Synthesis of PEBP-*b*-PBYP diblock copolymer. A solution of EBP (1.5 g, 7.2 mmol) and benzyl alcohol (15.6 mg, 0.14 mmol) in 2.1 mL anhydrous dichloromethane was transferred *via* syringe into a flame-dried vial equipped with a stir bar and rubber septum, under N_2, in an water/ice bath. A solution of 1,5,7-triazabicyclo[4.4.0]dec-5-ene (TBD) (40.2 mg, 0.29 mmol) in 0.3 mL anhydrous dichloromethane was injected quickly into the vial. After being stirred for 2 min, another 2.4 mL of anhydrous dichloromethane was injected into the vial to dilute the reaction mixture, and the vial was transferred to a cooling bath composed of equal amounts of ice/water and sodium chloride at -10 °C. Less than 0.1 mL of the reaction mixture was withdrawn and diluted with $CDCl_3$ to determine the EBP conversion by ^{31}P NMR. After stirring for another 2 min, the reaction mixture was augmented with a solution of BYP (1.27 g, 7.2 mmol) in 2.4 mL anhydrous dichloromethane *via* syringe. The reaction was quenched by adding an excess amount of acetic acid dissolved in DCM after another 3 min, and an aliquot of the mixture was used to determine the conversion of BYP by ^{31}P NMR. The PEBP-*b*-PBYP was purified by precipitation from acetone into a pentane/diethyl ether mixture (3:1 volume ratio) three times and then dried under vacuum. . ^1H NMR (300 MHz, $CDCl_3$, ppm): δ 0.89 (t, J = 7.2 Hz, $POCH_2CH(CH_2C\mathit{H}_3)_2$), 1.37 (m, $POCH_2CH(C\mathit{H}_2CH_3)_2$), 1.50 (m, $POCH_2C\mathit{H}$), 2.11 (s, $POCH_2CH_2C{\equiv}C\mathit{H}$), 2.62 (m,

$POCH_2CH_2C{\equiv}CH$), 4.00 (m, $POCH_2CH$), 4.12–4.39 (m, $POCH_2CH_2OP$, $POCH_2CH_2$), 5.08 (d, J = 8.3 Hz OCH_2Ar), 7.32–7.41 (m, Ar-*H*); ^{13}C NMR (75 MHz, $CDCl_3$, ppm): 10.99, 20.69, 22.75, 41.55, 65.52-67.11, 70.08, 70.88, 79.59; ^{31}P NMR (121 MHz, $CDCl_3$, ppm): δ -1.25, -1.81. GPC: M_n = 25200 g/mol, PDI = 1.25. DSC: T_g = -59°C, - 45 °C. TGA in N_2: 180-365 °C, 58% mass loss; 365–500 °C, 6.1% mass loss, 35% mass remaining above 500 °C. IR (cm^{-1}): 3700-3150, 3000-2800, 1645, 1464, 1379, 1267, 1009, 966, 868, 806.

Azide-alkyne Huisgen cycloaddition of PEBP-*b*-PBYP with α-methoxy-ω-azido PEG (CH_3O-PEG_{2k}-azido). In a typical experiment, a dried vial containing a magnetic stir bar was charged with PEBP-*b*-PBYP (0.83 g, 43 μmol, 1 eq.), α-methoxy-ω-azido PEG (0.33 g, 0.17 mmol, 4 eq.), *N*,*N*,*N*′,*N*′,*N*″-pentamethyldiethylenetriamine (PMDETA, 12 mg, 69 μmol, 1.6 eq.) and 7 mL of DMF. The reaction mixture was degassed by several freeze-pump-thaw cycles (N>3), during which copper(I) bromide (4.9 mg, 34 mmol, 0.8 eq.) was added. The flask was allowed to return to room temperature after the final cycle and stirred for another 4 h. The solution was subsequently filtered through a neutral alumina column and dialyzed against Chelex 100 resin in nanopure water in presoaked dialysis tubing (MWCO.*ca*. 6–8 kDa) for 2 d to remove copper ions, followed by lyophilization to yield white powder with a 70 % yield. Inductively coupled plasma-mass spectrometry (ICP-MS) confirmed that less than 10 ppm of copper was present in the polymer. ^1H NMR (300 Hz, $CDCl_3$, ppm): δ 0.90 (t, J = 7.5 Hz, $POCH_2CH(CH_2CH_3)_2$), 1.37 (m, $POCH_2CH(CH_2CH_3)_2$), 1.50 (m, $POCH_2CH$), 2.11 (s, $POCH_2CH_2C{\equiv}CH$), 2.56-2.65 (m, $POCH_2CH_2C{\equiv}CH$), 3.12 (m, NCH_2CH_2), 3.38

(s, OCH_3), 3.64 (s, OCH_2CH_2), 4.00 (m, POCH_2CH), 4.14-4.39 (m, POCH_2CH_2, POCH_2CH_2OP), 5.08 (d, J = 8.4 Hz, OCH_2Ar), 7.31-7.41 (m, Ar-H), 7.60-7.66 (m, $CH_2CH_2CCHNCH_2$). ^{13}C NMR (75 MHz, $CDCl_3$, ppm): δ 11.03, 20.72, 22.79, 41.60, 65.52-67.15, 70.13, 70.68, 70.95, 79.72, 128.06, 128.73. ^{31}P NMR (121 MHz, $CDCl_3$, ppm): δ -0.99, -1.64. GPC: M_n = 31300 g/mol, PDI = 1.26. DSC: T_g = - 52 °C; T_m = 42 °C. TGA in N_2: 180–265 °C, 41% mass loss; 265–380 °C, 32% mass loss, 360–600 °C, 1% mass loss, 26 % mass remaining above 600 °C. IR (cm^{-1}): 3800-3050, 3050-2700, 1651, 1460, 1348, 1271, 1016, 964, 866, 803.

Silver loading into micelles. In a typical experiment, PEBP-*b*-PBYP-*g*-PEG (32.0 mg, 1.0 eq.) was dissolved in 3.2 mL of nanopure water and sonicated for 3 min. Silver acetate (9.0 mg, 46 eq.) in 2.0 mL of nanopure water was added, and the mixture solution was shaded with aluminum foils and stirred overnight. The solution was transferred to a centrifugal filter device (100 kDa MWCO), and washed extensively for several cycles (N>3) with nanopure water to remove free small molecules. The amount of silver loaded into the micelles was quantified by ICP-MS using rhodium as an internal standard.

Release of silver from silver-loaded micelles. The release profiles of the silver-loaded micelles were studied by monitoring the decrease of silver concentration over time in dialysis cassettes by ICP-MS. In a typical procedure, 3.0 mL of silver-loaded micelles was transferred into a presoaked dialysis cassette. The cassette was allowed to stir in a beaker containing 3000 mL nanopure water or phosphate buffer (10 mM phosphate, 10 mM NaCl, pH 7.4) at 37 °C. Aliquots (*ca.* 0.05 mL) were taken at pre-

determined time and silver concentrations were determined by ICP-MS. The release experiments were conducted in a triplicate manner.

Determination of Minimum Inhibitory Concentrations (MICs) and Minimum Bactericidal Concentrations (MBCs). The bacterial strains were streaked from frozen stocks onto tryptic soy agar (TSA) plates and incubated at 37°C for 24-48 h, depending on the growth rate of the strain. Single colonies were then inoculated into Mueller Hinton broth (MHB) and incubated at 37 °C with 200 rpm shaking until they reached an optical density of 0.4 at 650 nm (OD_{650}), corresponding to approximately 5×10^8 CFU/mL. The silver-loaded micelles and silver acetate were suspended/dissolved and diluted in molecular-grade water and added to a 96-well plate (100 µL/well). The bacteria suspensions were diluted 1:500 in double-strength (2X) MHB and added 1:1 by volume to the diluted silver acetate or nanoparticles (10^5 CFU/well). The plates were then sealed with gas-permeable membranes (Breathe-Easy®) and incubated for 18-24 h at 37 °C. MICs were recorded as the lowest concentration of silver that yielded clear replicate wells. To determine MBCs, 100 µL of the contents of each clear well was dispensed onto TSA plates supplemented with 5% sheep blood. The plates were incubated 24-48 h at 37 °C, depending on the strain, and the MBCs were recorded as the lowest concentration of silver that yielded no growth. MIC/MBCs were all performed three times and the results with the highest MIC or MBC amongst the replicates were reported.

Cytotoxicity with AlamarBlue®. 16HBEs, provided by Dr. D. Gruenert (University of California, San Fransisco, CA), are a human bronchial epithelial cell line that were

transformed with SV40 large T-antigen using the replication-defective pSVori plasmid. 16HBEs between passage 20 to 40 were cultured in Minimum Essential Medium with Earle's Balanced Salts with non-essential amino acids and supplemented with penicillin-streptomycin (1%), l-glutamine (1%), and fetal bovine serum (10%). Prior to cytotoxicity studies, the cells were lifted with trypsin, seeded in a 96-well plate (25,000 cells/well), and incubated overnight at 37°C, 5% CO_2, and 100% RH. The silver-loaded micelles and silver acetate were suspended/dissolved and diluted in the same feeding media and added fresh to the cells. After a 24 h incubation, the media with silver was removed and replaced with OPTI-MEM containing 10% AlamarBlue® (Life Technologies Inc.) and the plates were incubated for an additional 6 h. To determine cytotoxicity, the plates were read with a plate-reading spectrophotometer (BMG Labtech) at 570 nm and 600 nm and cell viability was calculated according to manufacturer's instructions. IC_{50} values, based on molar concentration of silver, were calculated by generating a non-linear curve fit and interpolating the concentration yielding 50% inhibition (Graphpad Prism®). Viability assays were performed three times and averaged. Significant difference between the silver-loaded micelles and silver acetate was performed using non-parametric Student's t-test (Graphpad Prism®).

4.3 Results and discussion

The amphiphilic block terpolymer PEBP-*b*-PBYP-*g*-PEG was synthesized by utilizing click-type chemistries (Figure 4.1).[61] Hydrophobic-functional AB diblock polyphosphoesters PEBP-*b*-PBYP were synthesized by one-pot sequential ring-opening polymerizations (ROP) of hydrophobic monomer 2-ethylbutoxy

phospholane (EBP) and alkyne-functionalized 2-butynyl phospholane (BYP) in dichloromethane, with benzyl alcohol as the initiator. PEGylation was achieved *via* CuAAC of PEBP-*b*-PBYP by reaction with azido-terminated mPEG of 2 kDa molecular weight in *N*,*N*-dimethylformamide (DMF), followed by purification using Sephadex G-25 size exclusion chromatography and extensive dialysis against nanopure water to remove copper and other impurities. The gel permeation chromatographic (GPC) analysis (Figure 4.2) demonstrated the successful chain extension from homopolymer PEBP, with a peak maximum retention time at 24.5 min, to obtain the diblock copolymer PEBP-*b*-PBYP, having a peak maximum at 22.7 min. GPC also allowed for confirmation of grafting by PEG, with an observed >98% reduction in the intensity of the non-grafted PEG signal (25.6 min) and a shift of the grafted polymer product to shorter retention time (22.0 min) (Figure 4.2).

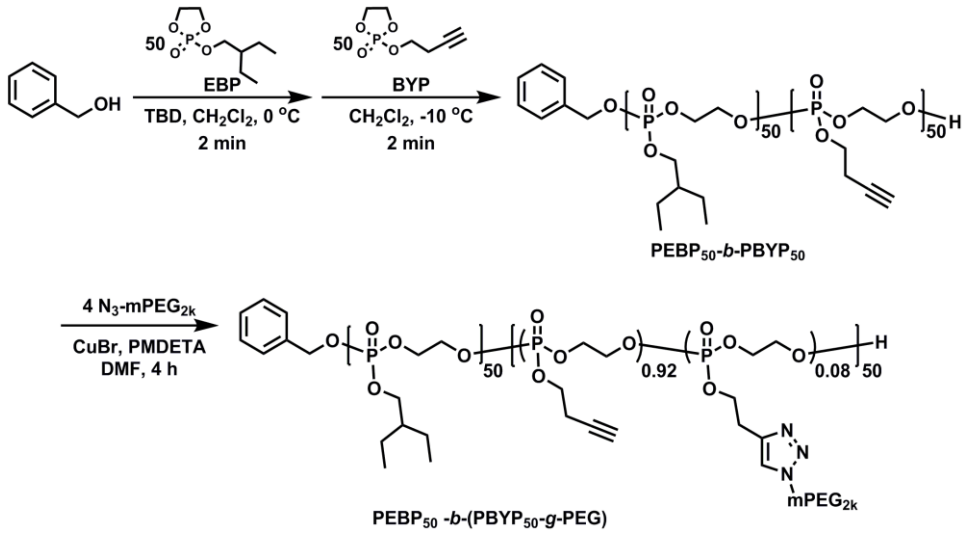

Figure 4.1. Synthesis of PEBP-*b*-PBYP-*g*-PEG *via* sequential ring-opening polymerizations of EBP and BYP, followed by PEGylation *via* CuAAC

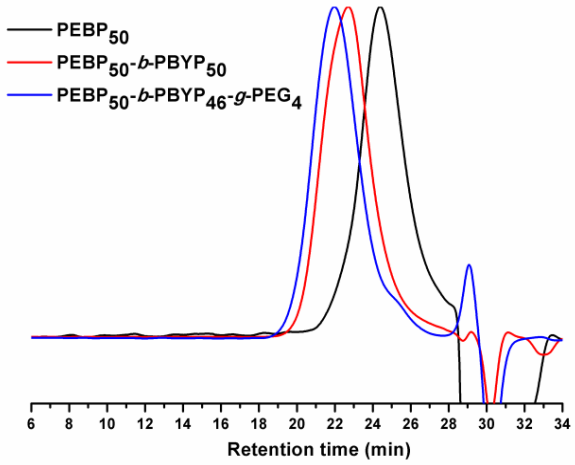

Figure 4.2. GPC traces of PEBP homopolymer (black line, PDI = 1.20), PEBP-*b*-PBYP diblock copolymer (red line, PDI = 1.25) and PEBP-*b*-PBYP-*g*-PEG terpolymer (blue line, PDI = 1.26).

Due to the water-soluble polyphosphoester backbone and densely-grafted mPEG, the amphiphilic block terpolymers could be directly dissolved in nanopure water at concentrations up to 120 mg/mL after 3 min sonication, during which they spontaneously formed micellar nanoparticles (Figure 4.3). These micelles were found to have a number-averaged hydrodynamic diameter of 11 ± 3 nm with monomodal size distribution and a low polymer dispersity of 0.25, as measured by dynamic light scattering (DLS) (Figure 4.4 a). The circular images observed by transmission electron microscopy (TEM) suggested that these nanoparticles were spherical with uniform sizes of 35 ± 4 nm (Figure 4.4 c). The significantly greater diameter by TEM *vs*. DLS also suggested that the particles deformed and flattened to a great extent upon deposition from solution and drying onto the carbon-coated copper grids for TEM imaging. Atomic force microscopy (AFM) was, therefore, conducted, and found to give an average height value measured as 0.82 nm,

confirming that deformation occurred upon deposition onto a mica substrate (Figure. 4.5 a, b). The flattening phenomenon observed by TEM and AFM could be attributed to the intrinsic low glass transition temperature (-52 ºC) of the polyphosphoester backbone.

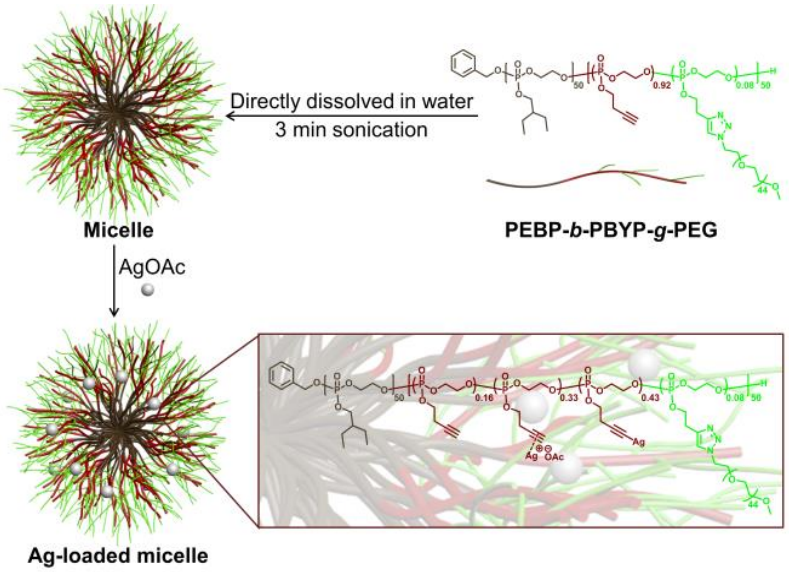

Figure 4.3. Schematic representation of micelle construction *via* self-assembly of the amphiphilic terpolymers in water, followed by loading with silver acetate (AgOAc).

Silver loading was subsequently performed after successful micellization, using silver acetate as the Ag^+ source to avoid potential inflammatory response from $AgNO_3$, which was used in the previous study (Figure 4.3).[193] The reaction mixture of micelles and silver acetate was stirred overnight to ensure maximum loading efficiency, followed by purification by passing through centrifugal filter devices (MWCO 100 kDa) several times (N>3) to remove unreacted silver acetate. The

actual loading was measured by inductively coupled plasma mass spectrometry (ICP-MS), using Rh as an internal standard. Different Ag feeding ratios were tested to optimize conditions with appropriate loading efficiency and loading amount (Figure 4.6). At feeding ratios below 1 (Ag^+ : alkyne), the loading amount increased approximately linearly, with only a slight drop in the loading efficiency, indicating reliability of the chemistry. A higher amount of silver loading was achieved with a maximum 15% loading (w/w), though much lower loading efficiency was observed as the feeding ratio continued to rise above 1. The feeding ratio of 1 was chosen for further characterization and biological evaluation, as it provided a good balance between loading amount and efficiency.

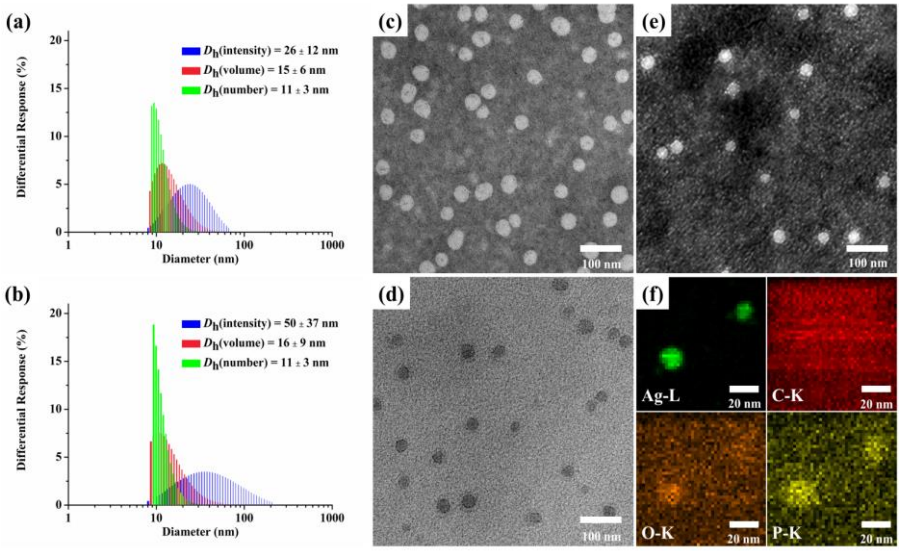

Figure 4.4. Characterization of nanoparticles. DLS histograms of intensity-averaged (D_h(intensity)), volume-averaged (D_h(volume)), number-averaged (D_h(number)) hydrodynamic diameters of (a) micelles, and (b) Ag-loaded micelles. Bright-field TEM images of (c) micelles, stained by uranyl acetate, and (d) Ag-loaded micelles. Dark-field

STEM image (e), and elemental mapping (f) of Ag-loaded micelles. The silver-loaded micelles were not stained in all samples.

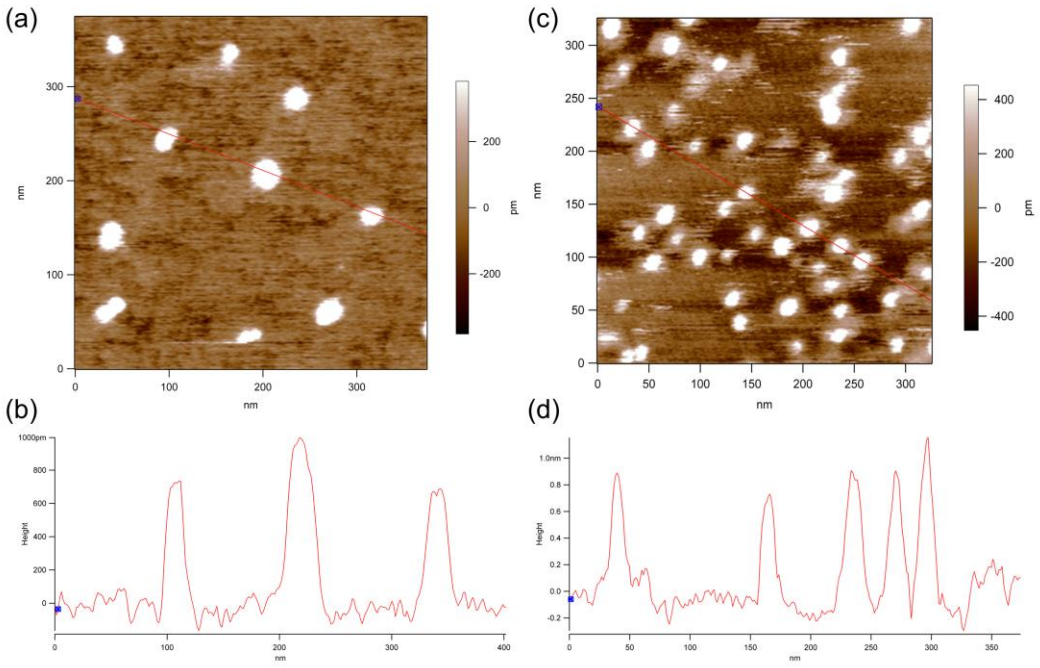

Figure 4.5. (a) Tapping mode AFM height image of empty micelles, and (b) height profile along the red line drawn in (a), (c) Tapping mode AFM height image of silver-loaded nanoparticles and (d) height profile along the red line drawn in (c).

The sizes and size distributions of these Ag-loaded micelles were also characterized by DLS and TEM. These data suggest that silver loading had minimal effect on the number-averaged hydrodynamic diameter of the micelles, with an average diameter remaining at *ca.* 11 nm. No staining of the Ag-loaded micelles is needed, since Ag is of high atomic number, which provides sufficient image contrast. Both bright-field TEM and high-angle annular dark-field imaging in the scanning TEM mode (HAADF-STEM) confirmed that well-defined silver-loaded nanoparticles were prepared, with relatively uniform dry-state substrate-adsorbed diameters of *ca.* 30 nm (Figure 4.4 d, e). As observed for the non-loaded micelles, comparisons of

TEM and AFM images indicated that these silver-loaded nanoparticles underwent severe deformation upon deposition and drying, giving AFM-measured height and diameter values of *ca.* 1.0 nm and *ca*. 30 nm, respectively, on a mica substrate (Figure 4.5 c, d). Elemental mapping was performed on the Ag-loaded nanoparticles using an energy-dispersive X-ray spectroscopy (EDS) detector in the STEM mode. The co-localization of silver, oxygen and phosphorous further demonstrated that silver was loaded into the polymeric matrix (Figure 4.4 f).

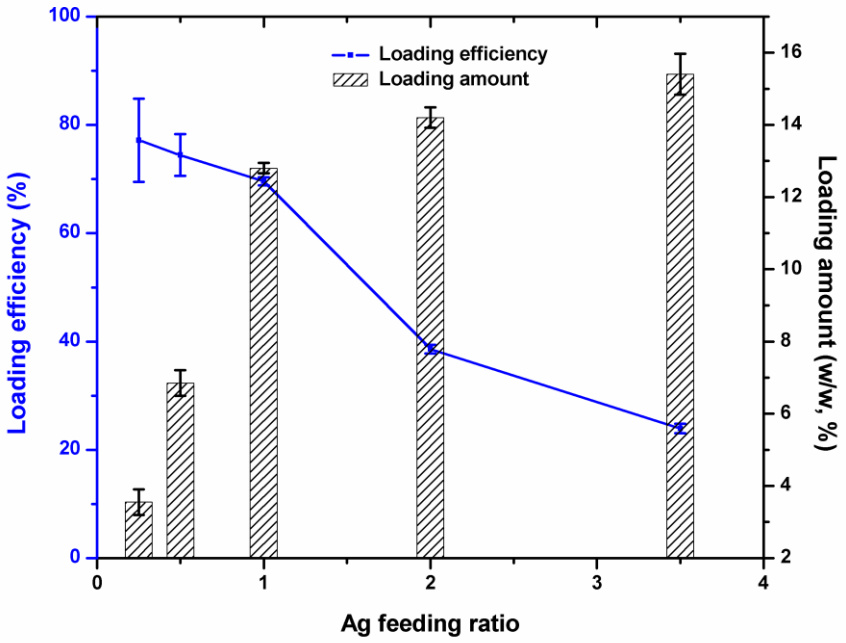

Figure 4.6. Optimization of loading efficiency (left, blue line) and loading amount (right, black hashed bars). The experiment was done in triplicate.

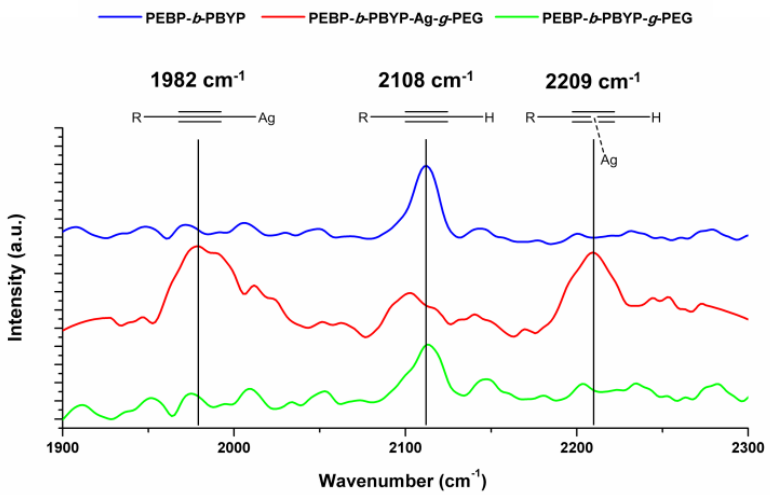

Figure 4.7. Raman spectroscopy of PEBP-*b*-PBYP (blue line), PEBP-*b*-PBYP-*g*-PEG (green line), and Ag-loaded micelles (PEBP-*b*-PBYP-Ag-*g*-PEG, feeding ratio = 1, red line).

The 1:1 silver-incubated sample was assessed by Raman spectroscopy to determine the extent and nature of silver-yne interactions (Fig. 5). Both the block copolymer PEBP-*b*-PBYP and block terpolymer PEBP-*b*-PBYP-*g*-PEG displayed only one peak in the region of 1900-2300 cm^{-1}, corresponding to the terminal alkyne groups present as side chain functionalities along one block of the polymer backbone.[198] In the case of silver-loaded nanoparticles, two additional peaks at 1982 and 2209 cm^{-1} were observed and were assigned to silver acetylide and Ag-alkyne complex, respectively.[198,202,203] An integrated signal intensity assessment of the number of subunits in each state, presuming comparable scattering cross-sections for each species, was performed, and revealed that *ca.* half of the alkyne functionalities were covalently bound to silver, with a third π-associated to silver, and that the remainder did not react.

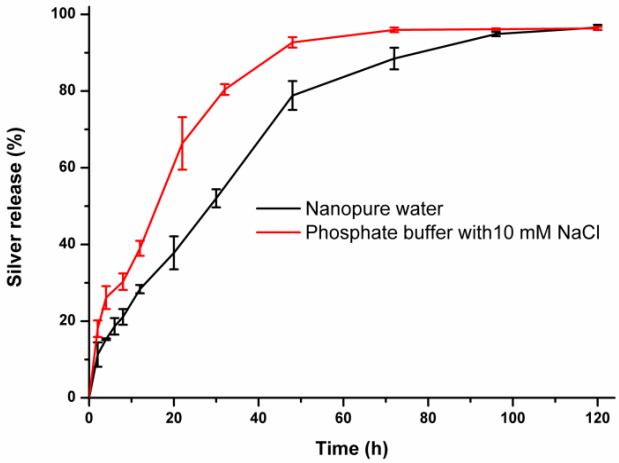

Figure 4.8. Release of Ag that was loaded into micelles at 37 ºC in nanopure water (black line) and 10 mM phosphate buffer with 10 mM NaCl, as measured by ICP-MS of aliquots collected from the cassettes over five days.

Release of silver from the nanoparticles was evaluated by monitoring the decrease of silver concentration inside dialysis cassettes at 37 ºC, analysed by ICP-MS (Fig. 6). It was found that silver was released in a sustained and controlled manner in nanopure water, with a release half-life $t_{1/2}$ of 28 h. The release was also conducted in 10 mM phosphate buffer containing 10 mM NaCl, to mimic the *in vivo* environment in patients with lung infection. As expected, the presence of NaCl significantly accelerated silver release due to the formation of AgCl, where the $t_{1/2}$ decreased from 28 h to 16 h. The sustained and controlled release of therapeutics may improve efficacy and reduce side effects. In addition, slow release kinetics allow a lower dosing frequency, which offers convenience to enhance patient adherence, as well as potential cost reduction. Furthermore, the silver-loaded

nanoparticles were stable in PBS for more than 2 days without visible precipitation, thus displaying the superior stability needed for *in vitro* and *in vivo* applications.

Table 4.1. MICs and MBCs of silver acetate and the silver-loaded micelles against cystic fibrosis pathogens. The MIC/MBCs were performed three times and the values reported represent the highest MIC/MBCs amongst the replicates. Concentration of silver-loaded micelles based on mass of silver.

Strains	MIC (µg/mL)		MBC (µg/mL)	
	AgOAc	Ag-NP	AgOAc	Ag-NP
P. aeruginosa				
PAO1	8	4	16	16
PAM57-15	8	4	16	16
PAHP3	8	4	16	16
S. aureus				
TCH1516	32	16	>256	>256
SALL06	32	16	>256	>256
SAEH05	16	8	64	16
Burkholderia sp.				
BG80	8	4	8	8
BM54	8	4	16	8

The antimicrobial potency of the silver-loaded nanoparticles was examined by broth micro dilution to determine the minimum inhibitory concentrations (MICs) and minimum bactericidal concentrations (MBCs) against cystic fibrosis-associated pathogens *Pseudomonas aeruginosa*, *Staphylococcus aureus*, and *Burkholderia sp.* (Table 4.1). Strains tested included a laboratory strain of *P. aeruginosa* (PAO1), USA300 *S. aureus* (TCH1516), and strains isolated from cystic fibrosis patients (PAM57-15, PAHP3, SALL06, SAEH05, BG80, and BM54). The MICs and MBCs of the silver nanoparticles were compared with silver acetate and generally showed

enhanced antimicrobial potency against these pathogens, with a reduction of MICs by 50% and similar MBCs. *P. aeruginosa* and *Burkholderia sp.* were more susceptible to silver than *S. aureus*, which was resistant to complete killing by silver in the case of TCH1516 and SALL06. The silver-loaded nanoparticles did show a remarkably higher potency against *S. aureus* strain SAEH05, which was not resistant to killing by silver. The increased antibacterial activities of silver-loaded nanoparticles over silver acetate might be ascribed to their increased stability in the aqueous environment and possibly superior association and/or uptake by the bacteria.[204] Furthermore, the silver-loaded nanoparticles displayed decreased toxicity compared with silver acetate, towards a cell line derived from human bronchial epithelial cells (16HBE), though it was not significantly different, as determined by nonparametric Student's t-test (Fig. S3). The increased antibacterial activities and decreased cytotoxicities towards human healthy cells demonstrated the advantages of using nanosized delivery systems for silver-based therapeutics *in vitro*, and suggest their great potential *in vivo*.

4.4 Conclusions

In summary, we have developed novel biocompatible and degradable polyphosphoester-based polymeric nanoparticles, which are capable of carrying silver cations *via* formation of silver acetylides with different coordination geometries, towards the treatment of lung infections associated with cystic fibrosis. The amphiphilic block terpolymer PEBP-*b*-PBYP-*g*-PEG was synthesized by "click-type" reactions, which are rapid, reliable and scalable. The amount of silver loaded

into the micelles was quantified by inductively coupled plasma-mass spectrometry (ICP-MS) using rhodium as an internal standard. It was found that up to 15% (w/w) loading could be achieved, consuming most of the pendant alkyne groups along the backbone. Raman spectroscopy of Ag-loaded micelles revealed that silver was loaded into the nanoparticles mainly by two coordination geometries at a molar feed ratio of 1:1 (alkyne : silver acetate). A combination of DLS, TEM and AFM indicated that the nanoscopic polymer assemblies were well-defined, having a hydrodynamic diameter of *ca*. 11 nm, and that they underwent significant flattening upon adsorption onto substrates. The co-localization of silver, oxygen and phosphorous, visualized by EDS elemental mapping, further confirmed that silver was loaded into the polymeric matrices. It was found that silver was released in a sustained and controlled manner over 5 days, with release half-life values of 28 h in nanopure water and 16 h in 10 mM phosphate buffer containing 10 mM NaCl. The superior stability of silver cations when loaded into the micelles has the potential to avoid the inactivation by anions and other biological compounds in the human body. Furthermore, these silver-loaded nanoparticles were measured to have higher antimicrobial activities with much lower MICs and similar MBCs against a series of cystic fibrosis pathogens and lower toxicities to human bronchial epithelial cells *in vitro*, as compared to the free drug (silver acetate), demonstrating advantageous features of this nanoscopic silver delivery platform. Evaluation of these silver-loaded nanoparticles as antimicrobial agents for lung infections *in vivo*, as well as determination of their *in vitro* and *in vivo* degradation profiles, are currently under

investigation.

CHAPTER V

CONCLUSIONS

Polymeric micelles are one of the most promising nanoscopic drug delivery platforms for the treatment of a wide range of diseases, including cancer and infectious diseases. Their characteristic core-shell morphology makes them especially suitable for packaging and protection of hydrophobic drugs in the core, while the hydrophilic shells provide water solubility and functionality for modifications, such as crosslinking, attachment of imaging agents and targeting ligands. The incorporation of crosslinks within the shells of polymeric micelles, to produce shell crosslinked knedel-like nanoparticles (SCKs), has been shown to provide for enhanced structural stability, better control with therapeutics release and alteration of their biological properties, while retaining the tunability of size and shape, and enhancing the ability to perform chemical modifications throughout the shell of the nanosized scaffold. In this dissertation, polymeric nanoparticles were designed and synthesized for the delivery of various therapeutic agents, including cisplatin & PTX for cancer therapy, and silver-based small molecules & other antibiotics for pulmonary infections, with a special attention on the effects of crosslinking on their *in vitro* and *in vivo* performance.

We first demonstrated the feasibility of incorporating CDDP into the shells of micelles and SCKs, which were self-assembled from non-degradable poly(acrylic acid)-*b*-polystyrene as a model system, by forming polymer-metal complexes. The drug loading decreased upon increasing the degree of crosslinking, with the micelles having

the highest drug loading percentage (48%, w/w). Nanosized particles with unimodal size distribution and low polydispersity indices were observed in all cases. The nanoparticles imparted significant physical stability to the incorporated drug and allowed control over its release from the polymeric particles. These CDDP-loaded nanoparticles exhibited cell-killing abilities *in vitro* that are comparable with reported micellar formulations. Crosslinking of polymeric micelles is often considered beneficial for improving stability against dilution. Here, Pt provides complexation-based crosslinks, and additional covalent crosslinks diminish sites for Pt complexation, giving lower cisplatin loading. Although cytotoxicity increased with covalent crosslinking, the lower drug loading counterbalanced the overall effect. In addition, upon incubating the micellar and crosslinked nanoparticles with the mouse macrophages, the crosslinked nanoparticles resulted in higher *in vitro* immunotoxicity. Therefore, any covalent crosslinking within future nanoparticle designs should be incorporated into an alternate region within the nanoparticle framework, to avoid consuming functionalities required for the drug complexation. Recently, we learnt the lessons above, and designed nanoscopic delivery vehicles comprised of degradable polyphosphoester-based polymers, where cisplatin was loaded into the core of these nanoparticles without additional covalent crosslinking (Appendix A).

Nanomaterials have great potential to offer effective treatment against devastating diseases by providing sustained release of high concentrations of therapeutic agents locally, especially when the route of administration allows for direct access to the diseased tissues. In Chapter III, we further investigated the effects of crosslinking of

polymeric micelles on their *in vitro* and *in vivo* performance, exploiting the biodegradable polyphosphoester-based polymeric micelles and SCKs, each derived from amphiphilic block-graft terpolymers, poly(2-ethylbutoxy phospholane)-*block*-poly(2-butynyl phospholane)-*graft*-poly(ethylene glycol) (PEBP-*b*-PBYP-*g*-PEG). It was found that high concentrations of PTX could be loaded into both micelles and SCKs, with well-defined morphology and uniform sizes. Encapsulation of 10 *wt*% PTX, into either micelles or SCKs, allowed for aqueous suspension of PTX at concentrations up to 4.8 mg/mL, as compared to < 2.0 μg/mL for the aqueous solubility of the drug alone. Drug release studies indicated that PTX release from these nanostructures was defined through a structure-function relationship, whereby the half-life of sustained PTX release was doubled through crosslinking of the micellar structure to form SCKs. These results demonstrated that crosslinking was capable of mediating PTX release by forming an additional physicochemical layer through the shell, the tuning of which could be utilized to further adjust the performance of these nanoscopic containers. Residual alkynyl groups along the backbones were modified by attaching the NIR dye IR800CW, enabling their use for *in vitro, in vivo* and *ex vivo* imaging-based studies.

We further investigated the *in vitro* and *in vivo* characteristics of both micelles and SCKs. *In vitro*, these micellar formulations had comparable cytotoxicities with the commercially available Taxol® mimicking formulation, further validating them as excellent candidates for translational studies. *In vivo* evaluation of the pharmacokinetics and biodistribution, following intratracheal delivery, revealed that crosslinking had the ability to control the rate of nanoparticle extravasation from the lungs. SCKs were

observed to be retained for almost twice the time of their micellar equivalents, *ca.* 8 days *vs*. 4 days respectively. These extravasation timelines appear to be reasonable for translational development when considering the repeating dosing schedules already in place for PTX chemotherapeutics. Interestingly, we have shown that the structure-function relationship of nanomaterials not only affects *in vitro* outcomes, but also has implications on *in vivo* performance and pharmacokinetics following intratracheal delivery to the lungs. More recently, we further optimized the formulation by PTX dual loading, where PTX was both chemically conjugated and physically loaded. The dual-loaded formulation could achieve a >15 mg/mL PTX total concentration in water (Appendix B).

In Chapter IV, we extended our degradable polyphosphoester-based nanoparticles, constructed from PEBP-*b*-PBYP-*g*-PEG, to deliver silver cations for the treatment of pulmonary infections. Silver cations were loaded to polymeric micelles *via* formation of silver acetylides with different coordination geometries. The amount of silver loaded into the micelles was quantified by inductively coupled plasma-mass spectrometry (ICP-MS) using rhodium as an internal standard. These systems displayed up to 15% (w/w) silver loading, consuming most of the pendant alkyne groups along the backbone. Raman spectroscopy of Ag-loaded micelles revealed that silver was loaded into the nanoparticles mainly by two coordination geometries at a molar feed ratio of 1:1 (alkyne : silver acetate). A combination of DLS, TEM and AFM characterization indicated that the nanoscopic polymer assemblies were well-defined, having a hydrodynamic diameter of *ca.* 11 nm, and that they underwent significant flattening upon adsorption onto

substrates. The co-localization of silver, oxygen and phosphorous, visualized by EDS elemental mapping, further confirmed the silver loading into the polymeric matrices. Silver-loaded nanoparticles was found to release their payload in a sustained and controlled manner over 5 days, with release half-life values of 28 h in nanopure water and 16 h in 10 mM phosphate buffer containing 10 mM NaCl. The superior stability of silver cations when loaded into the micelles has the potential to avoid the inactivation by anions and other biological compounds in the human body. Furthermore, these silver-loaded nanoparticles were measured to have higher antimicrobial activities against a series of cystic fibrosis pathogens and lower toxicities to human bronchial epithelial cells *in vitro*, as compared to the free drug (silver acetate), demonstrating advantageous features of this nanoscopic silver delivery platform. Evaluation of these silver-loaded nanoparticles as antimicrobial agents for lung infections *in vivo* in mice is currently under investigation. Combination delivery of silver and other antibiotics is also currently under investigation (Appendix C).

In summary, nanoscale drug delivery is a relative new, but fast growing field, which holds great promise for increased efficacy and reduced side effects of the incorporated therapeutic agents. In this dissertation, we have successfully loaded either hydrophilic drugs, such as silver cations and cisplatin, or hydrophobic paclitaxel into well-defined nanoparticles towards different lung diseases. These drugs were either physically entrapped or chemically conjugated to the nanocarriers. We have tested these formulations *in vitro* against relevant cancer cells or bacteria, and probed the *in vivo* biodistribution of the non-loaded nanoparticles in healthy animals to understand their

trafficking behaviors. However, some key issues remain to be investigated, for example the *in vivo* efficacy of the drug-loaded formulations, the relationships between *in vitro vs*. *in vivo* rates of degradation of the particles and release of their payloads, the independent trafficking globally and at the cellular level in diseased *vs*. healthy tissues, and the behaviors for each of the drug and carrier components, whether intact or in a fragmented form. Clearly, there is much chemistry and biology remaining to be understood, with this work being an important first step, providing initial information on the *in vivo* fate of polyphosphoester-based degradable nanoparticles.

REFERENCES

1. Feynman, R. P. *Eng. Sci.* **1960**, *23*, 22-36.
2. Freitas Jr, R. A. *Nanomedicine (N. Y., NY, U. S.)* **2005**, *1*, 2-9.
3. Wagner, V.; Dullaart, A.; Bock, A.-K.; Zweck, A. *Nat. Biotechnol.* **2006**, *24*, 1211-1217.
4. Lee, K. S.; Chung, H. C.; Im, S. A.; Park, Y. H.; Kim, C. S.; Kim, S. B.; Rha, S. Y.; Lee, M. Y.; Ro, J. *Breast Cancer Res. Treat.* **2008**, *108*, 241-250.
5. Tian, J.; Stella, V. J. *J. Pharm. Sci.* **2008**, *97*, 3100-3108.
6. Zhang, X. Q.; Xu, X.; Bertrand, N.; Pridgen, E.; Swami, A.; Farokhzad, O. C. *Adv. Drug Delivery Rev.* **2012**, *64*, 1363-1384.
7. Charrois, G. J. R.; Allen, T. M. *Biochim. Biophys. Acta, Biomembr.* **2004**, *1663*, 167-177.
8. Kelsen, D. P.; Alcock, N.; Young, C. W. *Am. J. Clin. Oncol.* **1985**, *8*, 77-80.
9. Campbell, A. B.; Kalman, S. M.; Jacobs, C. *Cancer Treat. Rep.* **1983**, *67*, 169-172.
10. Baba, M.; Matsumoto, Y.; Kashio, A.; Cabral, H.; Nishiyama, N.; Kataoka, K.; Yamasoba, T. *J. Controlled Release* **2012**, *157*, 112-117.
11. Uchino, H.; Matsumura, Y.; Negishi, T.; Koizumi, F.; Hayashi, T.; Honda, T.; Nishiyama, N.; Kataoka, K.; Naito, S.; Kakizoe, T. *Br. J. Cancer* **2005**, *93*, 678-687.
12. Wicki, A.; Witzigmann, D.; Balasubramanian, V.; Huwyler, J. *J. Controlled Release* **2015**, *200*, 138-157.
13. Grull, H.; Langereis, S. *J. Controlled Release* **2012**, *161*, 317-327.

14. Zhang, Z.; Chen, S. F.; Jiang, S. Y. *Biomacromolecules* **2006**, *7*, 3311-3315.

15. Li, A.; Luehmann, H. P.; Sun, G.; Samarajeewa, S.; Zou, J.; Zhang, S.; Zhang, F.; Welch, M. J.; Liu, Y.; Wooley, K. L. *ACS Nano* **2012**, *6*, 8970-8982.

16. Elsabahy, M.; Wooley, K. L. *Chem. Soc. Rev.* **2012**, *41*, 2545-2561.

17. Vonarbourg, A.; Passirani, C.; Saulnier, P.; Benoit, J. P. *Biomaterials* **2006**, *27*, 4356-4373.

18. Moghimi, S. M.; Hunter, A. C.; Murray, J. C. *Pharmacol. Rev.* **2001**, *53*, 283-318.

19. Lammers, T.; Kiessling, F.; Hennink, W. E.; Storm, G. *J. Controlled Release* **2012**, *161*, 175-187.

20. Maeda, H.; Wu, J.; Sawa, T.; Matsumura, Y.; Hori, K. *J. Controlled Release* **2000**, *65*, 271-284.

21. Matsumura, Y.; Maeda, H. *Cancer Res.* **1986**, *46*, 6387-6392.

22. Fang, J.; Nakamura, H.; Maeda, H. *Adv. Drug Delivery Rev.* **2011**, *63*, 136-151.

23. Sudimack, J.; Lee, R. J. *Adv. Drug Delivery Rev.* **2000**, *41*, 147-162.

24. Lee, R. J.; Low, P. S. *Biochim. Biophys. Acta, Biomembr.* **1995**, *1233*, 134-144.

25. Farokhzad, O. C.; Langer, R. *ACS Nano* **2009**, *3*, 16-20.

26. Sanson, C.; Schatz, C.; Le Meins, J. F.; Soum, A.; Thevenot, J.; Garanger, E.; Lecommandoux, S. *J. Controlled Release* **2010**, *147*, 428-435.

27. Rodriguez, M. A.; Pytlik, R.; Kozak, T.; Chhanabhai, M.; Gascoyne, R.; Lu, B.; Deitcher, S. R.; Winter, J. N.; Investigators, M. *Cancer* **2009**, *115*, 3475-3482.

28. Barenholz, Y. *J. Controlled Release* **2012**, *160*, 117-134.

29. Slingerland, M.; Guchelaar, H. J.; Rosing, H.; Scheulen, M. E.; van Warmerdam, L. J. C.; Beijnen, J. H.; Gelderblom, H. *Clin. Ther.* **2013**, *35*, 1946-1954.

30. Kato, K.; Chin, K.; Yoshikawa, T.; Yamaguchi, K.; Tsuji, Y.; Esaki, T.; Sakai, K.; Kimura, M.; Hamaguchi, T.; Shimada, Y.; Matsumura, Y.; Ikeda, R. *Invest. New Drugs* **2012**, *30*, 1621-1627.

31. Kataoka, K.; Harada, A.; Nagasaki, Y. *Adv. Drug Delivery Rev.* **2001**, *47*, 113-131.

32. Zhang, F. W.; Zhang, S. Y.; Pollack, S. F.; Li, R. C.; Gonzalez, A. M.; Fan, J. W.; Zou, J.; Leininger, S. E.; Pavia-Sanders, A.; Johnson, R.; Nelson, L. D.; Raymond, J. E.; Elsabahy, M.; Hughes, D. M. P.; Lenox, M. W.; Gustafson, T. P.; Wooley, K. L. *J. Am. Chem. Soc.* **2015**, *137*, 2056-2066.

33. Hamaguchi, T.; Doi, T.; Eguchi-Nakajima, T.; Kato, K.; Yamada, Y.; Shimada, Y.; Fuse, N.; Ohtsu, A.; Matsumoto, S.; Takanashi, M.; Matsumura, Y. *Clin. Cancer Res.* **2010**, *16*, 5058-5066.

34. Kim, S. C.; Kim, D. W.; Shim, Y. H.; Bang, J. S.; Oh, H. S.; Kim, S. W.; Seo, M. H. *J. Controlled Release* **2001**, *72*, 191-202.

35. Shah, P. N.; Lin, L. Y.; Smolen, J. A.; Tagaev, J. A.; Gunsten, S. P.; Han, D. S.; Heo, G. S.; Li, Y.; Zhang, F.; Zhang, S.; Wright, B. D.; Panzner, M. J.; Youngs, W. J.; Brody, S. L.; Wooley, K. L.; Cannon, C. L. *ACS Nano* **2013**, *7*, 4977-4987.

36. Zhang, F.; Elsabahy, M.; Zhang, S.; Lin, L. Y.; Zou, J.; Wooley, K. L. *Nanoscale* **2013**, *5*, 3220-3225.

37. Zhang, F. W.; Smolen, J. A.; Zhang, S. Y.; Li, R. C.; Shah, P. N.; Cho, S. H.; Wang, H.; Raymond, J. E.; Cannon, C. L.; Wooley, K. L. *Nanoscale* **2015**, *7*, 2265-2270.

38. Cui, H. G.; Chen, Z. Y.; Zhong, S.; Wooley, K. L.; Pochan, D. J. *Science* **2007**, *317*, 647-650.

39. Li, Z.; Ma, J.; Lee, N. S.; Wooley, K. L. *J. Am. Chem. Soc.* **2011**, *133*, 1228-1231.

40. Zhu, J. H.; Zhang, S. Y.; Zhang, F. W.; Wooley, K. L.; Pochan, D. J. *Adv. Funct. Mater.* **2013**, *23*, 1767-1773.

41. Lee, N. S.; Lin, L. Y.; Neumann, W. L.; Freskos, J. N.; Karwa, A.; Shieh, J. J.; Dorshow, R. B.; Wooley, K. L. *Small* **2011**, *7*, 1998-2003.

42. Thurmond, K. B.; Kowalewski, T.; Wooley, K. L. *J. Am. Chem. Soc.* **1996**, *118*, 7239-7240.

43. Joralemon, M. J.; O'Reilly, R. K.; Hawker, C. J.; Wooley, K. L. *J. Am. Chem. Soc.* **2005**, *127*, 16892-16899.

44. Wooley, K. L. *J. Polym. Sci., Part A: Polym. Chem.* **2000**, *38*, 1397-1407.

45. Lin, L. Y.; Lee, N. S.; Zhu, J. H.; Nystrom, A. M.; Pochan, D. J.; Dorshow, R. B.; Wooley, K. L. *J. Controlled Release* **2011**, *157*, 500-500.

46. Zhang, S. Y.; Li, Z.; Samarajeewa, S.; Sun, G. R.; Yang, C.; Wooley, K. L. *J. Am. Chem. Soc.* **2011**, *133*, 11046-11049.

47. Sun, G.; Hagooly, A.; Xu, J.; Nystrom, A. M.; Li, Z.; Rossin, R.; Moore, D. A.; Wooley, K. L.; Welch, M. J. *Biomacromolecules* **2008**, *9*, 1997-2006.

48. Pochan, D. J.; Chen, Z. Y.; Cui, H. G.; Hales, K.; Qi, K.; Wooley, K. L. *Science* **2004**, *306*, 94-97.

49. Lee, N. S.; Sun, G. R.; Lin, L. Y.; Neumann, W. L.; Freskos, J. N.; Karwa, A.; Shieh, J. J.; Dorshow, R. B.; Wooley, K. L. *J. Mater. Chem.* **2011**, *21*, 14193-14202.

50. Samarajeewa, S.; Shrestha, R.; Elsabahy, M.; Karwa, A.; Li, A.; Zentay, R. P.; Kostelc, J. G.; Dorshow, R. B.; Wooley, K. L. *Mol. Pharmaceutics* **2013**, *10*, 1092-1099.

51. Liu, J. Q.; Zhang, Q.; Remsen, E. E.; Wooley, K. L. *Biomacromolecules* **2001**, *2*, 362-368.

52. Tian, H. Y.; Tang, Z. H.; Zhuang, X. L.; Chen, X. S.; Jing, X. B. *Prog. Polym. Sci.* **2012**, *37*, 237-280.

53. Bertrand, N.; Leroux, J. C. *J. Controlled Release* **2012**, *161*, 152-163.

54. Shin, H. C.; Alani, A. W. G.; Cho, H.; Bae, Y.; Kolesar, J. M.; Kwon, G. S. *Mol. Pharmaceutics* **2011**, *8*, 1257-1265.

55. Chen, C. K.; Jones, C. H.; Mistriotis, P.; Yu, Y.; Ma, X.; Ravikrishnan, A.; Jiang, M.; Andreadis, S. T.; Pfeifer, B. A.; Cheng, C. *Biomaterials* **2013**, *34*, 9688-9699.

56. Deming, T. J. *Nature* **1997**, *390*, 386-389.

57. He, X.; Fan, J.; Zhang, F.; Li, R.; Pollack, K. A.; Raymond, J. E.; Zou, J.; Wooley, K. L. *J. Mater. Chem. B* **2014**, *2*, 8123-8130.

58. Gustafson, T. P.; Lonnecker, A. T.; Heo, G. S.; Zhang, S.; Dove, A. P.; Wooley, K. L. *Biomacromolecules* **2013**, *14*, 3346-3353.

59. Azechi, M.; Matsumoto, K.; Endo, T. *J. Polym. Sci., Part A: Polym. Chem.* **2013**, *51*, 1651-1655.

60. Chen, X.; Gross, R. A. *Macromolecules* **1998**, *32*, 308-314.

61. Zhang, S.; Zou, J.; Zhang, F.; Elsabahy, M.; Felder, S. E.; Zhu, J.; Pochan, D. J.; Wooley, K. L. *J. Am. Chem. Soc.* **2012**, *134*, 18467-18474.

62. Sun, C. Y.; Dou, S.; Du, J. Z.; Yang, X. Z.; Li, Y. P.; Wang, J. *Adv. Healthcare Mater.* **2014**, *3*, 261-272.

63. Zhai, X.; Huang, W.; Liu, J.; Pang, Y.; Zhu, X.; Zhou, Y.; Yan, D. *Macromol. Biosci.* **2011**, *11*, 1603-1610.

64. Sy, J. C.; Seshadri, G.; Yang, S. C.; Brown, M.; Oh, T.; Dikalov, S.; Murthy, N.; Davis, M. E. *Nat. Mater.* **2008**, *7*, 863-869.

65. Grad, S.; Kupcsik, L.; Gorna, K.; Gogolewski, S.; Alini, M. *Biomaterials* **2003**, *24*, 5163-5171.

66. Zou, J.; Zhang, F.; Zhang, S.; Pollack, S. F.; Elsabahy, M.; Fan, J.; Wooley, K. L. *Adv. Healthcare Mater.* **2014**, *3*, 441-448.

67. Liu, J.; Huang, W.; Pang, Y.; Zhu, X.; Zhou, Y.; Yan, D. *Biomacromolecules* **2010**, *11*, 1564-1570.

68. Sun, T. M.; Du, J. Z.; Yan, L. F.; Mao, H. Q.; Wang, J. *Biomaterials* **2008**, *29*, 4348-4355.

69. Wen, J.; Mao, H. Q.; Li, W. P.; Lin, K. Y.; Leong, K. W. *J. Pharm. Sci.* **2004**, *93*, 2142-2157.

70. Yang, X. Z.; Sun, T. M.; Dou, S.; Wu, J.; Wang, Y. C.; Wang, J. *Biomacromolecules* **2009**, *10*, 2213-2220.

71. Wan, A. C.; Mao, H. Q.; Wang, S.; Phua, S. H.; Lee, G. P.; Pan, J.; Lu, S.; Wang, J.; Leong, K. W. *J. Biomed. Mater. Res., Part B* **2004**, *70*, 91-102.

72. Huang, S. W.; Wang, J.; Zhang, P. C.; Mao, H. Q.; Zhuo, R. X.; Leong, K. W. *Biomacromolecules* **2004**, *5*, 306-311.

73. Wang, Y. C.; Yuan, Y. Y.; Du, J. Z.; Yang, X. Z.; Wang, J. *Macromol. Biosci.* **2009**, *9*, 1154-1164.

74. Zhao, Z.; Wang, J.; Mao, H. Q.; Leong, K. W. *Adv. Drug Delivery Rev.* **2003**, *55*, 483-499.

75. Ferlay, J.; Soerjomataram, I.; Dikshit, R.; Eser, S.; Mathers, C.; Rebelo, M.; Parkin, D. M.; Forman, D.; Bray, F. *Int. J. Cancer* **2015**, *136*, E359-E386.

76. *World Health Organization* **2015**, http://www.who.int/mediacentre/factsheets/fs310/en/ (accessed April 3, 2015).

77. Meyers, P. A.; Schwartz, C. L.; Krailo, M. D.; Healey, J. H.; Bernstein, M. L.; Betcher, D.; Ferguson, W. S.; Gebhardt, M. C.; Goorin, A. M.; Harris, M.; Kleinerman, E.; Link, M. P.; Nadel, H.; Nieder, M.; Siegal, G. P.; Weiner, M. A.; Wells, R. J.; Womer, R. B.; Grier, H. E. *J. Clin. Oncol.* **2008**, *26*, 633-638.

78. Ottaviani, G.; Jaffe, N. *Cancer Treat. Res.* **2009**, *152*, 3-13.

79. Ferguson, W. S.; Goorin, A. M. *Cancer Invest.* **2001**, *19*, 292-315.

80. Provisor, A. J.; Ettinger, L. J.; Nachman, J. B.; Krailo, M. D.; Makley, J. T.; Yunis, E. J.; Huvos, A. G.; Betcher, D. L.; Baum, E. S.; Kisker, C. T.; Miser, J. S. *J. Clin. Oncol.* **1997**, *15*, 76-84.

81. Bielack, S. S.; Kempf-Bielack, B.; Branscheid, D.; Carrle, D.; Friedel, G.; Helmke, K.; Kevric, M.; Jundt, G.; Kuhne, T.; Maas, R.; Schwarz, R.; Zoubek, A.; Jurgens, H. *J. Clin. Oncol.* **2009**, *27*, 557-565.

82. Kempf-Bielack, B.; Bielack, S. S.; Jurgens, H.; Branscheid, D.; Berdel, W. E.; Exner, G. U.; Gobel, U.; Helmke, K.; Jundt, G.; Kabisch, H.; Kevric, M.; Klingebiel, T.; Kotz, R.; Maas, R.; Schwarz, R.; Semik, M.; Treuner, J.; Zoubek, A.; Winkler, K. *J. Clin. Oncol.* **2005**, *23*, 559-568.

83. Hughes, D. P. *Curr. Opin. Oncol.* **2009**, *21*, 332-337.

84. Cutting, G. R. *Nat. Rev. Genet.* **2015**, *16*, 45-56.

85. Riordan, J. R.; Rommens, J. M.; Kerem, B. S.; Alon, N.; Rozmahel, R.; Grzelczak, Z.; Zielenski, J.; Lok, S.; Plavsic, N.; Chou, J. L.; Drumm, M. L.; Iannuzzi, M. C.; Collins, F. S.; Tsui, L. C. *Science* **1989**, *245*, 1066-1072.

86. Boucher, H. W.; Talbot, G. H.; Bradley, J. S.; Edwards, J. E.; Gilbert, D.; Rice, L. B.; Scheld, M.; Spellberg, B.; Bartlett, J. *Clin. Infect. Dis.* **2009**, *48*, 1-12.

87. Rice, L. B. *J. Infect. Dis.* **2008**, *197*, 1079-1081.

88. Lau, G. W.; Ran, H. M.; Kong, F. S.; Hassett, D. J.; Mavrodi, D. *Infect. Immun.* **2004**, *72*, 4275-4278.

89. Laxminarayan, R.; Duse, A.; Wattal, C.; Zaidi, A. K. M.; Wertheim, H. F. L.; Sumpradit, N.; Vlieghe, E.; Hara, G. L.; Gould, I. M.; Goossens, H.; Greko, C.; So, A. D.; Bigdeli, M.; Tomson, G.; Woodhouse, W.; Ombaka, E.; Peralta, A. Q.; Qamar, F. N.; Mir, F.; Kariuki, S.; Bhutta, Z. A.; Coates, A.; Bergstrom, R.; Wright, G. D.; Brown, E. D.; Cars, O. *Lancet Infect. Dis.* **2013**, *13*, 1057-1098.

90. Roemer, T.; Boone, C. *Nat. Chem. Biol.* **2013**, *9*, 222-231.

91. Weers, J. *Adv. Drug Delivery Rev.* **2015**, *85*, 24-43.

92. Sung, J. C.; Pulliam, B. L.; Edwards, D. A. *Trends Biotechnol.* **2007**, *25*, 563-570.

93. Sermet-Gaudelus, I.; Le Cocguic, Y.; Ferroni, A.; Clairicia, M.; Barthe, J.; Delaunay, J. P.; Brousse, V.; Lenoir, G. *Paediatr. Drugs* **2002**, *4*, 455-467.

94. Labiris, N. R.; Dolovich, M. B. *Br. J. Clin. Pharmacol.* **2003**, *56*, 588-599.

95. Jia, S. F.; Worth, L. L.; Turan, M.; Duan Xp, X. P.; Kleinerman, E. S. *Anti-Cancer Drugs* **2002**, *13*, 155-161.

96. Koshkina, N. V.; Kleinerman, E. S.; Waidrep, C.; Jia, S. F.; Worth, L. L.; Gilbert, B. E.; Knight, V. *Clin. Cancer Res.* **2000**, *6*, 2876-2880.

97. Videira, M.; Almeida, A. J.; Fabra, A. *Nanomedicine (N. Y., NY, U. S.)* **2012**, *8*, 1208-1215.

98. Zhang, S. Y.; Wang, H.; Shen, Y. F.; Zhang, F. W.; Seetho, K.; Zou, J.; Taylor, J. S. A.; Dove, A. P.; Wooley, K. L. *Macromolecules* **2013**, *46*, 5141-5149.

99. Shen, Y.; Zhang, S.; Zhang, F.; Loftis, A.; Pavia-Sanders, A.; Zou, J.; Fan, J.; Taylor, J. S.; Wooley, K. L. *Adv. Mater.* **2013**, *25*, 5609-5614.

100. Elsabahy, M.; Zhang, S.; Zhang, F.; Deng, Z. J.; Lim, Y. H.; Wang, H.; Parsamian, P.; Hammond, P. T.; Wooley, K. L. *Sci. Rep.* **2013**, *3*, 3313.

101. Lim, Y. H.; Tiemann, K. M.; Heo, G. S.; Wagers, P. O.; Rezenom, Y. H.; Zhang, S. Y.; Zhang, F. W.; Youngs, W. J.; Hunstad, D. A.; Wooley, K. L. *ACS Nano* **2015**, *9*, 1995-2008.

102. Zou, J.; Zhang, F. W.; Chen, Y. C.; Raymond, J. E.; Zhang, S. Y.; Fan, J. W.; Zhu, J. H.; Li, A.; Seetho, K.; He, X.; Pochan, D. J.; Wooley, K. L. *Soft Matter* **2013**, *9*, 5951-5958.

103. Fan, J. W.; Li, R. C.; He, X.; Seetho, K.; Zhang, F. W.; Zou, J.; Wooley, K. L. *Poly. Chem.* **2014**, *5*, 3977-3981.

104. Fan, J. W.; Zou, J.; He, X.; Zhang, F. W.; Zhang, S. Y.; Raymond, J. E.; Wooley, K. L. *Chem. Sci.* **2014**, *5*, 141-150.

105. Elsabahy, M.; Li, A.; Zhang, F. W.; Sultan, D.; Liu, Y. J.; Wooley, K. L. *J. Controlled Release* **2013**, *172*, 641-652.

106. Rosenberg, B. *Interdiscip. Sci. Rev.* **1978**, *3*, 134-147.

107. Kelland, L. *Nat. Rev. Cancer* **2007**, *7*, 573-584.

108. Gillies, E. R.; Frechet, J. M. J. *Drug Discov. Today* **2005**, *10*, 35-43.

109. Nishiyama, N.; Okazaki, S.; Cabral, H.; Miyamoto, M.; Kato, Y.; Sugiyama, Y.; Nishio, K.; Matsumura, Y.; Kataoka, K. *Cancer Res.* **2003**, *63*, 8977-8983.

110. Jin, W.; Xu, P.; Zhan, Y.; Shen, Y.; Van Kirk, E. A.; Alexander, B.; Murdoch, W. J.; Liu, L.; Isaak, D. D. *Drug Delivery* **2007**, *14*, 279-286.

111. Hirai, M.; Minematsu, H.; Hiramatsu, Y.; Kitagawa, H.; Otani, T.; Iwashita, S.; Kudoh, T.; Chen, L.; Li, Y.; Okada, M.; Salomon, D. S.; Igarashi, K.; Chikuma, M.; Seno, M. *Int. J. Pharm.* **2010**, *391*, 274-283.

112. Duan, S. F.; Cai, S.; Xie, Y. M.; Bagby, T.; Ren, S. Q.; Forrest, M. L. *J. Polym. Sci., Part A: Polym. Chem.* **2012**, *50*, 2715-2724.

113. Paraskar, A. S.; Soni, S.; Chin, K. T.; Chaudhuri, P.; Muto, K. W.; Berkowitz, J.; Handlogten, M. W.; Alves, N. J.; Bilgicer, B.; Dinulescu, D. M.; Mashelkar, R. A.; Sengupta, S. *Proc. Natl. Acad. Sci. U. S. A.* **2010**, *107*, 12435-12440.

114. Haxton, K. J.; Burt, H. M. *J. Pharm. Sci.* **2009**, *98*, 2299-2316.

115. Oberoi, H. S.; Laquer, F. C.; Marky, L. A.; Kabanov, A. V.; Bronich, T. K. *J. Controlled Release* **2011**, *153*, 64-72.

116. Huynh, V. T.; de Souza, P.; Stenzel, M. H. *Macromolecules* **2011**, *44*, 7888-7900.

117. Huynh, V. T.; Chen, G.; de Souza, P.; Stenzel, M. H. *Biomacromolecules* **2011**, *12*, 1738-1751.

118. Jadhav, V. B.; Jun, Y. J.; Song, J. H.; Park, M. K.; Oh, J. H.; Chae, S. W.; Kim, I. S.; Choi, S. J.; Lee, H. J.; Sohn, Y. S. *J. Controlled Release* **2010**, *147*, 144-150.

119. Elsabahy, M.; Wooley, K. L. *J. Polym. Sci., Part A: Polym. Chem.* **2012**, *50*, 1869-1880.

120. Lin, L. Y.; Karwa, A.; Kostelc, J. G.; Lee, N. S.; Dorshow, R. B.; Wooley, K. L. *Mol. Pharmaceutics* **2012**, *9*, 2248-2255.

121. Boyer, C.; Stenzel, M. H.; Davis, T. P. *J. Polym. Sci., Part A: Polym. Chem.* **2011**, *49*, 551-595.

122. Ha, H.-W.; Kim, I. Y.; Hwang, S.-J.; Ruoff, R. S. *Electrochem. Solid-State Lett.* **2011**, *14*, B70-B73.

123. Wang, C.; Yin, L.; Zhang, L.; Liu, N.; Lun, N.; Qi, Y. *ACS Appl. Mater. Interfaces* **2010**, *2*, 3373-3377.

124. Cheong, S.; Watt, J.; Ingham, B.; Toney, M. F.; Tilley, R. D. *J. Am. Chem. Soc.* **2009**, *131*, 14590-14595.

125. Lee, S. M.; O'Halloran, T. V.; Nguyen, S. T. *J. Am. Chem. Soc.* **2010**, *132*, 17130-17138.

126. Shrestha, R.; Elsabahy, M.; Florez-Malaver, S.; Samarajeewa, S.; Wooley, K. L. *Biomaterials* **2012**, *33*, 8557-8568.

127. Sun, G. R.; Lee, N. S.; Neumann, W. L.; Freskos, J. N.; Shieh, J. J.; Dorshow, R. B.; Wooley, K. L. *Soft Matter* **2009**, *5*, 3422-3429.

128. Dhar, S.; Kolishetti, N.; Lippard, S. J.; Farokhzad, O. C. *Proc. Natl. Acad. Sci. U. S. A.* **2011**, *108*, 1850-1855.

129. Torchilin, V. *Adv. Drug Delivery Rev.* **2011**, *63*, 131-135.

130. Pan, D.; Turner, J. L.; Wooley, K. L. *Chem. Commun.* **2003**, 2400-2401.

131. Stordal, B.; Pavlakis, N.; Davey, R. *Cancer Treatment Rev.* **2007**, *33*, 688-703.

132. Wei, L.; Cai, C.; Lin, J.; Chen, T. *Biomaterials* **2009**, *30*, 2606-2613.

133. Sparreboom, A.; Scripture, C. D.; Trieu, V.; Williams, P. J.; De, T.; Yang, A.; Beals, B.; Figg, W. D.; Hawkins, M.; Desai, N. *Clin. Cancer Res.* **2005**, *11*, 4136-4143.

134. Gautam, A.; Koshkina, N. *Curr. Cancer Drug Targets* **2003**, *3*, 287-296.

135. Singla, A. K.; Garg, A.; Aggarwal, D. *Int. J. Pharm.* **2002**, *235*, 179-192.

136. Rowinsky, E. K.; Donehower, R. C. *N. Engl. J. Med.* **1995**, *332*, 1004-1014.

137. Brannon-Peppas, L.; Blanchette, J. O. *Adv. Drug Delivery Rev.* **2004**, *56*, 1649-1659.

138. Rowinsky, E. K.; Chaudhry, V.; Cornblath, D. R.; Donehower, R. C. *J. Natl. Cancer Inst. Monogr.* **1993**, 107-115.

139. Gelderblom, H.; Verweij, J.; Nooter, K.; Sparreboom, A. *Eur. J. Cancer* **2001**, *37*, 1590-1598.

140. Wang, J.; Liu, W.; Tu, Q.; Wang, J.; Song, N.; Zhang, Y.; Nie, N.; Wang, J. *Biomacromolecules* **2011**, *12*, 228-234.

141. Miele, E.; Spinelli, G. P.; Miele, E.; Tomao, F.; Tomao, S. *Int. J. Nanomedicine* **2009**, *4*, 99-105.

142. Hamaguchi, T.; Matsumura, Y.; Suzuki, M.; Shimizu, K.; Goda, R.; Nakamura, I.; Nakatomi, I.; Yokoyama, M.; Kataoka, K.; Kakizoe, T. *Br. J. Cancer* **2005**, *92*, 1240-1246.

143. Wang, A. Z.; Langer, R.; Farokhzad, O. C. *Annu. Rev. Med.* **2012**, *63*, 185-198.

144. Kratz, F. *J. Controlled Release* **2008**, *132*, 171-183.

145. Green, M. R.; Manikhas, G. M.; Orlov, S.; Afanasyev, B.; Makhson, A. M.; Bhar, P.; Hawkins, M. J. *Ann. Oncol.* **2006**, *17*, 1263-1268.

146. Ko, Y. J.; Canil, C. M.; Mukherjee, S. D.; Winquist, E.; Elser, C.; Eisen, A.; Reaume, M. N.; Zhang, L. Y.; Sridhar, S. S. *Lancet Oncol.* **2013**, *14*, 769-776.

147. Zhang, S.; Zou, J.; Elsabahy, M.; Karwa, A.; Li, A.; Moore, D. A.; Dorshow, R. B.; Wooley, K. L. *Chem. Sci.* **2013**, *4*, 2122-2126.

148. Teow, H. M.; Zhou, Z.; Najlah, M.; Yusof, S. R.; Abbott, N. J.; D'Emanuele, A. *Int. J. Pharm.* **2013**, *441*, 701-711.

149. Murphy, E. A.; Majeti, B. K.; Mukthavaram, R.; Acevedo, L. M.; Barnes, L. A.; Cheresh, D. A. *Mol. Cancer Ther.* **2011**, *10*, 972-982.

150. Yu, Y.; Chen, C. K.; Law, W. C.; Mok, J.; Zou, J.; Prasad, P. N.; Cheng, C. *Mol. Pharmaceutics* **2013**, *10*, 867-874.

151. Liao, L.; Liu, J.; Dreaden, E. C.; Morton, S. W.; Shopsowitz, K. E.; Hammond, P. T.; Johnson, J. A. *J. Am. Chem. Soc.* **2014**, *136*, 5896-5899.

152. Schmitt-Sody, M.; Strieth, S.; Krasnici, S.; Sauer, B.; Schulze, B.; Teifel, M.; Michaelis, U.; Naujoks, K.; Dellian, M. *Clin. Cancer Res.* **2003**, *9*, 2335-2341.

153. Liang, K.; Richardson, J. J.; Ejima, H.; Such, G. K.; Cui, J.; Caruso, F. *Adv. Mater.* **2014**, *26*, 2398-2402.

154. Yu, Y.; Chen, C. K.; Law, W. C.; Weinheimer, E.; Sengupta, S.; Prasad, P. N.; Cheng, C. *Biomacromolecules* **2014**, *15*, 524-532.

155. Meng, L.; Huang, W.; Wang, D.; Huang, X.; Zhu, X.; Yan, D. *Biomacromolecules* **2013**, *14*, 2601-2610.

156. Matsumura, Y.; Kataoka, K. *Cancer Sci.* **2009**, *100*, 572-579.

157. Emoto, S.; Yamaguchi, H.; Kishikawa, J.; Yamashita, H.; Ishigami, H.; Kitayama, J. *Cancer Sci.* **2012**, *103*, 1304-1310.

158. Owen, S. C.; Chan, D. P. Y.; Shoichet, M. S. *Nano Today* **2012**, *7*, 53-65.

159. Savic, R.; Azzam, T.; Eisenberg, A.; Maysinger, D. *Langmuir* **2006**, *22*, 3570-3578.

160. Maysinger, D.; Lovric, J.; Eisenberg, A.; Savic, R. *Eur. J. Pharm. Biopharm.* **2007**, *65*, 270-281.

161. Zhang, S.; Li, Z.; Samarajeewa, S.; Sun, G.; Yang, C.; Wooley, K. L. *J. Am. Chem. Soc.* **2011**, *133*, 11046-11049.

162. O'Reilly, R. K.; Hawker, C. J.; Wooley, K. L. *Chem. Soc. Rev.* **2006**, *35*, 1068-1083.

163. Vila, A.; Gill, H.; McCallion, O.; Alonso, M. J. *J. Controlled Release* **2004**, *98*, 231-244.

164. Tang, B. C.; Dawson, M.; Lai, S. K.; Wang, Y. Y.; Suk, J. S.; Yang, M.; Zeitlin, P.; Boyle, M. P.; Fu, J.; Hanes, J. *Proc. Natl. Acad. Sci. U. S. A.* **2009**, *106*, 19268-19273.

165. Suk, J. S.; Lai, S. K.; Wang, Y. Y.; Ensign, L. M.; Zeitlin, P. L.; Boyle, M. P.; Hanes, J. *Biomaterials* **2009**, *30*, 2591-2597.

166. Cu, Y.; Saltzman, W. M. *Mol. Pharmaceutics* **2009**, *6*, 173-181.

167. Suk, J. S.; Kim, A. J.; Trehan, K.; Schneider, C. S.; Cebotaru, L.; Woodward, O. M.; Boylan, N. J.; Boyle, M. P.; Lai, S. K.; Guggino, W. B.; Hanes, J. *J. Controlled Release* **2014**, *178*, 8-17.

168. Baran, J.; Penczek, S. *Macromolecules* **1995**, *28*, 5167-5176.

169. Lu, Z. Z.; Wu, J.; Sun, T. M.; Ji, J.; Yan, L. F.; Wang, J. *Biomaterials* **2008**, *29*, 733-741.

170. Yang, X. Z.; Wang, Y. C.; Tang, L. Y.; Xia, H.; Wang, J. *J. Polym. Sci., Part A: Polym. Chem.* **2008**, *46*, 6425-6434.

171. Wang, J.; Mao, H. Q.; Leong, K. W. *J. Am. Chem. Soc.* **2001**, *123*, 9480-9481.

172. Gustafson, T. P.; Lim, Y. H.; Flores, J. A.; Heo, G. S.; Zhang, F.; Zhang, S.; Samarajeewa, S.; Raymond, J. E.; Wooley, K. L. *Langmuir* **2014**, *30*, 631-641.

173. Gustafson, T. P.; Cao, Q.; Achilefu, S.; Berezin, M. Y. *ChemPhysChem* **2012**, *13*, 716-723.

174. Philip, R.; Penzkofer, A.; Baumler, W.; Szeimies, R. M.; Abels, C. *J. Photochem. Photobiol., A* **1996**, *96*, 137-148.

175. Le Garrec, D.; Gori, S.; Luo, L.; Lessard, D.; Smith, D. C.; Yessine, M. A.; Ranger, M.; Leroux, J. C. *J. Controlled Release* **2004**, *99*, 83-101.

176. Choi, H. S.; Ashitate, Y.; Lee, J. H.; Kim, S. H.; Matsui, A.; Insin, N.; Bawendi, M. G.; Semmler-Behnke, M.; Frangioni, J. V.; Tsuda, A. *Nat. Biotechnol.* **2010**, *28*, 1300-1303.

177. Garbuzenko, O. B.; Mainelis, G.; Taratula, O.; Minko, T. *Cancer Biol. Med.* **2014**, *11*, 44-55.

178. Geiser, M.; Kreyling, W. G. *Part. Fibre Toxicol.* **2010**, *7*, 2.

179. Gonzalez-Angulo, A. M.; Hortobagyi, G. N. *J. Clin. Oncol.* **2008**, *26*, 1585-1587.

180. Rizzello, L.; Pompa, P. P. *Chem. Soc. Rev.* **2014**, *43*, 1501-1518.

181. *World Health Organization, World Health Statistics* **2014**, 45-46.

182. Klasen, H. J. *Burns* **2000**, *26*, 131-138.

183. Gupta, A.; Matsui, K.; Lo, J. F.; Silver, S. *Nat. Med.* **1999**, *5*, 183-188.

184. Lok, C. N.; Ho, C. M.; Chen, R.; He, Q. Y.; Yu, W. Y.; Sun, H.; Tam, P. K.; Chiu, J. F.; Che, C. M. *J. Biol. Inorg. Chem.* **2007**, *12*, 527-534.

185. Russell, A. D.; Hugo, W. B. *Prog. Med. Chem.* **1994**, *31*, 351-370.

186. Lansdown, A. B.; Sampson, B.; Laupattarakasem, P.; Vuttivirojana, A. *Br. J. Dermatol.* **1997**, *137*, 728-735.

187. Percival, S. L.; Bowler, P. G.; Russell, D. *J. Hosp. Infect.* **2005**, *60*, 1-7.

188. Hidalgo, E.; Dominguez, C. *Toxicol. Lett.* **1998**, *98*, 169-179.

189. Silver, S. *FEMS Microbiol. Rev.* **2003**, *27*, 341-353.

190. Fox, C. L., Jr. *Arch. Surg.* **1968**, *96*, 184-188.

191. Ornelas-Megiatto, C.; Shah, P. N.; Wich, P. R.; Cohen, J. L.; Tagaev, J. A.; Smolen, J. A.; Wright, B. D.; Panzner, M. J.; Youngs, W. J.; Frechet, J. M.; Cannon, C. L. *Mol. Pharmaceutics* **2012**, *9*, 3012-3022.

192. Youngs, W. J.; Knapp, A. R.; Wagers, P. O.; Tessier, C. A. *Dalton Trans.* **2012**, *41*, 327-336.

193. Li, Y. L.; Hindi, K.; Watts, K. M.; Taylor, J. B.; Zhang, K.; Li, Z. C.; Hunstad, D. A.; Cannon, C. L.; Youngs, W. J.; Wooley, K. L. *Chem. Commun.* **2010**, *46*, 121-123.

194. Azzopardi, E. A.; Ferguson, E. L.; Thomas, D. W. *J. Antimicrob. Chemother.* **2013**, *68*, 257-274.

195. Zhou, Y.; Huang, W.; Liu, J.; Zhu, X.; Yan, D. *Adv. Mater.* **2010**, *22*, 4567-4590.

196. Halbes-Letinois, U.; Weibel, J. M.; Pale, P. *Chem. Soc. Rev.* **2007**, *36*, 759-769.

197. Su, Y. J.; Lu, M.; Dong, B. L.; Chen, H.; Shi, X. D. *Adv. Synth. Catal.* **2014**, *356*, 692-696.

198. Kennedy, D. C.; Mckay, C. S.; Tay, L. L.; Rouleau, Y.; Pezacki, J. P. *Chem. Commun.* **2011**, *47*, 3156-3158.

199. Meng, X. Y.; Liao, P. Q.; Liu, J. Q.; Bi, X. H. *Chem. Commun.* **2014**, *50*, 11837-11839.

200. Wang, Y. Y.; Lai, S. K.; Suk, J. S.; Pace, A.; Cone, R.; Hanes, J. *Angew. Chem. Int. Edit.* **2008**, *47*, 9726-9729.

201. Hoyle, C. E.; Lowe, A. B.; Bowman, C. N. *Chem. Soc. Rev.* **2010**, *39*, 1355-1387.

202. Cataido, F. *J. Raman Spectrosc.* **2008**, *39*, 169-176.

203. Feilchenfeld, H.; Weaver, M. J. *J. Phys. Chem.* **1989**, *93*, 4276-4282.

204. Kumar, A.; Pandey, A. K.; Singh, S. S.; Shanker, R.; Dhawan, A. *Chemosphere* **2011**, *83*, 1124-1132.

APPENDIX A

CORE-CROSSLINKED DEGRADABLE POLYPHOSPHOESTER-BASED MICELLES FOR CISPLATIN DELIVERY[*]

In Chapter II, the cisplatin was incorporated into the shell of non-degradable polymeric micelles *via* the formation of polymer-metal complexes with high drug loading. We found that increased shell crosslinking led to decreased cisplatin loading, and increased immunotoxicities due to the incomplete crosslinking by amidation chemistry. In this study, we designed and synthesized nanoscopic delivery vehicles, comprised of degradable polyphosphoester-based polymers. The core of these nanoparticles was loaded with cisplatin without additional covalent crosslinking.

The block copolymer PEG-*b*-PBYPA was synthesized *via* "click-type" reactions as illustrated in Figure A1. Briefly, poly(ethylene glycol)-*b*-poly(2-butynyl phospholane) (PEG-PBYP) was synthesized by ring-opening polymerization of butynyl phospholane (BYP), with PEG (M_n ~ 2000 Da) as the initiator and 1,8-diazabicycloundec-7-ene (DBU) as the catalyst. Within 4 min, a well-defined block copolymer was obtained with relatively low polydispersity index of 1.12, as determined by gel permeation chromatography (GPC). Subsequently, the pendant alkynes along the PBYP block were completely transformed into carboxyl acid groups by copper(I)-catalyzed azide-alkyne

[*] In collaboration with Sarosh Khan, Richen Li, Shiyi Zhang, Mahmoud Elsabahy, Karen L. Wooley, Department of Chemistry, Texas A&M University.

cycloaddition (CuAAC) in dimethylformamide (DMF). The polymer was purified by dialysis against nanopure water containing Chelex 100 resin for three days, to remove copper and other potential contaminants. A white powder was obtained after lyophilization.

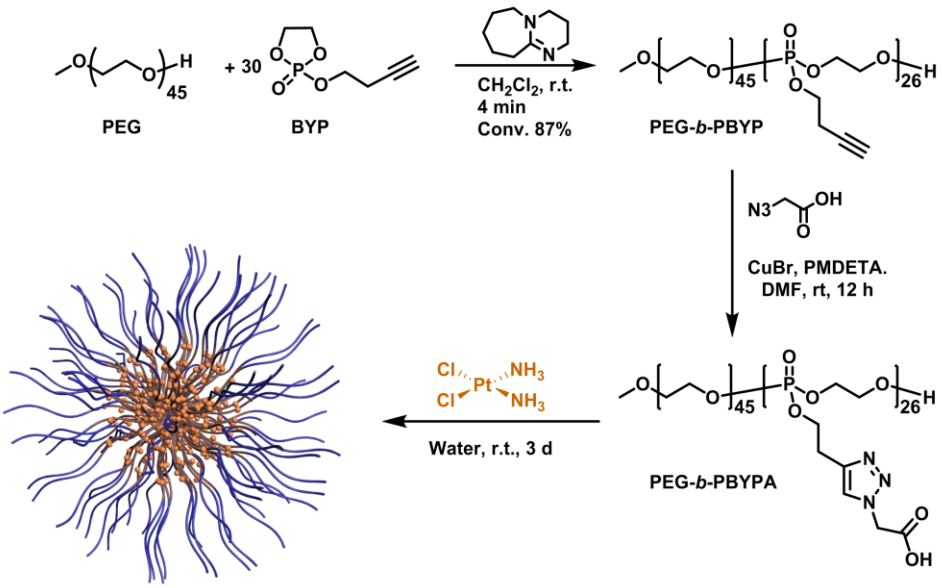

Figure A1. Synthesis of PEG-*b*-PBYPA copolymer *via* ring-opening polymerization, followed by addition of 2-azidoacetic acid by click chemistry. Cisplatin induced the formation of nanoparticle by forming polymer-metal complex.

Cisplatin loading was then performed by incubating the PEG-*b*-PBYPA and cisplatin in water for three days. The coordination bonds between chloride ligands and platinum were labile, and underwent ligand substitution reactions with the pendant carboxylates from the polymer. Since cisplatin has two chloride ligands for substitution, it can crosslink two polymer chains or form an intramolecular loop, leading to decreased water

solubility. The crosslinking of the two polymer chains, together with their decreased water solubility, induced the formation of core-crosslinked micelles. As reported in CHAPTER II, the platinum concentration was quantified by inductively coupled plasma mass spectrometry (ICP-MS). The amount of cisplatin loaded into the nanoparticles was found to increase, with the increasing feed ratio of cisplatin over polymer, but with lower loading efficiencies.

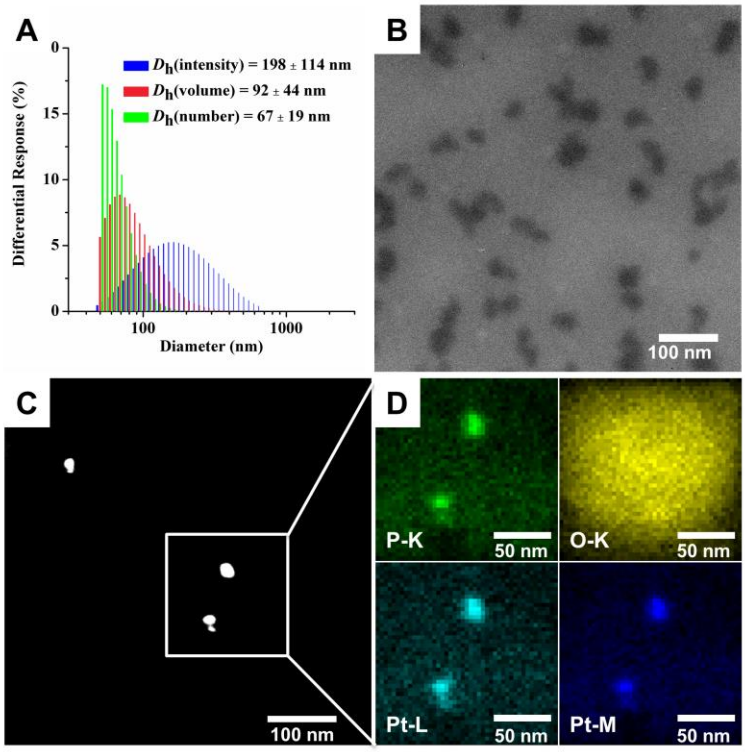

Figure A2. Characterization of Pt-loaded nanoparticles. (A) DLS histograms of intensity-averaged (D_h(intensity)), volume-averaged (D_h(volume)), number-averaged (D_h(number)) hydrodynamic diameters; (B) bright-field TEM; (C) dark-field STEM; (D) EDS elemental mapping.

The cisplatin-loaded nanoparticles were characterized by dynamic light scattering (DLS), transmission electron microscopy (TEM), scanning TEM (STEM), and energy-dispersive X-ray spectroscopy (EDS) elemental mapping (Figure A2). These nanoparticles were shown to have a number-averaged hydrodynamic diameter of 67 nm with a narrow polydispersity index of 0.236, as measured by DLS (Figure A2, A). Samples for TEM were not stained, since Pt itself provided enough contrast for imaging. The platinum core was measured to have a diameter of *ca.* 35 nm by TEM (Figure A2-B). The co-localization of platinum and phosphorous demonstrated that platinum was loaded into the polymeric matrix (Figure A2, C, D).

Moreover, platinum was released in a controlled and sustained manner over 7 days, whereas *ca.* 95% platinum was released in 2 h for cisplatin placed in dialysis cassettes.

In summary, this work demonstrated cisplatin could be loaded into the core of polyphosphoester-based degradable nanoparticles, as an extension of the research in Chapter II. In addition, the *in vitro* cytotoxicities of Pt-loaded nanoparticles and their hydrolytic and enzymatic degradations are under investigation.

Experimental procedures

Synthesis of PEG-*b*-PBYP. In a typical experiment, a solution of poly(ethylene glycol) methyl ether ($mPEG_{45}$, 195 mg, 0.098 mmol, 1.0 eq) in 0.3 mL of anhydrous dichloromethane and a solution of butynyl phospholane (BYP, 515 mg, 2.93 mmol, 30 eq) in 0.2 mL of anhydrous dichloromethane were transferred into a flame-dried 5 mL vial equipped with a rubber stopper and a stir bar. At room temperature, a solution of 1,8-diazabicycloundec-7-ene (DBU, 31 mg, 0.20 mmol, 2.0 eq) in 0.2 mL of anhydrous

dichloromethane was injected into the vial under a nitrogen gas atmosphere. After 4 min, a solution of excessive acetic acid in dichloromethane was added into reaction mixture to quench the reaction. The monomer conversion was measured to be 86% by ^{31}P NMR. The PEG-*b*-PBEP was purified by precipitation into anhydrous diethyl ether three times and dried under vacuum, with a yield of 83%. ^{1}H NMR ($CDCl_3$, ppm): δ 2.05-2.15 (br, $POCH_2CH_2C{\equiv}C\mathit{H}$), 2.55-2.67 (m, $POCH_2C\mathit{H}_2C{\equiv}CH$), 3.41 (s, $CH_2CH_2OC\mathit{H}_3$), 3.67 (s, $CH_2OC\mathit{H}_2C\mathit{H}_2OCH_2$), 4.25-4.28 (m, $POC\mathit{H}_2CH_2C$), 4.29-4.41 ($POC\mathit{H}_2C\mathit{H}_2OP$). ^{13}C NMR ($CDCl_3$, ppm): 20.8, 65.9, 66.6, 70.7, 71.0, 79.7. ^{31}P NMR ($CDCl_3$, ppm): δ -1.61. GPC: M_n = 15900 g/mol, PDI = 1.12. DSC: T_g = -39 °C. TGA in N_2: 170-278 °C, 37% mass loss; 278–310 °C, 34% mass loss; 310–500 °C, 4% mass loss; 25% mass remaining above 500 °C. IR (cm^{-1}): 3700-3080, 3080-2600, 1648, 1460, 1342, 1274, 1009, 956, 843, 802.

Synthesis of anionic polymer. In a 10-mL Schlenk flask equipped with a magnetic stir bar, PEBP-*b*-PBYP (200.0 mg, 0.029 mmol), 2-azidoacetic acid (96 mg, 0.95 mmol), and PMDETA (55 mg, 0.32 mmol) were added and dissolved in DMF (4 mL). The reaction mixture was deoxygenated by freeze-pump-thaw (3x), during which copper(I) bromide (23 mg, 0.16 mmol) was added. The flask was allowed to return to room temperature after the final cycle and stir overnight. The resulting mixture was dissolved in nanopure water and purified by dialysis against nanopure water for 2 days with Chelex resin. The polymer solution was lyophilized to give a white powder. ^{1}H NMR (D_2O, ppm): δ 3.04-3.20 (br, $POCH_2C\mathit{H}_2C{=}CH$), 3.39 (s, $CH_2CH_2OC\mathit{H}_3$), 3.71 (s, $CH_2OC\mathit{H}_2C\mathit{H}_2OCH_2$), 4.11-4.45 (m, $POC\mathit{H}_2CH_2C$, $POC\mathit{H}_2C\mathit{H}_2OP$), 4.96-5.03 (br,

NC*H*$_2$COOH), 7.78-7.87 (br, POCH$_2$C*H*$_2$C=C*H*N). ^{13}C NMR ($CDCl_3$, ppm): 25.9, 45.0, 66.9, 67.3, 69.5, 124.6, 125.3, 165.0. ^{31}P NMR ($CDCl_3$, ppm): δ -1.70. DSC: T_g = -53 °C, T_m = -38 °C. TGA in N_2: 160-310 °C, 23% mass loss; 310–420 °C, 28% mass loss; 420–500 °C, 4% mass loss, 45% mass remaining above 500 °C. IR (cm^{-1}): 3700-3030, 3030-2650, 1615, 1465, 1389, 1341, 1249, 1102, 1059, 1013, 979, 961, 956, 842, 808.

Cisplatin loading. In a typical experiment, to a vial containing a magnetic stir bar and polymer solution (10 mg/mL in water, pH was adjusted to 5.5), a solution of cisplatin (0.5 mg/mL in water, 0.5 molar ratio with respect to the carboxylate groups) was added dropwise. The solution was stirred for three days and then dialyzed against nanopure water at room temperature for 36 h to remove free cisplatin. The purified Pt-loaded nanoparticles were lyophilized to obtain white powder and stored in freezer for further use. Dynamic light scattering (DLS), transmission electron microscopy and inductively coupled plasma mass spectrometry (ICP-MS) were used to measure the particle dimensions and platinum concentrations, respectively.

Platinum release. In a typical procedure, a solution of CDDP-loaded nanoparticles or CDDP (1.0 mL) was transferred into a presoaked dialysis cassette (Slide-A-Lyzer, 10 kDa MWCO, Pierce Biotechnology, Rockford IL). The cassette was allowed to stir in a beaker containing PBS (180 mL, 10 mM phosphate, 137 mM NaCl, pH 7.4 at 37 °C), and 1 mL of samples were collected from the dialysate at pre-determined times and analyzed by ICP-MS, with fresh PBS (2 mL) added back into the beaker. The release experiments were conducted in a triplicate manner.

APPENDIX B

DESIGN AND DEVELOPMENT OF MULTIFUNCTIONAL POLYPHOSPHOESTER-BASED NANOPARTICLES FOR ULTRAHIGH PACLITAXEL DUAL LOADING*

In Chapter III, paclitaxel (PTX) was physically loaded into the PEBP-*b*-PBYP-*g*-PEG micelles, which were highly water-soluble and stable in aqueous solution. The micelles were able to be cleared from the lung relatively fast with a $t_{1/2}$ of 4 days, though they degraded very slowly *in vitro.* In this study, we designed and synthesized nanoscopic multifunctional polyphosphoester-based nanoparticles for ultrahigh paclitaxel dual loading, where PTX was both chemically conjugated and physically loaded. The PTX conjugates could be dissolved in nanopure water with a solubility as high as 110 mg/mL,

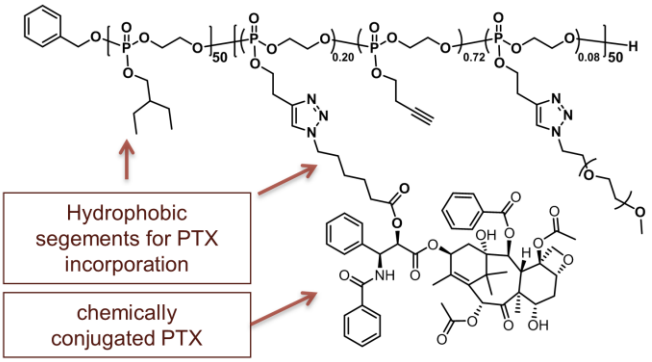

Figure B1. Overall design of multifunctional polyphosphoester-based nanoparticles for ultrahigh paclitaxel dual loading.

* In collaboration with Sarosh Khan, Richen Li, Ashlee Jahnke, Mahmoud Elsabahy, Karen L. Wooley, Department of Chemistry, Texas A&M University.

corresponding to a PTX concentration of 25 mg/mL (PTX loading: 23.0 *wt*%); whereas dual loaded micelles could dissolve in nanopure water with a solubility of 50 mg/mL, where 10 *wt*% was physically loaded PTX and 21 *wt*% was chemically conjugated PTX.

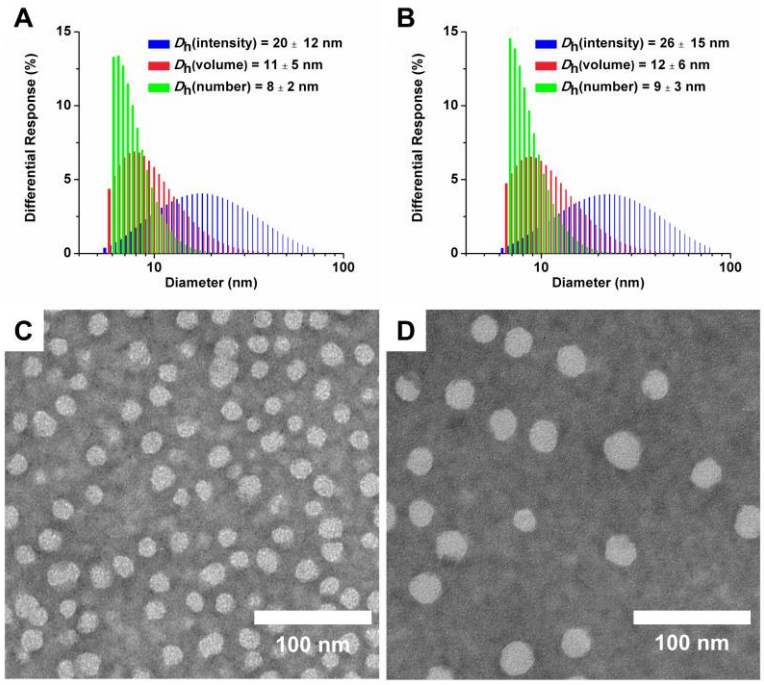

Figure B2. Characterization of nanoparticles. DLS histograms of (A) PTX-conjugated micelles, and (B) PTX dual loaded micelles; TEM images of (C) PTX-conjugated micelles, and (D) PTX dual loaded micelles. Samples were negatively stained by uranyl acetate.

The sizes and size distributions of PTX-conjugated micelles and PTX dual loaded micelles were characterized by dynamic light scattering (DLS) and transmission electron microscopy (TEM) (Figure B2). The PTX-conjugated micelles were measured to have a number-averaged hydrodynamic diameter (D_h(number))of 8 nm, with polydispersity

index of 0.329, as measured by DLS (Figure B2, A). PTX dual loaded micelles displayed a D_h(number) of 9 nm, with slightly lower polydispersity index of 0.267 (Figure B2, B). By TEM, PTX-conjugated micelles were determined to have dry-state diameter of 18 nm, compared to 25 nm of that of PTX dual loaded micelles, both of which had relatively uniform sizes (Figure B2, C, D).

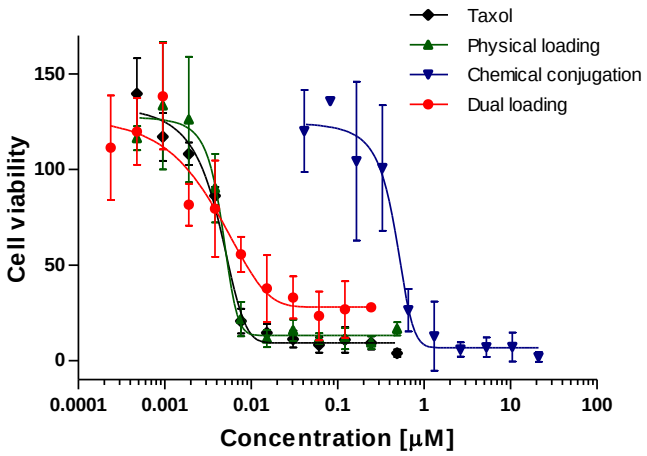

Figure B3. *In vitro* cell viability data in OVCAR-3 with Taxol (IC_{50} = 0.0044 μM), PTX physical loading (IC_{50} = 0.0045 μM), PTX chemical conjugation (IC_{50} = 0.46 μM), and PTX dual loading (IC_{50} = 0.0040 μM, calculated based on the concentration of physically-loaded PTX).

The cytotoxicities of these nanoparticles were studied against OVCAR-3 cancer cell lines (Figure B3). PTX-conjugates were found to be much less cytotoxic compared to Taxol, while PTX physically-loaded and PTX dual loaded micelles demonstrated similar cytotoxicities to Taxol. The lower cytotoxicity of PTX-conjugates was partly due to the relative stable linkages, where nearly no drugs were released in PBS in several days.

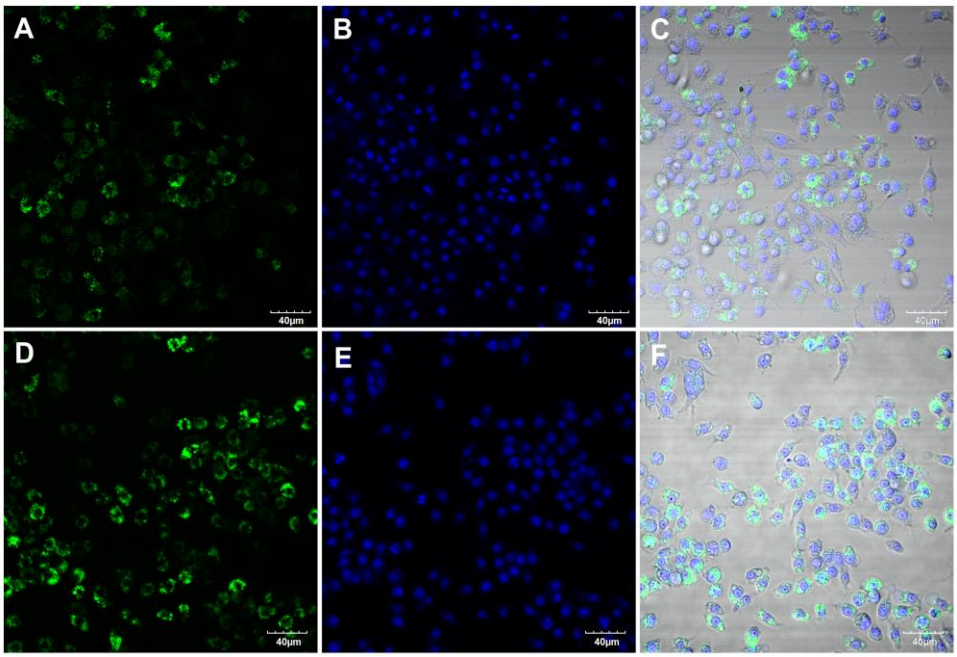

Figure B4. Confocal microscopy images demonstrating cellular internalization of PTX-conjugated micelles (A-C) and PTX dual loaded-micelles (D-F) in RAW 264.7 cells. Green = Alexa Fluor 488 (dye-labelled nanoparticle) and blue = DRAQ5 (nuclear stain). Images to the right overlay fluorescence on the DIC.

To investigate the cell internalization of PTX chemically conjugated and PTX dual loaded nanoparticles, an Alexa Fluor 488 azide was conjugated to the polymer pendant residual alkynes *via* CuAAC in nanopure water. Both fluorescein-labeled nanoparticles were readily internalized, after incubation with RAW 264.7 mouse macrophages for 2 hours (Figure B4).

In summary, nanoscopic multifunctional polyphosphoester-based nanoparticles were prepared, where PTX was both chemically conjugated and physically loaded. These nanoparticles were cytotoxic against cancer cells, and could be easily modified with functional moieties, herein, a fluorescent dye as an example.

Experimental procedures

Synthesis of PEBP-*b*-PBYP-g-PEG/PTX. In a 10-mL Schlenk flask equipped with a magnetic stir bar, PEBP-*b*-PBYP-*g*-PEG (300.0 mg, 0.0110 mmol), azido-PTX (109.1 mg, 0.110 mmol), and PMDETA (19.0 mg, 0.0110 mmol) were added and dissolved in DMF (6 mL). The reaction mixture was deoxygenated by freeze-pump-thaw (3x), during which copper(I) bromide (7.9 mg, 0.0550 mmol) was added. The flask was allowed to return to room temperature after the final cycle and stir overnight in a preheated reaction bath at 37 ^{o}C. The resulting mixture was precipitated from acetone into ethyl ether (3x) to remove unreacted azido-PTX. The crude product was collected and dissolved in 5 mL nanopure water and purified by Sephadex G-25 column to remove copper ions. The solution was transferred to dialysis tubing (MWCO: 12-14 kDa) and dialyzed against nanopure water for 2 days. The micelle solution was then lyophilized to give a white powder (271.3 mg, 66.3 %). ^{1}H NMR ($CDCl_3$, ppm): δ 0.89 (t, *J* = 7.4 Hz, $POCH_2CH(CH_2\mathit{CH_3})_2$), 1.08-1.31 (broad multiple peaks, protons from PTX), 1.37 (m, $POCH_2CH(C\mathit{H_2}CH_3)_2$), 1.52 (m, $POCH_2C\mathit{H}$), 1.56-2.80 (broad multiple peaks, protons from PTX, $POCH_2CH_2C{\equiv}C\mathit{H}$), $POCH_2C\mathit{H_2}C{\equiv}CH$), 3.00-3.18 (brs, $NC\mathit{H_2}CH_2$), 3.38 (s, $OC\mathit{H_3}$), 3.64 (s, $OC\mathit{H_2}C\mathit{H_2}$ from PEG), 3.78 (m, CH from PTX(C-3)-C*H*), 3.96-4.02 (t, *J* = 5.5 Hz, $POC\mathit{H_2}CH$), 4.02-4.56 (br, POC*H2*CH2, POC*H2*C*H2*OP, and protons from PTX), 4.90-5.00 (br, CH from PTX(C-5)-C*H*), 5.07 (d, *J* = 8.0 Hz, $OC\mathit{H_2}Ar$), 5.48 (br, CH from PTX(C-2')-C*H*), 5.65 (br, CH from PTX(C-2)-C*H*), 5.90 (br, CH from PTX(C-3')-C*H*), 6.15 (br, CH from PTX(C-13)-C*H*), 6.30 (br, CH from PTX(C-10)-C*H*), 7.28-7.70 (broad multiple peaks, Ph*H* from PTX, $CH_2CH_2CC\mathit{H}NCH_2$), 7.75 (br, Ph*H* from

PTX), 8.11 (br, Ph*H* from PTX). ^{13}C NMR ($CDCl_3$, ppm): δ 9.9, 11.1, 15.0, 20.8, 21.1, 21.53, 22.2, 22.9, 24.2, 25.8, 26.9, 27.2, 29.9, 33.5, 35.6, 36.0,41.9, 43.4, 45.2,46.0, 50.0, 50.3, 53.5, 58.6,59.3, 65.8-67.3 (multiple overlapping br), 70.2, 70.8, 71.5-72.5 (multiple overlapping br), 74.4, 75.2, 75.8, 79.1, 81.2, 84.6,122.5, 127.2-129.8 (multiple overlapping br), 130.4, 132.1, 132.8, 133.0, 133.9, 134.0, 137.3, 142.1-144.0 (multiple overlapping br), 167.1, 167.5, 170.1, 171.2, 172.7, 204.0. ^{31}P NMR ($CDCl_3$, ppm): δ -0.98 and -1.70. DSC: T_g = -15 °C. TGA in N_2: 200-270 °C, 33% mass loss; 270–330 °C, 29% mass loss; 420–500 °C, 6% mass loss, 32% mass remaining above 500 °C.

Self-assembly of PEBP-*b*-PBYP-*g*-PEG/PTX. The polymer was directly dissolved in water and sonicated for 5 min and micelles formed spontaneously. The solubility could be as high as 110 mg/mL, with a PTX concentration of 25 mg/mL (PTX loading: 23.0 wt%). Hydrodynamic diameters of SCKs in nanopure water as measured by DLS: D_h(intensity) = 22 ± 12 nm, D_h(volume) = 11 ± 5 nm, D_h(number) = 8 ± 2 nm; ζ-potential in nanopure water: - 43 ± 3 mV

PTX loading into PEBP-*b*-PBYP-*g*-PEG/PTX. In a typical experiment, to a 20-mL vial containing 50.0 mg of polymer in ethanol (50.0 mg/mL), a solution of PTX (5.56 mg, 2.0 mg/mL in ethanol, 10 wt%) was added. The flask was shaken robustly to mix the solution, and then ethanol was completely removed *in vacuo*. Subsequently, 1.0 mL of nanopure water was added to the vial to resuspend the polymer and PTX mixture. After sonication for 5 min, a well dispersed nanoparticle suspension was obtained. The resuspension was centrifuged at 4000 rpm for 5 minutes to remove possible large aggregates. PTX concentration in the upper clear supernatant was determined by HPLC

with acetonitrile and 20 mM ammonium acetate (45/55) as the eluent. Final PTX loading: 10 *wt*% was physically loaded and 21 *wt*% was chemically conjugated. DLS, AFM and TEM were used to characterize these PTX-loaded nanoparticles, and HPLC was used to confirm the actual loading amount of PTX. Hydrodynamic diameters of SCKs in nanopure water as measured by DLS: D_h(intensity) = 26 ± 15 nm, D_h(volume) = 12 ± 6 nm, D_h(number) = 9 ± 3 nm; ζ-potential in nanopure water: - 40 ± 4 mV.

Dye-labeling of PEBP-b-PBYP-g-PEG/PTX. In a typical experiment, an oven-dried vial containing a magnetic stir bar was charged with PEBP-*b*-PBYP-*g*-PEG/PTX, 10.0 mg, 0.268 μmol), Alexa Fluor 488 azide (0.116 mg from a 1.0 mg/mL stock solution in DMSO, 0.134 μmol), copper (II) sulfate pentahydrate (0.0672 mg, from 1.0 mg/mL stock solution in water, 0.268 μmol), sodium ascorbate (0.532 mg, 2.68 μmol) and 2.0 mL nanopure water. The reaction mixture was degassed for 10 min *via* nitrogen bubbling, wrapped with aluminum foil and stirred for another 12 h at 37 °C. The solution was subsequently passed through a Sephadex G-25 desalting column and dialyzed against Chelex® 100 resin in nanopure water in presoaked dialysis tubing (MWCO *ca*. 12 – 14 kDa) for 2 days, to remove copper ions and unreacted dye, followed by lyophilization to yield green to yellow powder with a 92% yield and a 75% conjugation efficiency.

APPENDIX C

PREPARATION AND *IN VITRO* ANTIMICROBIAL ACTIVITIES OF DEGRADABLE NANOPARTICLES CAPABLE OF DUAL LOADING OF SILVER CATIONS AND MINOCYCLINE FOR BACTERIAL LUNG INFECTIONS*

Pulmonary infections are becoming difficult to treat, partly due to the widespread bacterial resistance. Combinational delivery of antimicrobials, which have different killing mechanisms, has the potential to overcome bacterial resistance. In this project, we designed and synthesized anionic shell crosslinked knedel-like nanoparticle (aSCKs), which could carry both silver cations *via* Ag-S interaction, and minocycline *via* electrostatic interaction.

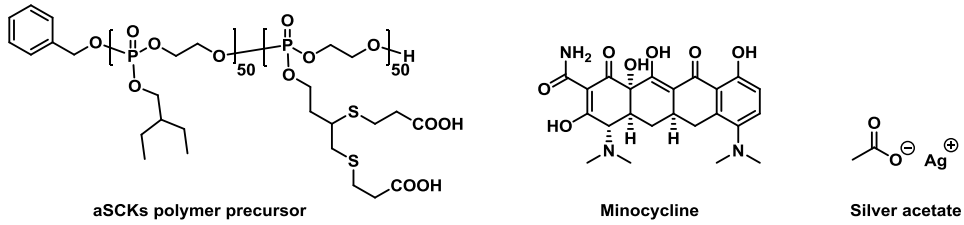

Figure C1. Chemical structures for aSCK polymer precursor, minocycline, and silver acetate.

* In collaboration with Parth N. Shah,[†] Justin A. Smolen,[†,§] Richen Li,[§] Carolyn L. Cannon,[†] Karen L. Wooley,[§] [†]Department of Microbial Pathogenesis and Immunology, College of Medicine, Texas A&M Health Science Center, [§]Department of Chemistry, Texas A&M University.

The anionic polymer was synthesized *via* thiol-yne reaction between 3-mercaptopropionic acid and diblock copolymer poly(2-ethylbutoxy phospholane)-*block*-poly(2-butynyl phospholane) (PEBP-*b*-PBYP). Then, aSCKs were prepared by self-assembly of the anionic polymer, followed by crosslinking using a diamine as a crosslinker. Silver cations and minocycline were loaded into the aSCKs by mixing them together for 3 h, and purified by centrifugal filter devices. The dual loaded aSCKs were obtained by stirring silver-loaded aSCKs with minocycline for 3 h, followed by purification. Both silver cations and minocycline could be loaded into the same aSCKs with *ca.* 10% loading (Table C1). Dual loaded aSCKs had a slightly higher minocycline loading, which might be due to some potential interaction between the two drugs. Dynamic light scattering (DLS) suggested that dual loaded aSCKs had a largest number-averaged hydrodynamic diameter (D_h(number)) of 22 nm, whereas the D_h(number) of minocycline-loaded aSCKs was measured to be smallest of 12 nm (Figure C2). Transmission electron microscopy (TEM) indicated that these nanoparticles were spherical (Figure C2).

Table C1. Silver and minocycline loading into aSCKs.

	Ag (mg)	Minocycline hydrochloride (mg)	SCKs (mg)	Drug loading
Ag-SCKs	0.464	0	4.6	10.1%
Mino-SCKs	0	0.175	1.63	10.8%
Dual-SCKs	0.161	0.217	1.62	Ag: 9.9%; Minocycline hydrochloride: 13.4%

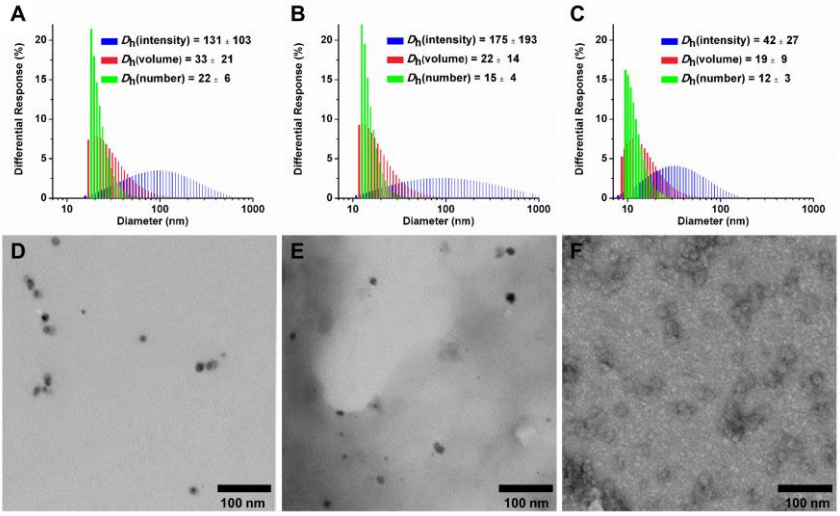

Figure C2. DLS (top) and TEM (bottom) of drug-loaded aSCKs. From left to right: Dual loaded aSCKs, Ag-loaded aSCKs, and minocycline-loaded aSCKs. Samples D and E were not stained, and sample F was stained by uranyl acetate.

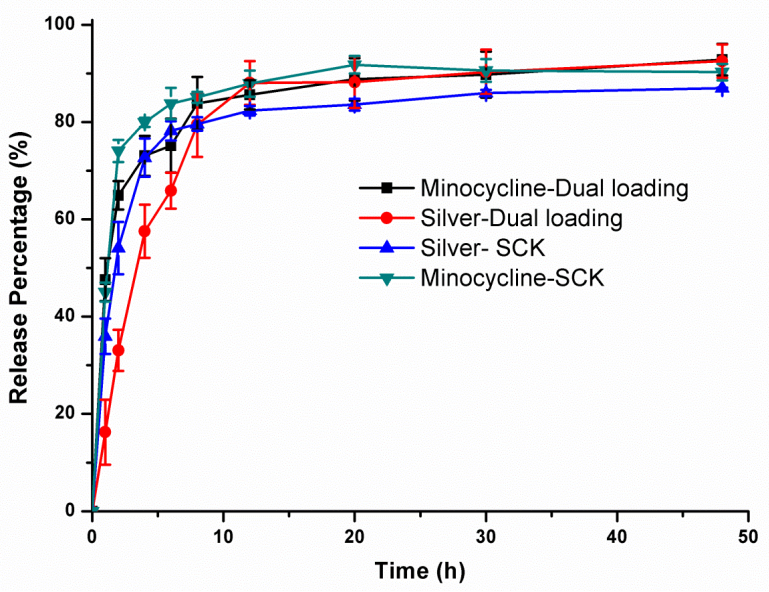

Figure C3. Drugs releases from aSCKs in nanopure water at 37 °C.

The *in vitro* drug release experiments were investigated in nanopure water (Figure C3). Rapid drug releases were observed for all drug-loaded aSCKs. The release half-life of minocycline from either minocycline-loaded nanoparticles or dual loaded nanoparticles was *ca.* 1.1 h. Interestingly, the release of silver was slower in the dual loaded nanoparticles compared to the Ag-loaded nanoparticles.

In conclusion, we were able to load both silver cations and minocycline into the same nanoparticle with relatively high loading. Both drugs could be released from the dual loaded nanoparticles. Their *in vitro* antimicrobial activities and *in vivo* performance are currently under investigation.

Experimental procedures

Preparation of aSCKs. The anionic diblock copolymers (623 mg, 2.08 mmol of acrylic acid) were suspended into nanopure water (60.0 mL) and sonicated for 10 min. The clear solution was stirred for another 1 hour to obtain well dispersed micelles, followed by the addition of a solution of 2,2'-(ethylenedioxy)bis(ethylamine) (EDDA, 46.1 mg, 0.311 mmol) dropwisely in nanopure water (10.0 mL). The solution was allowed to stir for 1 h at room temperature. To this reaction mixture was added dropwise a solution of 1-[3'-(Dimethylamino)propyl]-3-ethylcarbodiimide methiodide (EDCI, 204 mg, 0.687 mmol) in nanopure water (10.0 mL) *via* a syringe pump over 1 hour. The reaction mixture was allowed to stir overnight at room temperature and was then transferred to presoaked dialysis membrane tubes(MWCO *ca.* 12–14 kDa), and dialyzed against nanopure water for 36 h in the cold room (4–8 ºC) to remove small

molecules. The purified anionic SCKs solution was lyophilized into powder and kept in the freezer at -20 ºC.

Silver loading into aSCKs. In a typical experiment, aSCKs (250 mg) were dissolved in 25.0 mL of nanopure water and sonicated for 5 min. Silver acetate (100 mg) in 20.0 mL of nanopure water was added, and the mixture solution was shaded with aluminum foils and stirred overnight. The solution was transferred to a centrifugal filter device (100 kDa MWCO), and washed extensively for several cycles (N>3) with nanopure water to remove free small molecules. The amount of silver loaded into the micelles was quantified by ICP-MS using rhodium as an internal standard.

Minocycline loading into aSCKs. In a typical experiment, aSCKs (5.0 mg) were dissolved in 3.0 mL of nanopure water and sonicated for 5 min. Minocycline hydrochloride (1.5 mg) in 1.0 mL of nanopure water was added, and the mixture solution was shaded with aluminum foils and stirred overnight. The solution was transferred to a centrifugal filter device (100 kDa MWCO), and washed extensively for several cycles (N>3) with nanopure water to remove free small molecules. The amount of minocycline hydrochloride loaded into the micelles was quantified by UV-Vis using absorbance at 345nm.

Dual loading into aSCKs. In a typical experiment, Ag-loaded aSCKs (9.2 mg, containing 0.92 mg silver) were dissolved in 5.0 mL of nanopure water and sonicated for 5 min. Minocycline hydrochloride (2.8 mg) in 1.8 mL of nanopure water was added, and the mixture solution was shaded with aluminum foils and stirred overnight. The solution was transferred to a centrifugal filter device (100 kDa MWCO), and washed

extensively for several cycles (N>3) with nanopure water to remove free small molecules. The amount of minocycline hydrochloride loaded into the micelles was quantified by UV-Vis using absorbance at 345nm, while the amount of silver loaded into the micelles was quantified by ICP-MS using rhodium as an internal standard.

Release of drugs from nanoparticles. The release profiles of the drug-loaded aSCKs were studied by monitoring the decrease of drug concentration over time in dialysis cassettes by ICP-MS or UV-Vis. In a typical procedure, drug-loaded aSCKs (3.0 mL) were transferred into a presoaked dialysis cassette. The cassette was allowed to stir in a beaker containing 3000 mL nanopure water at 37 °C. Aliquots (*ca.* 0.05 mL) were taken at pre-determined time. Silver and minocycline hydrochloride concentrations were determined by ICP-MS and UV-Vis, respectively. The release experiments were conducted in a triplicate manner.

APPENDIX D

OTHER JOINT WORK AND LIST OF PUBLICATIONS IN GRADUATE STUDY

Besides the three chapters and three appendices above, other joint research was also conducted (Table D1). Polyphosphoester-based materials were extensively investigated, which laid the foundation of this dissertation. Their design, syntheses, properties, and various biomedical applications were discussed in details in publications listed in Table D1 under entry 1-3, 7, 9. 10, 12, 16. Another important class of degradable materials is polypeptides, which were facilely synthesized by ring-opening polymerization of N-carboxyanhydrides (NCAs) and exploited as both organogelators and hydrogelators because of their ability to form secondary structures (Table D1, entry 4-6, 14). Furthermore, poly(carboxybetaine) was prepared and evaluated against poly(ethylene glycol) both *in vitro* and *in vivo* as nanoparticle coating material (Table D1, entry 8, 17). In addition, poly(acrylic acid)-based block copolymers were also utilized as nanocarriers of cisplatin by forming polymer-metal complex and silver-based antimicrobials through electrostatic interactions, as well as building blocks in the hierarchical assembly of multicompartment superstructures (Table D1, entry 11, 13, 15).

Table D1. List of co-authored publications in graduate study.

Entry	Authors
1	Lim, Y. H.; Tiemann, K. M.; Heo, G. S.; Wagers, P. O.; Rezenom, Y. H.; Zhang, S.; Zhang, F.; Youngs, W. J.; Hunstad, D. A.; Wooley, K. L. "Preparation and *in vitro* antimicrobial activity of silver-bearing degradable polymeric nanoparticles of polyphosphoester-*block*-poly(L-lactide)", *ACS Nano* **2015**, *9*, 1995-2008.
2	Zhang, F.; Zhang, S.; Pollack, S. F.; Li, R.; Gonzalez, A. M.; Fan, J.; Zou, J.; Leininger, S. E.; Pavía-Sanders, A.; Johnson, R.; Nelson, L. D.; Raymond, J. E.; Elsabahy, M.; Hughes, D. M. P.; Lenox, M. W.; Gustafson, T. P.; Wooley, K. L. "Improving paclitaxel delivery: *in vitro* and *in vivo* characterization of PEGylated polyphosphoester-based nanocarriers", *J. Am. Chem. Soc.* **2015**, *137*, 2056-2066.
3	Zhang, F.; Smolen, J. A.; Zhang, S.; Li, R.; Shah, P. N.; Cho, S.; Wang, H.; Raymond, J. E.; Cannon, C. L.; Wooley, K. L. "Degradable polyphosphoester-based silver-loaded nanoparticles as therapeutics for bacterial lung infections", *Nanoscale* **2015**, *7*, 2265-2270.
4	He, X.; Fan, J.; Zhang, F.; Li, R.; Pollack, K. A.; Raymond, J. E.; Zou, J.; Wooley, K. L. "Multi-responsive hydrogels derived from the self-assembly of tethered allyl-functionalized racemic oligopeptides", *J. Mater. Chem. B* **2014**, *2*, 8123-8130.
5	Fan, J.; Li, R.; He, X.; Seetho, K.; Zhang, F.; Zou, J.; Wooley, K. L. "Construction of a versatile and functional nanoparticle platform derived from a helical diblock copolypeptide-based biomimetic polymer", *Polym. Chem.* **2014**, *5*, 3977-3981.
6	Fan, J.; Zou, J.; He, X.; Zhang, F.; Zhang, S.; Raymond, J. E.; Wooley, K. L. "Tunable mechano-responsive organogels by ring-opening copolymerizations of N-carboxyanhydrides", *Chem. Sci.* **2014**, *5*, 141-150.
7	Zou, J.; Zhang, F.; Zhang, S.; Pollack, S. F.; Elsabahy, M.; Fan, J.; Wooley, K. L. "Poly(ethylene oxide)-*block*-polyphosphoester-*graft*-paclitaxel conjugates with acid-labile linkages as a pH-sensitive and functional nanoscopic platform for paclitaxel delivery", *Adv. Healthcare Mater.* **2014**, *3*, 441-448.
8	Elsabahy, M.; Li, A.; Zhang, F.; Sultan, D.; Liu, Y; Wooley, K. L. "Differential immunotoxicities of poly(ethylene glycol)- *vs.* poly(carboxybetaine)-coated nanoparticles", *J. Controlled Release* **2013**, *172*, 641-652.
9	Shen, Y.; Zhang, S.; Zhang, F.; Loftis, A.; Pavía-Sanders, A.; Zou, J.; Fan, J.; Taylor, J.-S. A.; Wooley, K. L. "Polyphosphoester-based cationic nanoparticles serendipitously release integral biologically-active components to serve as novel degradable inducible nitric oxide synthase inhibitors", *Adv. Mater.* **2013**, *25*, 5609-5614.
10	Elsabahy, M.; Zhang, S.; Zhang, F.; Deng, Z.; Lim, Y. H.; Wang, H.; Parsamian, P.; Hammond, P. T.; Wooley, K. L. "Surface charges and shell crosslinks each play significant roles in mediating degradation, biofouling, cytotoxicity and immunotoxicity for polyphosphoester-based nanoparticles", *Sci. Rep.* **2013**, *3*, 3133: 1-10.

Table D1. Continued.

11	Shah, P. N.; Lin, L. Y.; Smolen, J. A.; Tagaev, J. A.; Gunsten, S. P.; Heo, G. S.; Li, Y.; Zhang, F.; Zhang, S.; Kang, A. G.; Wright, B. D.; Panzner, M. J.; Youngs, W. J.; Brody, S. L.; Wooley, K. L.; Cannon, C. L. "Synthesis, characterization, and *in vivo* efficacy of shell crosslinked nanoparticle formulations carrying silver antimicrobials as aerosolized therapeutics", *ACS Nano*, **2013**, *7*, 4977-4987.
12	Zhang, S.; Wang, H.; Shen, Y.; Zhang, F.; Seetho, K.; Zou, J.; Taylor, J. -S. A.; Wooley, K. L. "A simple and efficient synthesis of an acid-labile polyphosphoramidate by organobase-catalyzed ring-opening polymerization and transformation to polyphosphoester ionomers by acid treatment", *Macromolecules* **2013**, *46*, 5141-5149.
13	Zhang, F.; Elsabahy, M.; Zhang, S.; Lin, L. Y.; Zou, J.; Wooley, K. L. "Shell crosslinked knedel-like nanoparticles for delivery of cisplatin: effects of crosslinking", *Nanoscale* **2013**, *5*, 3220-3225.
14	Zou, J.; Zhang, F.; Zhang, S.; Fan, J.; Raymond, J. E.; Zhu, J.; Li, A.; Seetho, K.; Pochan, D. J.; Wooley, K. L. "Responsive organogels formed by supramolecular self assembly of PEG-*block*-allyl-functionalized polypeptides into β-sheet-driven polymeric ribbons", *Soft Matter* **2013**, *9*, 5951-5958.
15	Zhu, J.; Zhang, S.; Zhang, F.; Wooley, K. L.; Pochan, D. J. "Hierarchical assembly of complex block copolymer nanoparticles into multicompartment superstructures through tunable interparticle associations", *Adv. Funct. Mater.* **2013**, *23*, 1767-1773.
16	Zhang, S.; Zou, J.; Zhang, F.; Elsabahy, M.; Felder, S. E.; Zhu, J.; Pochan, D. J.; Wooley, K. L. "Rapid and versatile construction of diverse and functional nanostructures derived from a polyphosphoester-based biomimetic block copolymer system", *J. Am. Chem. Soc.* **2012**, *134*, 18467-18474.
17	Li, A.; Luehmann, H. P.; Sun, G.; Samarajeewa, S.; Zou, J.; Zhang, S.; Zhang, F.; Welch, M. J.; Liu, Y.; Wooley, K. L. "Synthesis and *in vivo* pharmacokinetic evaluation of degradable shell cross-linked polymer nanoparticles with poly(carboxybetaine) *vs.* poly(ethylene glycol) surface-grafted coatings", *ACS Nano* **2012**, *6*, 8970-8982.